Centrum voor Wiskunde en Informatica

REPORT*RAPPORT*

MAS

Modelling, Analysis and Simulation

Modelling, Analysis and Simulation

Unsteady compressible two-fluid flow model for interface capturing.

On the dynamics of a shock-bubble interaction

J.J. Kreeft

REPORT MAS-E0717 NOVEMBER 2007

Centrum voor Wiskunde en Informatica (CWI) is the national research institute for Mathematics and Computer Science. It is sponsored by the Netherlands Organisation for Scientific Research (NWO).
CWI is a founding member of ERCIM, the European Research Consortium for Informatics and Mathematics.

CWI's research has a theme-oriented structure and is grouped into four clusters. Listed below are the names of the clusters and in parentheses their acronyms.

Probability, Networks and Algorithms (PNA)

Software Engineering (SEN)

Modelling, Analysis and Simulation (MAS)

Information Systems (INS)

P.O. Box 94079, 1090 GB Amsterdam (NL)
Kruislaan 413, 1098 SJ Amsterdam (NL)
Telephone +31 20 592 9333
Telefax +31 20 592 4199

ISSN 1386-3703

Unsteady compressible two-fluid flow model for interface capturing.

On the dynamics of a shock-bubble interaction

ABSTRACT

Multi-fluid flows are found in many applications in engineering and physics. Examples of these flows from engineering are water-air flows in ship hydrodynamics, exhaust-air flows behind rockets, gas-petrolea flows in upstream pipes of oil rigs, air-fuel bubble interaction flows in scramjets and many others. To gain better insight in the behavior of multi-fluid flows, especially two-fluid flows, numerical simulations are needed. We assume that the fluids do not mix or chemically react, but remain separated by a sharp interface. With these assumptions a model is developed for unsteady, compressible two-fluid flow, with pressures and velocities that are equal on both sides of the interface. The model describes the behavior of a numerical mixture of the two fluids (not a physical mixture). This kind of interface modeling is called interface capturing. Numerically, the interface becomes a transition layer between both fluids. The model consists of five equations; mass, momentum and energy equation for the mixture (these are the standard Euler equations), mass equation for one of the two fluids and energy equation for one of the two fluids. This last equation is not conservative, but contains a source term. The source term represents the exchange of energy between the two fluids. The model is discretized by using a finite-volume approximation. The finite-volume method consists of a third-order Runge-Kutta scheme for temporal discretization and a limited second-order spatial discretization. For the flux evaluation Osher's Riemann solver is constructed, which uses a new set of Riemann invariants that was derived for the two-fluid model. The source term is evaluated using the limited state distribution and the wave pattern in the Osher solver. The two-fluid model is validated on several shock tube problems. The results show that the method is pressure-oscillation-free without special precautions, which is not the case for most other two-fluid flow models. The developed method is applied to two shock-bubble interaction problems. The numerical results really show the competence of the two-fluid model.

2000 Mathematics Subject Classification: 65M60, 76N15, 76T10

Keywords and Phrases: Unsteady compressible two-fluid flow, interface capturing, source term, energy exchange, Osher's Riemann solver, finite-volume discretization, shock tube problem, shock-bubble interaction

Unsteady Compressible Two-Fluid Flow Model for Interface Capturing

On the Dynamics of a Shock-Bubble Interaction

October 2007

J.J. Kreeft

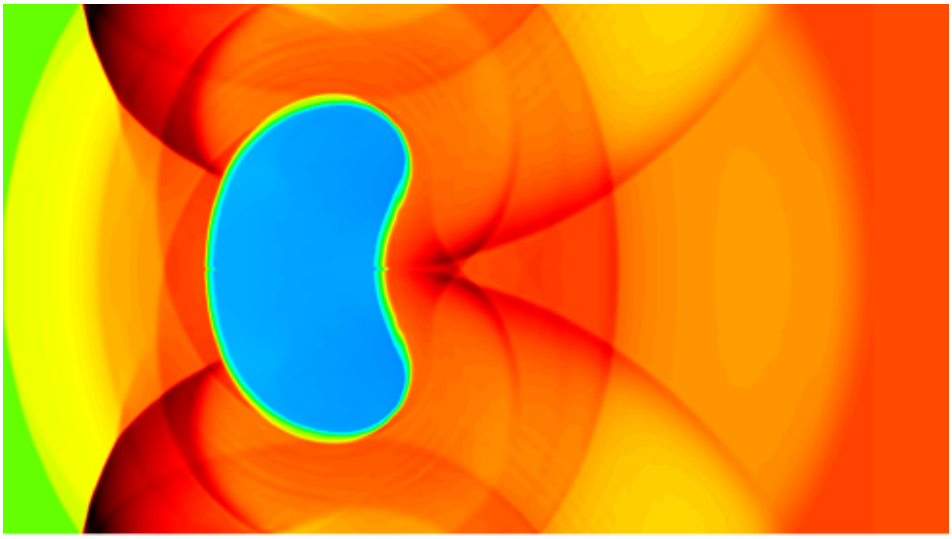

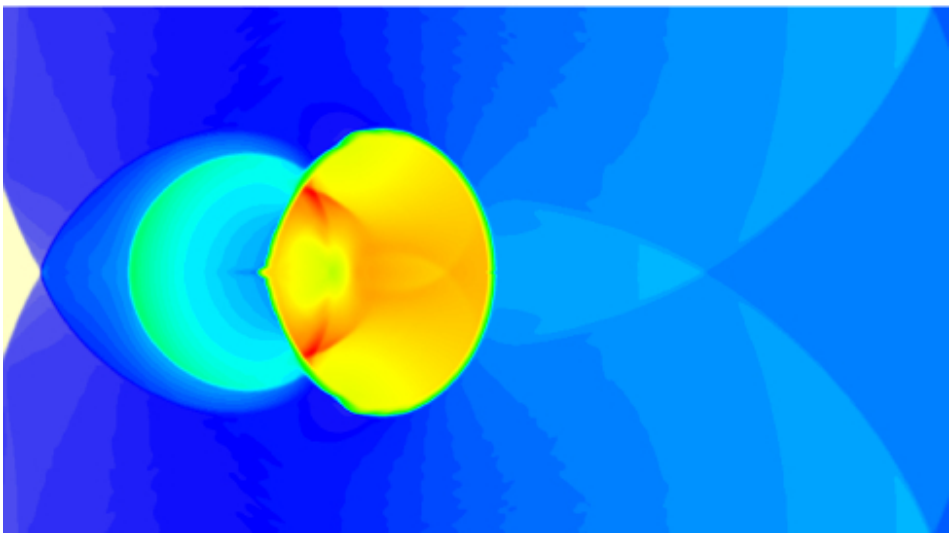

Centre for Mathematics and Computer Science

Delft University of Technology

Unsteady Compressible Two-Fluid Flow Model for Interface Capturing

On the Dynamics of a Shock-Bubble Interaction

Master of Science Thesis

For obtaining the degree of
Master of Science in Aerospace Engineering
at
Delft University of Technology

J.J. Kreeft

September 14, 2007

Faculty of Aerospace Engineering · Delft University of Technology

Preface

This report is my final work of my study at the faculty of Aerospace Engineering at Delft University of Technology. The work was performed within the chair of Aerodynamics in cooperation with the Centre of Mathematics and Computer Science (CWI) in Amsterdam. The report presents the work I did the last twelve months on two-fluid flow modeling. This work would not have been a success without the help and support of the a several people.

First of all I would like to thank my supervisor Barry Koren who gave me the opportunity to work on this challenging and interesting subject and for providing me a work spot at CWI. His enthusiasm and dedication, during my thesis work and also during my participation as a teaching assistant in the course Computational Fluid and Structural Mechanics, made our cooperation to a pleasant and instructive period.
I am especially grateful to Jeroen Wackers and Harald van Brummelen. Without all the conversations and discussions we had, the result would not have been as it is now in front of you.
Furthermore I would like to thank the people of Aerodynamics and CWI for their support and the people of the "Aero-basement" for their support, discussions and other activities which made it to a pleasant stay.
Above all I would like to thank my parents, brothers and friends for their support during my study, and last but definitely not least I would like to thank my girlfriend for her endless support during my study and graduation period.

Jasper Kreeft
Delft, September 2007

Abstract

Multi-fluid flows are found in many applications in engineering and physics. Examples of these flows from engineering are water-air flows in ship hydrodynamics, exhaust-air flows behind rockets, gas-petrolea flows in upstream pipes of oilrigs, air-fuel bubble interaction flows in scramjets and many others. To gain better insight in the behavior of multi-fluid flows, especially two-fluid flows, numerical simulations are needed.
We assume that the fluids do not mix or chemically react, but remain separated by a sharp interface. With these assumptions a model is developed for unsteady, compressible two-fluid flow, with pressures and velocities that are equal on both sides of the interface. The model describes the behavior of a numerical mixture of the two-fluids (not a physical mixture). This kind of interface modeling is called interface capturing. Numerically, the interface becomes a transition layer between both fluids.
The model consists of five equations; mass, momentum and energy equation for the mixture (these are the standard Euler equations), mass equation for one of the two fluids and energy equation for one of the two fluids. This last equation is not conservative, but contains a source term. The source term represents the exchange of energy between the two fluids.
The model is discretized by using a finite-volume approximation. The finite-volume method consists of a third-order Runge-Kutta scheme for temporal discretization and a limited second-order spatial discretization. For the flux evaluation Osher's Riemann solver is constructed, which uses a new set of Riemann invariants that was derived for the two-fluid model. The source term is evaluated using the limited state distribution and the wave pattern in the Osher solver.
The two-fluid model is validated on several shock tube problems. The results show that the method is pressure-oscillation-free without special precautions, which is not the case for most other two-fluid flow models. The developed method is applied to two shock-bubble interaction problems. The numerical results really show the competence of the two-fluid model.

Keywords: Unsteady compressible two-fluid flow, interface capturing, source term, energy exchange, Osher's Riemann solver, finite-volume discretization, shock tube problem, shock-bubble interaction.

Table of Contents

Chapter 1

Introduction

The complex mechanics of multiple fluid flows that occur in many applications in engineering and physics has attracted quite some interest in recent years. Examples of these flows from engineering are water-air flows in ship hydrodynamics, exhaust-air flows behind rockets, gas-petrolea flows in upstream pipes of oilrigs, air-fuel bubble interaction flows in scramjets and many others. The latter example is treated in detail in this report. Although much research has already been done on two-fluid modeling, it is still a challenge to accurately simulate these problems. Theoretical analysis and experiments can give us insight in the behavior of two-fluid flows, but numerical simulations are needed to extend the knowledge and to use it in engineering applications.
This report presents a model for unsteady compressible two-fluid flow. The two fluids do not mix or chemically react, but remain separated by a sharp interface. The pressures and velocities of both fluids are equal on both sides of the interface. The model is an extension of the well-known single-fluid Euler equations. The numerical treatment of the interface in the two-fluid model is referred to as interface capturing. Different methods for interface modeling have been proposed in the past years. In the next section the basic ideas of the different methods are discussed and the method used in this report is explained.

1.1 Treating the interface

To numerically model the interface of the two immiscible fluids and to couple this model to a flow model without introducing large errors is a big challenge. Many different methods have been presented, which can be divided into *Lagrangian* and *Eulerian* types of methods. The former type is also referred to as *interface-fitting*. The later type can be subdivided into *interface-capturing* and *interface-tracking*. Below a short overview of the different approaches is given and it is explained why a certain method is chosen. For a complete overview of Lagrangian and Eulerian methods see [5].
Interface-fitting is of the Lagrangian type. In this method the grid deforms each time step and aligns with the interface, see figure 1.1. This results in a sharp interface. However moving-grid methods are not applicable for the computation of bifurcating interfaces and are less applicable in flows with large deformation, which is typical for many flow problems.
Interface-capturing is of the Eulerian type. Eulerian methods use a fixed grid, making these methods, in contrast to Lagrangian methods, well-suited for large deformations. To describe the behavior of both fluids and their interface, interface-capturing methods

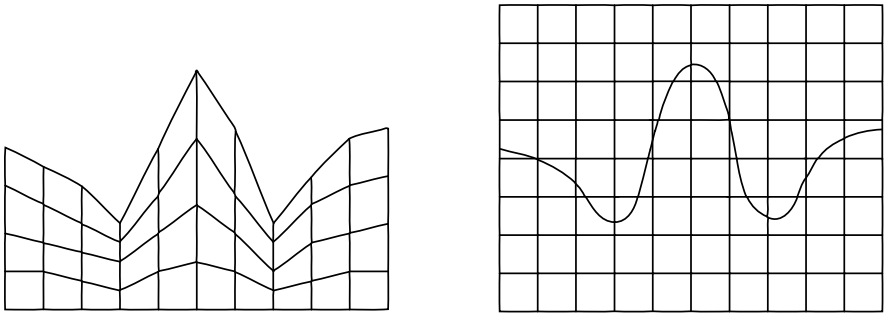

Figure 1.1: Left: moving grid, Lagrangian type. Right: fixed grid, Eulerian

use flow variables only. No separate treatment of the interface is needed. The flow equations model the flow as a mixture of both fluids. In this approach the interface acts as a smooth transition layer. This causes some numerical smearing of the interface, which locally acts as a mixture of both fluids.
Former interface-capturing approaches use the single-fluid equations together with a transport equation describing the mixture of the fluid, expressed in the mass fraction or in the ratio of specific heats. The interface location implicitly follows from the flow solution. In [1] it is shown that these methods suffer from spurious pressure oscillations. Nowadays flow equations only can be used. This gives more promising results, see [8, 29].
Interface-tracking is also of the Eulerian type. Interface-tracking uses the single-fluid flow equations combined with a mathematical model which tracks the location of the interface. Former versions of the tracking methods are the *marker and cell* [10], where massless particles are advected with the flow, and the *volume-of-fluid* [12], where a volume fraction is transported with the flow by means of an advection equation. A more recent approach is the *level-set* method. The level-set method uses a so-called *signed distance function* which is advected by the flow. All three methods suffer from spurious pressure oscillations. In [17] a simple fix for the level-set method is proposed to avoid these oscillations.
The focus of this report is on the interface-capturing method using two complete sets of flow equations, which are coupled by means of two fraction parameters. The advantage of this approach is the absence of pressure oscillations. For this method it is important to define what is meant by the word *interface*:

In reality the interface is a sharp boundary, which separates the two fluids in the flow. The interface is a discontinuity in the flow.
In the interface-capturing model, presented in this report, the interface acts as a transition region, in which the flow locally consists of a mixture of the two fluids. Here the interface is a continuous transition.

1.2 From general two-phase flow to two-fluid flow based on the Euler equations

In this work two-fluid flows are considered. This is already an approximation to the general two-phase flows. In general two-phase flows, each phase has its own density,

pressure, velocity and state. The phases exchange mass, momentum and energy due to mass transfer, exert forces and work onto each other and exchange heat with each other. To model these kind of flows, seven equations (two mass equations, two momentum equations, two energy equations and a topological equation to separate both) and seven closures are needed. These models, see e.g. [3], are seldom used due to their complexity[1]. In practice, there is a difference in pressure and velocity over the interface for only a small part of the time. To reduce the complexity of the model we make the following simplifications:

- the model is based on the Euler equations,
- the phases are immiscible,
- the velocities of both phases are equal, so $\mathbf{V}_1 = \mathbf{V}_2 = \mathbf{V}$,
- and the pressures of both phases are equal, so $p_1 = p_2 = p$.

By demanding zero relaxation of the pressure and velocity, the model reduces to five equations. The two phases still interact, they exert forces on each other which keep the velocities equal and they exchange work to keep the pressures equal. However, since Euler equations will be used, there is no heat exchange so there is in general no thermal equilibrium.
Although there is no definition of when to use the term two-phase and when to use two-fluid, we prefer to use the latter over here, because when a state changes from one phase to another, a transition process will occur, e.g. condensation or vaporization, see figure 1.2(a). In such a transition region, the behavior of the state, like the speed of sound $c^2 = \left(\frac{\partial p}{\partial \rho}\right)_s$, may be completely different from that of the two phases. In our model, such a transition state does not exist. Here the state in the interface transition layer will be modeled as a combination of both states, see figure 1.2(b). The speed of sound therefore changes monotonously when going from one phase to the other. By the

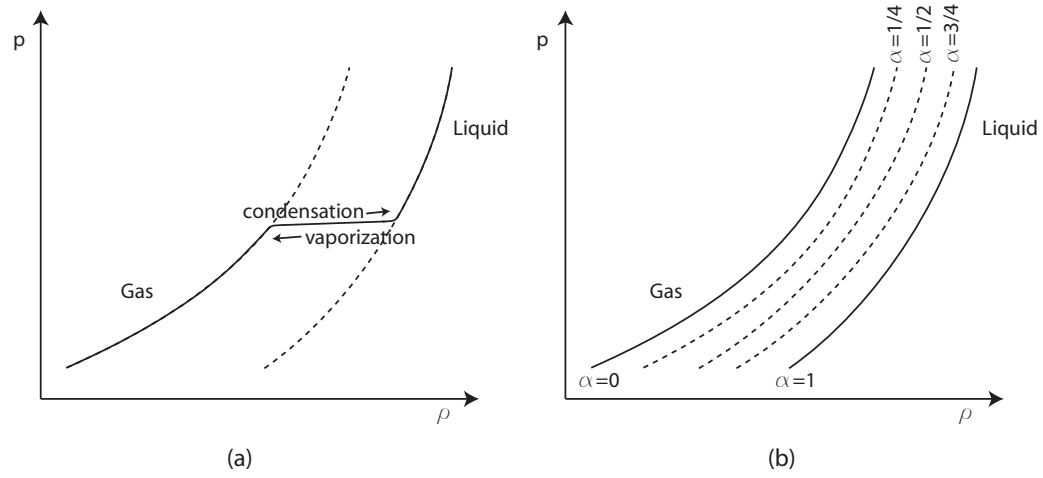

Figure 1.2: Pressure-density diagrams for two-phase flows (a) and two-fluid flows (b), with α being a volume fraction.

[1]These models are numerically complex to solve because of the large number of waves they contain and of the sensibility of the results with respect to the relaxation procedures.

absence of a phase change, both states are modeled as the same phase, namely fluid, with varying properties.
Some investigations in two-fluid models based on the Euler equations have already been done, see e.g. [7, 8, 20, 29], but they are not complete or use a combination of equations in conservative and advective form.

1.3 Research objectives

This thesis presents research done on unsteady compressible two-fluid flow. Three research objectives were defined:

- Derive a model for unsteady compressible two-fluid flow according to the given assumptions and derive a proper closure for the model.
- Discretize the model with a finite volume approximation. Develop for this purpose a discretization method for the closure of the model.
- Verify the model using several shock tube problems and two two-dimensional shock-bubble interaction benchmark cases.

Although beyond the aim of this research, an attempt is presented to derive relations that are valid for flows with discontinuities.

1.4 Thesis outline

This report is divided into three main parts. In part I, the flow model is derived and explained. Chapter 2 gives the derivation of the two-fluid model. Chapter 3 presents the derivation of the source term, to close the model. In chapter 4 attention is paid to flows with discontinuities.
In part II the flow solver is presented. Chapter 5 treats the finite-volume discretization of the model, chapter 6 treats the flux solver, in this case Osher's approximate Riemann solver, and in chapter 7 the derivation is presented how to integrate the source term for the given finite-volume discretization. The last chapter of part II is about the implementation of the discretization to the algorithm in chapter 8.
Part III accommodates the flow problems. Chapter 9 treats the one-dimensional flow problems and chapter 10 focuses on two shock-bubble interaction problems.
The final chapter gives the conclusions and some recommendations for future work on this topic. An appendix is added, to derive various formulations of the speed of sound.

Part I

Flow Model

Chapter 2

Two-fluid flow model

The two-fluid model is based on the unsteady compressible Euler equations. The Euler equations are simplifications of the Navier-Stokes equations. For the Euler equations viscosity and heat conduction are neglected. Euler flow simulations are especially valuable in flows with high Reynolds number and in flows which contain strong shocks or vorticity. In flows with high Reynolds number due to low viscosity, the viscous effects are only noticeable in the boundary layer. Such flows are therefore well described by the Euler equations. On the other hand, if the flow contains a strong shock or vorticity, simplification of the Euler equations to the potential equation is no longer valid.
Besides, the development of the two-fluid Euler model can be used as a preparatory stage for the development of a two-fluid Navier-Stokes model. The two-fluid Euler model will be derived in the next section.

2.1 Derivation of the two-fluid Euler model

Consider a control volume V. Let us imagine an infinitesimally small fluid element in this control volume with a differential volume $\mathrm{d}V$ which is fixed in space and time. For this fluid element we know three fundamental physical principles; conservation of mass, momentum and energy. In integral form this can be written as

$$\frac{\partial}{\partial t}\int_V \rho \mathrm{d}V + \int_S \rho \mathbf{V}\cdot\mathbf{n}\mathrm{d}S = 0, \tag{2.1}$$

$$\frac{\partial}{\partial t}\int_V \rho \mathbf{V}\mathrm{d}V + \int_S \rho \mathbf{V}\otimes\mathbf{V}\cdot\mathbf{n}\mathrm{d}S + \int_S p\,\mathbf{n}\mathrm{d}S = \mathbf{0}, \tag{2.2}$$

$$\frac{\partial}{\partial t}\int_V \rho E\mathrm{d}V + \int_S \rho E\mathbf{V}\cdot\mathbf{n}\mathrm{d}S + \int_S p\mathbf{V}\cdot\mathbf{n}\mathrm{d}S = 0. \tag{2.3}$$

Until now we did not look at the content of the fluid element. There can be two fluids present in this element. The pressure and velocity are constant over the two-fluid interface, but the density and total energy do not need to be constant over the interface. These have to be defined separately. Equations (2.1) to (2.3) are called the *bulk* equations containing two bulk quantities; bulk density and bulk total energy. These bulk quantities are a combination of the same quantities of fluid 1 and fluid 2.
For each fluid separately we can also write an equation for mass, momentum and energy. The momentum equation of a fluid separately is not treated here, because, as will be shown in chapter 3, it is already included in a combination of bulk mass equation (2.1), bulk momentum equation (2.2) and the mass equation of a separate fluid, like (2.4). This

is caused by the assumptions that velocity and pressure are constant over an interface. This in contrast to the energy equation, which is an independent equation, because we did not assume the temperature to be constant over the interface.
The mass of each fluid is conserved, since we assumed no mixing. We can write the conservation of mass of fluid 1 as

$$\frac{\partial}{\partial t}\int_{V_1(t)} \rho_1 \mathrm{d}V_1 + \int_{S_1(t)} \rho_1 \left(\mathbf{V} - \mathbf{V}_{S_1}\right)\cdot \mathbf{n}\mathrm{d}S_1 = 0. \tag{2.4}$$

The energy equation of a fluid is in general not conservative since there may be an exchange of energy between fluid 1 and fluid 2. For now this is indicated by a source term S, which represents a rate of energy exchange between the two fluids. This energy exchange is a result of both fluids, so S is integrated over the total volume. The energy equation of fluid 1 can be written as

$$\frac{\partial}{\partial t}\int_{V_1(t)} \rho_1 E_1 \mathrm{d}V_1 + \int_{S_1(t)} \rho_1 E_1 \left(\mathbf{V} - \mathbf{V}_{S_1}\right)\cdot \mathbf{n}\mathrm{d}S_1 + \int_{S_1(t)} p\mathbf{V}\cdot\mathbf{n}\mathrm{d}S_1 = \int_V S\mathrm{d}V. \tag{2.5}$$

In contrast to equations (2.1) to (2.3) the volume $V_1(t)$ and surface $S_1(t)$, over which we integrate the two equations above, are unknown and not constant in time. This is due to the moving interface, which moves with a velocity $\mathbf{V}_{S_1}$. By applying the divergence theorem to the surface integrals of equations (2.4) and (2.5) the unknown integration parameter $S_1(t)$ disappears and only the volume of fluid 1 $V_1(t)$ remains as an unknown. A new variable will be introduced to change from integrating over the unknown volume $V_1(t)$ to integrating over the known volume V. This is the volume fraction of fluid 1, defined as

$$\alpha = \frac{V_1}{V}. \tag{2.6}$$

Then of course $(1-\alpha)$ is the volume fraction of fluid 2. Substitute equation (2.6) into equations (2.4) and (2.5). Changing from a moving domain into a fixed domain causes V_{S_1} to become zero. Equations (2.4) and (2.5) result in

$$\frac{\partial}{\partial t}\int_V \alpha\rho_1 \mathrm{d}V + \int_V \nabla\cdot\alpha\rho_1\mathbf{V}\mathrm{d}V = 0, \tag{2.7}$$

$$\frac{\partial}{\partial t}\int_V \alpha\rho_1 E_1 \mathrm{d}V + \int_V \nabla\cdot\alpha\rho_1 E_1\mathbf{V}\mathrm{d}V + \int_V \nabla\cdot\alpha p\mathbf{V}\mathrm{d}V = \int_V S\mathrm{d}V. \tag{2.8}$$

We can derive the same kind of equations for fluid 2. If we add these to equations (2.7) and (2.8), they should result in the bulk equations (2.1) and (2.3). This gives us an expression for the bulk density and bulk total energy,

$$\rho = \alpha\rho_1 + (1-\alpha)\rho_2, \tag{2.9}$$

$$\rho E = \alpha\rho_1 E_1 + (1-\alpha)\rho_2 E_2, \tag{2.10}$$

with the total energy for each fluid defined as

$$E_1 = e_1 + \frac{1}{2}\mathbf{V}\cdot\mathbf{V}, \tag{2.11a}$$

$$E_2 = e_2 + \frac{1}{2}\mathbf{V}\cdot\mathbf{V}. \tag{2.11b}$$

The internal energies can be written as functions of the density of the fluid and the pressure, by introducing the equations of state. In general form they can be written as

$$e_1 = f(\rho_1, p), \tag{2.12a}$$
$$e_2 = f(\rho_2, p). \tag{2.12b}$$

Assuming that the source term S can be written as a combination of the already introduced variables, we can say that equations (2.12) close the system of equations.
Equations (2.1), (2.2), (2.3), (2.7) and (2.8) can also be written in differential form. These will become useful when deriving the source term. The equations become

$$\frac{\partial \rho}{\partial t} + \nabla \cdot \rho \mathbf{V} = 0, \tag{2.13}$$
$$\frac{\partial \rho \mathbf{V}}{\partial t} + \nabla \cdot \rho \mathbf{V} \otimes \mathbf{V} + \nabla p = \mathbf{0}, \tag{2.14}$$
$$\frac{\partial \rho E}{\partial t} + \nabla \cdot \rho E \mathbf{V} + \nabla \cdot p \mathbf{V} = 0, \tag{2.15}$$
$$\frac{\partial \alpha \rho_1}{\partial t} + \nabla \cdot \alpha \rho_1 \mathbf{V} = 0, \tag{2.16}$$
$$\frac{\partial \alpha \rho_1 E_1}{\partial t} + \nabla \cdot \alpha \rho_1 E_1 \mathbf{V} + \nabla \cdot \alpha p \mathbf{V} = S. \tag{2.17}$$

These equations can be cast into the general form, where, for two-dimensional, $\mathbf{F} = (\mathbf{f}, \mathbf{g})^T$ is the general flux vector:

$$\frac{\partial \mathbf{q}}{\partial t} + \nabla \cdot \mathbf{F}(\mathbf{q}) = \frac{\partial \mathbf{q}}{\partial t} + \frac{\partial \mathbf{f}(\mathbf{q})}{\partial x} + \frac{\partial \mathbf{g}(\mathbf{q})}{\partial y} = \mathbf{S}(\mathbf{q}), \tag{2.18}$$

with

$$\mathbf{q} = \begin{pmatrix} \rho \\ \rho u \\ \rho v \\ \rho E \\ \alpha \rho_1 \\ \alpha \rho_1 E_1 \end{pmatrix}, \ \mathbf{f} = \begin{pmatrix} \rho u \\ \rho u^2 + p \\ \rho u v \\ \rho u E + p u \\ \alpha \rho_1 u \\ \alpha \rho_1 E_1 u + \alpha p u \end{pmatrix}, \ \mathbf{g} = \begin{pmatrix} \rho v \\ \rho v u \\ \rho v^2 + p \\ \rho v E + p v \\ \alpha \rho_1 v \\ \alpha \rho_1 E_1 v + \alpha p v \end{pmatrix}, \ \mathbf{S} = \begin{pmatrix} 0 \\ 0 \\ 0 \\ 0 \\ 0 \\ S \end{pmatrix}.$$

We conclude that in general this system of equations is not fully conservative due to the rate of exchange in energy term. Consequences of this will be treated later in this report.

2.2 Boundary conditions

There are five different kind of boundary conditions possible for the Euler equations. This also holds for the presented two-fluid Euler model. These are: supersonic outflow, supersonic inflow, subsonic outflow, subsonic inflow and a solid wall / symmetry plane boundary condition. For each kind of boundary condition a number of the state variables $(\rho_1, \rho_2, u, v, p, \alpha)$ should be prescribed at the boundary. The number of state variables to be prescribed and the implementation of boundary conditions are described in more detail in chapter 6.

Chapter 3

Derivation of the source term

In equation (2.5) in the previous chapter a source term S was introduced. This source term expresses the rate of energy that is transferred from fluid 2 to fluid 1. In order to use the model presented in the previous chapter, it must still be closed by expressing the source term S in flow parameters.
The derivation of the source term in this chapter is done for flow away from any discontinuity. Therefore we may say that all derivatives of the flow parameters do exist. Flows containing discontinuities are considered in the next chapter.
In the first section the source term is split into two different types of work. Then work due to zero velocity relaxation and work due to zero pressure relaxation are derived.

3.1 Splitting the source term

This exchange in energy can only occur due to work, since there is no heat exchange and there are no viscous effects. We can distinguish two kinds of work. The first is mechanical work. In differential form this is given by:

$$\delta w = \mathbf{F} \cdot \mathrm{d}\mathbf{r}. \tag{3.1}$$

The source term S is defined as the rate of energy exchange, i.e. the rate of work:

$$\frac{\mathrm{d}w}{\mathrm{d}t} = \mathbf{F} \cdot \frac{\mathrm{d}\mathbf{r}}{\mathrm{d}t} = \mathbf{F} \cdot \mathbf{V}. \tag{3.2}$$

In our model, this force $\mathbf{F}$ is the source term in the momentum equation of fluid 1, $\mathbf{S}_M$. This term represents the force exerted by fluid 2 on fluid 1 and will be derived in the next section.
The second type of work is the thermodynamic work, which occurs when the volume of a fluid changes, like in a piston problem. In differential form this is given by:

$$\delta w = -p\mathrm{d}V. \tag{3.3}$$

Again we can take the time derivative, resulting in:

$$\frac{\mathrm{d}w}{\mathrm{d}t} = -p\frac{\mathrm{d}V}{\mathrm{d}t}. \tag{3.4}$$

This kind of work is represented by S_E. This term is added to system in the energy equation of fluid 1.
So the source term introduced in equation (2.5) can be split as

$$S = S_E + \mathbf{S_M} \cdot \mathbf{V}. \tag{3.5}$$

3.2 Zero velocity relaxation

The source term $\mathbf{S}_M$ can be found when applying zero velocity relaxation over the interface. This is done by saying that there is only one velocity $\mathbf{V}$. So the velocity in the momentum equation of fluid 1 and of fluid 2 and of the bulk must be the same. The bulk momentum equation is given by equation (2.14). The momentum equation of fluid 1 is given by:

$$\frac{\partial \alpha\rho_1\mathbf{V}}{\partial t} + \nabla\cdot\alpha\rho_1\mathbf{V}\otimes\mathbf{V} + \nabla(\alpha p) = \mathbf{S}_M. \tag{3.6}$$

$\mathbf{S}_M$ is a vector and its elements are the rate of momentum exchange from fluid 2 to fluid 1 in each direction. By expanding equation (3.6) and substituting (2.16), a primitive equation[1] for the velocity is found:

$$\frac{\mathrm{D}\mathbf{V}}{\mathrm{D}t} + \frac{1}{\alpha\rho_1}\nabla(\alpha p) = \frac{1}{\alpha\rho_1}\mathbf{S}_M. \tag{3.7}$$

The same can be done for the bulk momentum equation (2.14). Expand (2.14) and substitute (2.13), then we find another primitive equation for the velocity:

$$\frac{\mathrm{D}\mathbf{V}}{\mathrm{D}t} + \frac{1}{\rho}\nabla p = 0. \tag{3.8}$$

In order to keep the velocities of both fluids equal, the time and space derivatives of the velocities should also be equal. This results in:

$$-\frac{1}{\rho}\nabla p = \frac{1}{\alpha\rho_1}\left(-\nabla(\alpha p) + \mathbf{S}_M\right).$$

This expression can be rearranged for the source term in the momentum equation,

$$\mathbf{S}_M = \nabla(\alpha p) - \frac{\alpha\rho_1}{\rho}\nabla p = p\nabla\alpha + (\alpha-\beta)\nabla p, \tag{3.9}$$

where β is the mass fraction of fluid 1,

$$\beta = \frac{\alpha\rho_1}{\rho}. \tag{3.10}$$

The rate of energy exchange due to mechanical work in equation (2.5) becomes

$$\mathbf{S}_M\cdot\mathbf{V} = p\mathbf{V}\cdot\nabla\alpha + (\alpha-\beta)\,\mathbf{V}\cdot\nabla p. \tag{3.11}$$

3.3 Zero pressure relaxation

For the derivation of S_E more primitive equations of the flow variables are needed, so they will be derived first. The pressure relaxation is applied twice, first to find the last two primitive equations and second to find the source term due to zero pressure relaxation.

[1] a primitive equation is an equation for a state or primitive variable in the form of $\frac{\mathrm{D}\bullet}{\mathrm{D}t} + ... = 0$.

3.3.1 More primitive equations

The primitive equations are found when writing the conservative equations into non-conservative form. Some of the derivations are straightforward.
When expanding all terms of equation (2.13), it results in the primitive equation for the bulk density:

$$\frac{\mathrm{D}\rho}{\mathrm{D}t} + \rho\nabla\cdot\mathbf{V} = 0. \tag{3.12}$$

The primitive equation for the bulk internal energy is found by expanding all terms of equation (3.12) and substituting equations (2.15) and (3.8), which gives:

$$\frac{\mathrm{D}e}{\mathrm{D}t} + \frac{p}{\rho}\nabla\cdot\mathbf{V} = 0. \tag{3.13}$$

The equation for conservation of mass of fluid 1 leads to two kinds of primitive equations. At first, expanding equation (2.16) results in:

$$\frac{\mathrm{D}\rho_1}{\mathrm{D}t} + \frac{\rho_1}{\alpha}\frac{\mathrm{D}\alpha}{\mathrm{D}t} + \rho_1\nabla\cdot\mathbf{V} = 0. \tag{3.14}$$

The same can be found for fluid 2:

$$\frac{\mathrm{D}\rho_2}{\mathrm{D}t} - \frac{\rho_2}{1-\alpha}\frac{\mathrm{D}\alpha}{\mathrm{D}t} + \rho_2\nabla\cdot\mathbf{V} = 0. \tag{3.15}$$

Secondly, substituting equation (2.13) into equation (2.16) results in the primitive equation for the mass fraction:

$$\frac{\mathrm{D}\beta}{\mathrm{D}t} = 0. \tag{3.16}$$

This shows that the mass fraction is convected with the flow. The resulting force vector $\mathbf{S}_M$, equation (3.9), can be substituted into the momentum equation of fluid 1 (3.6),

$$\frac{\partial\beta\rho\mathbf{V}}{\partial t} + \nabla\cdot\beta\rho\mathbf{V}\otimes\mathbf{V} + \nabla(\alpha p) = p\nabla\alpha + (\alpha-\beta)\nabla p. \tag{3.17}$$

Substitution of equation (2.14) into (3.17) also gives the primitive equation for the mass fraction (3.16). This shows that the momentum equation for fluid 1 is not useful in our system of flow equations, since it is already present as a combination of the conservation equations of bulk mass (2.13), mass of fluid 1 (2.16) and the bulk momentum equation (2.14).
The last equation (2.17) in our system of equations contains the unknown source term. Substituting the result from the previous section, equation (3.9), into the energy equation of fluid 1 gives:

$$\frac{\partial\alpha\rho_1 E_1}{\partial t} + \nabla\cdot\alpha\rho_1 E_1\mathbf{V} + \nabla\cdot\alpha p\mathbf{V} = p\mathbf{V}\cdot\nabla\alpha + (\alpha-\beta)\,\mathbf{V}\cdot\nabla p + S_E.$$

Expand all the terms and substitute equations (2.16) and (3.8). This results in:

$$\frac{\mathrm{D}e_1}{\mathrm{D}t} + \frac{p}{\rho_1}\nabla\cdot\mathbf{V} = \frac{S_E}{\alpha\rho_1}. \tag{3.18}$$

The same can be found for fluid 2:

$$\frac{\mathrm{D}e_2}{\mathrm{D}t} + \frac{p}{\rho_2}\nabla\cdot\mathbf{V} = -\frac{S_E}{(1-\alpha)\rho_2}. \tag{3.19}$$

All these non-conservative formulations are needed for the derivations later in this chapter, and are also useful to find the characteristic equations in chapter 6.

3.3.2 Entropy relations

Using Euler equations instead of Navier-Stokes equations reduces the complexity of the model. Here non-adiabatic processes, like external heating, are neglected. Furthermore viscosity, heat conduction and mass diffusion are neglected and discontinuities are not considered here. This makes the model also reversible. Neglecting the non-adiabatic processes reduces the first law of thermodynamics, given by

$$\mathrm{d}e_i = \delta w_i + \delta q_i, \qquad \text{for} \quad i = 1, 2, \tag{3.20}$$

to

$$\mathrm{d}e_i = \delta w_i. \tag{3.21}$$

Equation (3.21) states that all work that is exerted on the system is converted to internal energy. This includes the work exerted by the source term. The second law of thermodynamics,

$$\mathrm{d}s_i \geq \frac{\delta q_i}{T_i}, \tag{3.22}$$

introduces an extra state variable, the *entropy*, s_i. Because the model of equation (2.13) to (2.17) is adiabatic and reversible for flows away from discontinuities and because the source term does not produce entropy, equation (3.22) reduces to

$$\mathrm{d}s_i = 0. \tag{3.23}$$

Equation (3.23) says that the model is isentropic everywhere in a continuous domain. Taking the substantial derivative of equation (3.23) gives

$$\frac{\mathrm{D}s_i}{\mathrm{D}t} = 0. \tag{3.24}$$

So the entropy is constant when moving with a fluid particle. Equation (3.24) does not only tell us more about the behavior of the flow, it is also useful to find more primitive equations, which will be useful later on. These are the primitive equations for the pressure and for the volume fraction. The derivation of these primitive equations starts with the definition of the speed of sound of each fluid,

$$c_i^2 = \left(\frac{\mathrm{d}p}{\mathrm{d}\rho_i}\right)_{s_i}, \tag{3.25}$$

and the fact that for reversible flow the entropy change can be related by:

$$\mathrm{d}s_i \propto \mathrm{d}p - c_i^2 \mathrm{d}\rho_i.$$

Substitute the above relation into equations (3.24):

$$\frac{\mathrm{D}p}{\mathrm{D}t} - c_1^2 \frac{\mathrm{D}\rho_1}{\mathrm{D}t} = 0, \tag{3.26a}$$

$$\frac{\mathrm{D}p}{\mathrm{D}t} - c_2^2 \frac{\mathrm{D}\rho_2}{\mathrm{D}t} = 0. \tag{3.26b}$$

Substitute the equations for conservation of mass of fluid 1 (2.16) and fluid 2 ((2.13)-(2.16)):

$$\frac{\mathrm{D}p}{\mathrm{D}t} + \rho_1 c_1^2 \left(\frac{1}{\alpha}\frac{\mathrm{D}\alpha}{\mathrm{D}t} + \nabla \cdot \mathbf{V}\right) = 0, \tag{3.27a}$$

$$\frac{\mathrm{D}p}{\mathrm{D}t} + \rho_2 c_2^2 \left(\frac{-1}{1-\alpha}\frac{\mathrm{D}\alpha}{\mathrm{D}t} + \nabla \cdot \mathbf{V}\right) = 0. \tag{3.27b}$$

The pressure and all its derivatives are equal over the interface for both fluids. Now we can apply it for the first time:

$$\frac{\mathrm{D}p}{\mathrm{D}t}(e_1, \rho_1) = \frac{\mathrm{D}p}{\mathrm{D}t}(e_2, \rho_2). \tag{3.28}$$

By eliminating the pressure derivatives, the primitive equation for the volume fraction is found:

$$\frac{\mathrm{D}\alpha}{\mathrm{D}t} + \varphi \nabla \cdot \mathbf{V} = 0, \tag{3.29}$$

with

$$\varphi = \alpha\,(1-\alpha)\,\frac{\rho_1 c_1^2 - \rho_2 c_2^2}{(1-\alpha)\,\rho_1 c_1^2 + \alpha \rho_2 c_2^2}.$$

The primitive equation for the pressure can be found by eliminating $\frac{\mathrm{D}\alpha}{\mathrm{D}t}$ from equations (3.27). This gives

$$\frac{\mathrm{D}p}{\mathrm{D}t} + \rho c^2 \nabla \cdot \mathbf{V} = 0, \tag{3.30}$$

with

$$\frac{1}{\rho c^2} = \frac{\alpha}{\rho_1 c_1^2} + \frac{1-\alpha}{\rho_2 c_2^2}.$$

For all variables which are used to derive the characteristic equations and the corresponding Riemann invariants (chapter 6), we found a primitive equation.

Let's take a closer look at equation (3.29). If we follow an element in the flow containing both fluids, then the mass-fraction, β, is convected with the flow. This is expected, because the element always consists of the same particles. Due to compression and expansion the volume of the element changes. To what extent the volume of each fluid will change depends on the compressibility of the fluids. A difference in compressibility of the fluids causes the change in volume fraction. Isentropic compressibility is defined as

$$\tau_{i_{s_i}} = -\frac{1}{\rho_i}\left(\frac{\partial \rho_i}{\partial p}\right)_{s_i} = \frac{1}{\rho_i c_i^2}. \tag{3.31}$$

Equation (3.29) can be rewritten to show the effect of compressibility on φ and thus the effect on the volume fraction,

$$\varphi = -\alpha(1-\alpha)\frac{\tau_{1_{s_1}} - \tau_{2_{s_2}}}{\tau_s}. \tag{3.32}$$

Suppose the flow element expands, then $\nabla \cdot \mathbf{V} > 0$. If fluid 1 is more compressible than fluid 2, so $\tau_1 > \tau_2$, then the volume fraction increases, while the mass fraction remains the same.

3.3.3 Thermodynamic relations

Above the relation for zero pressure relaxation (3.28) is used to eliminate pressure terms, in this section the pressure terms will be expanded in terms of its thermodynamic variables to find an expression for the source term added to the energy equation of fluid 1, S_E.

We start by repeating that the pressure and its time and space derivatives of both fluids on either side of the interface are equal:

$$\frac{\mathrm{D}p}{\mathrm{D}t}(e_1, \rho_1) = \frac{\mathrm{D}p}{\mathrm{D}t}(e_2, \rho_2).$$

The pressure derivatives can be expanded into the thermodynamic variables:

$$\left(\frac{\partial p}{\partial e_1}\right)_{\rho_1} \frac{\mathrm{D}e_1}{\mathrm{D}t} + \left(\frac{\partial p}{\partial \rho_1}\right)_{e_1} \frac{\mathrm{D}\rho_1}{\mathrm{D}t} = \left(\frac{\partial p}{\partial e_2}\right)_{\rho_2} \frac{\mathrm{D}e_2}{\mathrm{D}t} + \left(\frac{\partial p}{\partial \rho_2}\right)_{e_2} \frac{\mathrm{D}\rho_2}{\mathrm{D}t}.$$

Substituting equations (3.14), (3.15), (3.18) and (3.19), and rearranging it all gives:

$$S_E \left\{ \frac{1}{\alpha\rho_1} \left(\frac{\partial p}{\partial e_1}\right)_{\rho_1} + \frac{1}{(1-\alpha)\rho_2} \left(\frac{\partial p}{\partial e_2}\right)_{\rho_2} \right\} = \frac{\mathrm{D}\alpha}{\mathrm{D}t} \left\{ \frac{\rho_1}{\alpha} \left(\frac{\partial p}{\partial \rho_1}\right)_{e_1} + \frac{\rho_2}{1-\alpha} \left(\frac{\partial p}{\partial \rho_2}\right)_{e_2} \right\} + \left\{ \rho_1 \left(\frac{\partial p}{\partial \rho_1}\right)_{e_1} + \frac{p}{\rho_1} \left(\frac{\partial p}{\partial e_1}\right)_{\rho_1} - \rho_2 \left(\frac{\partial p}{\partial \rho_2}\right)_{e_2} - \frac{p}{\rho_2} \left(\frac{\partial p}{\partial e_2}\right)_{\rho_2} \right\} \nabla \cdot \mathbf{V}.$$

Again we make use of the speed of sound of each fluid, only now in the form of the thermodynamic variables used in the equations of state, which is derived in appendix A. This is given by:

$$c_i^2 = \left(\frac{\partial p}{\partial \rho_i}\right)_{s_i} = \left(\frac{\partial p}{\partial \rho_i}\right)_{e_i} + \frac{p}{\rho_i^2} \left(\frac{\partial p}{\partial e_i}\right)_{\rho_i}, \qquad \text{for } i = 1, 2.$$

Substitute the speed of sound of each fluid and rewrite everything to an equation for the source term due to zero pressure relaxation:

$$S_E = -p\frac{\mathrm{D}\alpha}{\mathrm{D}t} + \frac{\frac{\mathrm{D}\alpha}{\mathrm{D}t}\left(\frac{\rho_1 c_1^2}{\alpha} + \frac{\rho_2 c_2^2}{1-\alpha}\right) + \left(\rho_1 c_1^2 - \rho_2 c_2^2\right) \nabla \cdot \mathbf{V}}{\frac{1}{\alpha\rho_1}\left(\frac{\partial p}{\partial e_1}\right)_{\rho_1} + \frac{1}{(1-\alpha)\rho_2}\left(\frac{\partial p}{\partial e_2}\right)_{\rho_2}}.$$

The numerator of the second term is equal to the right hand side of equation (3.29), so the second term is equal to zero. This finally results in the expression for the source term due to pressure relaxation.

$$S_E = -p\frac{\mathrm{D}\alpha}{\mathrm{D}t}. \tag{3.33}$$

So by applying zero pressure relaxation, the pressure difference is compensated by a change in volume fraction. Equation (3.33) indeed corresponds with the definition of thermodynamic work, equation (3.4).

3.4 The final source term

Adding up equations (3.11) and (3.33) gives us the total energy exchange between fluid 2 and fluid 1:

$$\begin{aligned} S &= -p\frac{\mathrm{D}\alpha}{\mathrm{D}t} + p\mathbf{V} \cdot \nabla\alpha + (\alpha - \beta)\mathbf{V} \cdot \nabla p \\ &= -p\frac{\partial \alpha}{\partial t} + (\alpha - \beta)\mathbf{V} \cdot \nabla p. \end{aligned} \tag{3.34}$$

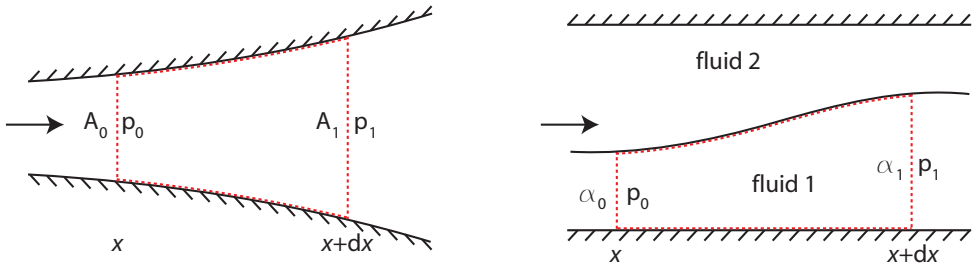

Figure 3.1: Similarity between channel flow problems with variable cross-section (a) and the two-fluid flow model (b).

The first line shows that the source term S consists of three terms. Each term has a specific contribution to the system. Below every term will be explained. The last two terms of equation (3.34) originate from the momentum equation, so for these terms only the force part will be explained.

$p\nabla\alpha$: This term is best explained by making a comparison with the channel flow equations with variable cross-section, see figure 3.1a. Then focus on the pressure integral of the momentum equation. For a channel flow with variable area, it can be written as

$$\int_S p\ \mathbf{n}\mathrm{d}S = p_1 A_1 - p_0 A_0 - \int_0^1 p\mathrm{d}A.$$

In differential form this becomes

$$p\ \mathbf{n}\mathrm{d}S = \mathrm{d}(pA) - p\mathrm{d}A.$$

Analogous to our two-fluid model, see figure 3.1b, we have the forces $\nabla(\alpha p)$ and $p\nabla\alpha$. The former represents the flux of the pressure force. The latter is a pressure force which counts for the increment in volume fraction.

$(\alpha - \beta)\nabla p$: Take for example an expansion. Then we know that the pressure drops ($\mathrm{d}p < 0$) and the velocity rises ($\mathrm{d}\mathbf{V} > 0$) when moving through an expansion, see e.g. equation (3.8). It shows that the amount of acceleration is opposite proportional to the density of the fluid. So when the density of fluid 1 is higher than that of fluid 2, $\alpha < \beta$, then the velocity of fluid 1 tends to be lower than that of fluid 2. Extra momentum is added to fluid 1 in the form of a pressure force. This momentum comes from fluid 2, of which the velocity tends to be too high. This exchange in momentum causes the fluids to gain the same velocity, namely the bulk velocity.

$-p\frac{\mathrm{D}\alpha}{\mathrm{D}t}$: This term looks already familiar, see e.g. equation (3.4). When a mixture of the two fluids is compressed or expanded, the two fluids do not compress or expand at the same rate because one is more compressible than the other. A pressure difference tends to occur over the interface. The term $-p\frac{\mathrm{D}\alpha}{\mathrm{D}t}$ exerts work on the interface which causes the interface to move, so that the pressure over the interface remains constant.

Chapter 4

Flow with discontinuities

In this chapter discontinuities, especially contact discontinuities and shocks, are considered. The model derived so far is not valid over discontinuities, where locally the derivatives of the state variables do not exist. To allow discontinuities in the flow, jump conditions have to be derived that describe the behavior of the flow over a discontinuity. This is not as straightforward as it is in single-fluid Euler flow. The source term of equation (2.17), given in equation (3.34), cannot be written in conservative form, which makes it less trivial to integrate the two-fluid model. In this chapter, contact discontinuities and shocks are treated separately because they require different solution methods. First however, jump conditions are introduced in more detail.
The derivations in this chapter are based on Wackers [28]. However the argumentation, especially in section 4.3, is different than that in [28].

4.1 Jump conditions

Consider a control volume around a discontinuity for the one-dimensional case. The flow on either side of the discontinuity is governed by the two-fluid Euler equations. We can integrate the system of equations of equation (2.18) over the control volume. The first four equations of our model are conservative, so they result in the well-known Rankine-Hugoniot condition

$$[\mathbf{f}] = c_s[\mathbf{q}], \tag{4.1a}$$

with $[.] = (.)_R - (.)_L$ expressing the jump between the states and with c_s representing the speed of the discontinuity. When integrating the fifth equation over the control volume an integral over the source term appears,

$$[\mathbf{f}] = c_s[\mathbf{q}] + \int_{x_L}^{x_R} S \mathrm{d}x. \tag{4.1b}$$

However, the spatial derivatives in S are not defined at the location of the discontinuity, so this integral cannot be evaluated in the normal way.

4.2 Contact discontinuity

First consider the contact discontinuity. For a contact discontinuity the velocity and pressure are constant. A constant pressure causes the source term due to pressure relaxation, $S_{E_{cd}}$, to be zero. A constant velocity reduces $S_{M_{cd}}$ to only the pressure force

that counts for the increment in volume fraction, $p\nabla\alpha$. The one-dimensional source term over a contact discontinuity becomes

$$S_{cd} = pu\frac{\partial\alpha}{\partial x}. \tag{4.2}$$

To calculate the integral we first have to express α as a function of x. Between x_L and x_R, the volume fraction has the shape of a heaviside function:

$$\alpha(x) = \alpha_L + (\alpha_R - \alpha_L)H(x). \tag{4.3}$$

The derivative of equation (4.3) introduces the Dirac delta:

$$\frac{\partial\alpha(x)}{\partial x} = (\alpha_R - \alpha_L)\delta(x). \tag{4.4}$$

Substitute equation (4.4) into equation (4.2) and use the definition of the Dirac delta:

$$\int_{-\epsilon}^{+\epsilon} \delta(t)\mathrm{d}t = 1, \quad \text{for} \quad \epsilon > 0,$$

then the contribution of the source term to the jump relations is given by:

$$\int_{x_L}^{x_R} S_{cd}\mathrm{d}x = pu\,(\alpha_R - \alpha_L) = pu[\alpha]. \tag{4.5}$$

Equations (4.1) and equation (4.5) together give the jump relations over a contact discontinuity.

4.3 Shock wave

For a shock evaluation of the integral is not possible. Another method, proposed in [28], is used. Suppose that the flow is a weak solution of the system if it is the inviscid and non-heat-conducting limit of the solution of the system with viscous effects, τ, and heat conduction, Q, added. This implies two things. One, that the solution is irreversible, and two, that the discontinuity has some internal structure. The latter makes it possible to integrate the source term through the shock.
We examine the shock in the shock frame. Here the flow is steady. The velocity u is replaced by $\tilde{u} = u - c_s$. The control volume over which we integrate is shown in figure 4.1, where x lies somewhere in the shock domain. Outside of the shock we consider $\frac{\partial\tau}{\partial x}$ and $\frac{\partial Q}{\partial x}$ to be zero. Integrating the system of equations over the control volume gives

$$\rho\tilde{u} = \rho_L\tilde{u}_L, \tag{4.6a}$$

$$\rho\tilde{u}^2 + p - \tau = \rho_L\tilde{u}_L^2 + p_L, \tag{4.6b}$$

$$\rho\tilde{u}(e + \frac{1}{2}\tilde{u}^2) + (p-\tau)\tilde{u} - Q = \rho_L\tilde{u}_L(e_L + \frac{1}{2}\tilde{u}_L^2) + p_L\tilde{u}_L, \tag{4.6c}$$

$$\beta\rho\tilde{u} = \beta_L\rho_L\tilde{u}_L, \tag{4.6d}$$

$$\beta\rho\tilde{u}(e_1 + \frac{1}{2}\tilde{u}^2) + (p-\tau_1)\alpha\tilde{u} - \alpha Q_1 = \beta_L\rho_L\tilde{u}_L(e_{1,L} + \frac{1}{2}\tilde{u}_L^2) + \alpha_L p_L\tilde{u}_L + \int_{x_L}^{x} S_s\mathrm{d}x. \tag{4.6e}$$

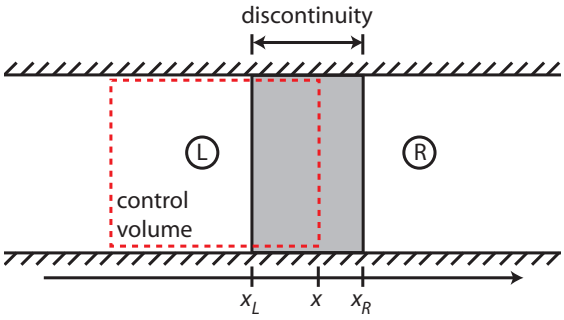

Figure 4.1: Control volume over a discontinuity with finite thickness

The internal structure of the shock depends on the viscous stress, τ_i, and heat conduction, Q_i, of each fluid. The viscous stresses and heat conductions determine among others the thickness of the shock and the entropy distribution through the shock. However the internal structure is not of interest here, because we are only interested in the jump relations over the shock. The viscous stresses and heat conductions are *assumed* to have no effect on the jump of the state variables over the shock, as in single-fluid flow. This assumption is the basis of the derivation. Considering this assumption we can use that:

- The viscous stress and heat conduction of both fluids can be taken the same, so $\tau_1 = \tau_2 = \tau$ and $Q_1 = Q_2 = Q$.

- Taking the limits $\tau \to 0$ and $Q \to 0$, only effects the internal structure of the shock and not the jump relations over the shock.

Furthermore, since the thickness of the shock is of no interest, it is more useful to write the state variables as a function of $\tilde{u}$ instead of x. With this and the two assumptions, a set of ordinary differential equations will be derived. These can be integrated numerically from $\tilde{u}_L$ to $\tilde{u}_R$. While the value $\tilde{u}_L$ is known, $\tilde{u}_R$ is not. We do know that $\frac{\partial \tilde{u}}{\partial x}|_R = 0$ and that the viscous stress τ is proportional to $\frac{\partial \tilde{u}}{\partial x}$. Therefore the limit $\tau \to 0$ is not used, but τ remains in the system of equations, to measure when the state at the right side of the shock is reached, i.e. where $\tau = 0$.
The source term in equation (4.6e) is integrated over a certain domain x. This requires a change in integration parameter. Before doing this, the source term itself must be reconsidered. The source term S_s differs from the source term derived in the previous chapter, because of the viscous stress that is added to the system. Again two relaxations are applied. The same method for the velocity relaxation as in section 3.2 now results in

$$S_{M_s} = (p - \tau)\frac{\partial \alpha}{\partial x} + (\alpha - \beta)\frac{\partial (p - \tau)}{\partial x}. \tag{4.7}$$

In section 3.3.3 zero relaxation was applied to the pressure. Now the term $p - \tau$ works as a stress on the flow. Therefore we apply zero relaxation to $p - \tau$. This results in

$$S_{E_s} = -(p - \tau)\frac{\mathrm{D}\alpha}{\mathrm{D}t} = -(p - \tau)\left(\frac{\partial \alpha}{\partial t} + \tilde{u}\frac{\partial \alpha}{\partial x}\right). \tag{4.8}$$

Because the shock frame is used, the flow is steady and thus $\frac{\partial \alpha}{\partial t}$ equals zero. The complete source term inside the shock, with the assumptions given above, becomes

$$S_s = (\alpha - \beta)\tilde{u}\frac{\partial(p-\tau)}{\partial x}. \tag{4.9}$$

To be able to change the integration parameter in equation (4.6e) to $\tilde{u}$, the spatial derivative in equation (4.9) must be rewritten. This is done by differentiating equation (4.6b) to x. This gives

$$\frac{\partial(p-\tau)}{\partial x} = -\rho_L \tilde{u}_L \frac{\partial \tilde{u}}{\partial x}. \tag{4.10}$$

Hence,

$$S_s = -\rho \tilde{u}_L(\alpha - \beta)\tilde{u}\frac{\partial \tilde{u}}{\partial x}. \tag{4.11}$$

So, the source term is independent of the viscous stress. Equations (4.6) can now be rewritten as

$$\rho = \frac{\rho_L \tilde{u}_L}{\tilde{u}}, \tag{4.12a}$$

$$p - \tau = \rho_L \tilde{u}_L(\tilde{u}_L - \tilde{u}) + p_L, \tag{4.12b}$$

$$\rho_L \tilde{u}_L\left[e - \frac{1}{2}\tilde{u}^2 + \tilde{u}_L\tilde{u}\right] + p_L\tilde{u} = \rho_L\tilde{u}_L(e_L + \frac{1}{2}\tilde{u}_L^2) + p_L\tilde{u}_L, \tag{4.12c}$$

$$\beta = \beta_L, \tag{4.12d}$$

$$\rho_L\tilde{u}_L\left[\beta_L(e_1 + \frac{1}{2}\tilde{u}^2) + \alpha(\tilde{u}_L\tilde{u} - \tilde{u}^2)\right] + \alpha p_L\tilde{u} + \rho_L\tilde{u}_L\int_{\tilde{u}_L}^{\tilde{u}}(\alpha - \beta_L)\tilde{u}\mathrm{d}\tilde{u} =$$
$$\beta_L\rho_L\tilde{u}_L(e_{1,L} + \frac{1}{2}\tilde{u}_L^2) + \alpha_L p_L\tilde{u}_L. \tag{4.12e}$$

The integral can be removed by differentiating equation (4.12e) to $\tilde{u}$. If we also differentiate equations (4.12a), (4.12c), (4.12d) and the internal energies e and e_1 to $\tilde{u}$, we find a complete set of six differential equations, with six different derivatives with respect to $\tilde{u}$. The first four become:

$$\frac{\partial \rho}{\partial \tilde{u}} = -\frac{\rho_L \tilde{u}_L}{\tilde{u}^2}, \tag{4.13a}$$

$$\rho_L\tilde{u}_L\left(\frac{\partial e}{\partial \tilde{u}} + \tilde{u}_L - \tilde{u}\right) + p_L = 0, \tag{4.13b}$$

$$\frac{\partial \beta}{\partial \tilde{u}} = 0, \tag{4.13c}$$

$$\rho_L\tilde{u}_L\left[\beta_L\frac{\partial e_1}{\partial \tilde{u}} + \alpha\left(\tilde{u}_L - \tilde{u}\right) + \left(\tilde{u}_L\tilde{u} - \tilde{u}^2\right)\frac{\partial \alpha}{\partial \tilde{u}}\right] + p_L\left(\alpha + \tilde{u}\frac{\partial \alpha}{\partial \tilde{u}}\right) = 0. \tag{4.13d}$$

For the derivation of derivative of the bulk internal energy, e, we can rewrite equation (2.10) as

$$e = \beta e_1 + (1-\beta)e_2. \tag{4.14}$$

Substitute the general equations of state (2.12) and use equation (3.10) to relate the bulk density, ρ, with the density for a single fluid, ρ_i. Differentiate equation (4.14) and

use the chain rule. Do the same for internal energy, e_1. This results in the following two equations:

$$\begin{aligned}\frac{\partial e}{\partial \tilde{u}} = &\left[e_1 - e_2 + \frac{\beta}{\alpha}\rho\frac{\partial e_1}{\partial \rho_1} + \frac{1-\beta}{1-\alpha}\rho\frac{\partial e_2}{\partial \rho_2}\right]\frac{\partial \beta}{\partial \tilde{u}} + \left[\beta\frac{\partial e_1}{\partial p} + (1-\beta)\frac{\partial e_2}{\partial p}\right]\frac{\partial p}{\partial \tilde{u}} \\ &+ \left[\frac{\beta^2}{\alpha}\frac{\partial e_1}{\partial \rho_1} + \frac{(1-\beta)^2}{1-\alpha}\frac{\partial e_2}{\partial \rho_2}\right]\frac{\partial \rho}{\partial \tilde{u}} + \left[-\frac{\beta^2}{\alpha^2}\rho\frac{\partial e_1}{\partial \rho_1} + \frac{(1-\beta)^2}{(1-\alpha)^2}\rho\frac{\partial e_2}{\partial \rho_2}\right]\frac{\partial \alpha}{\partial \tilde{u}},\end{aligned} \tag{4.15a}$$

$$\frac{\partial e_1}{\partial \tilde{u}} = \frac{\partial e_1}{\partial p}\frac{\partial p}{\partial \tilde{u}} + \frac{\partial e_1}{\partial \rho_1}\left[\frac{1}{\alpha}\rho\frac{\partial \beta}{\partial \tilde{u}} + \frac{\beta}{\alpha}\frac{\partial \rho}{\partial \tilde{u}} - \frac{\beta}{\alpha^2}\rho\frac{\partial \alpha}{\partial \tilde{u}}\right]. \tag{4.15b}$$

Equations (4.13) and (4.15) together give a set of differential equations, which contains six different derivatives with respect to $\tilde{u}$. After a lot of rewriting an ordinary differential equation appears that gives $\frac{\partial \alpha}{\partial \tilde{u}}$ as function of α and $\tilde{u}$ only,

$$\frac{\partial \alpha}{\partial \tilde{u}} = \frac{\left[\begin{array}{l} -\beta_L(1-\beta_L)\frac{\rho_L \tilde{u}_L}{\tilde{u}^2}\frac{\frac{\beta_L}{\alpha}\frac{\partial e_1}{\partial \rho_1}\frac{\partial e_2}{\partial p} - \frac{1-\beta_L}{1-\alpha}\frac{\partial e_2}{\partial \rho_2}\frac{\partial e_1}{\partial p}}{\beta_L\frac{\partial e_1}{\partial p} + (1-\beta_L)\frac{\partial e_2}{\partial p}} + \alpha(\tilde{u}_L - \tilde{u}) \\ \qquad + \left(\tilde{u} - \tilde{u}_L - \frac{p_L}{\rho_L \tilde{u}_L}\right)\frac{\beta_L\frac{\partial e_1}{\partial p}}{\beta_L\frac{\partial e_1}{\partial p} + (1-\beta_L)\frac{\partial e_2}{\partial p}} + \frac{\alpha p_L}{\rho_L \tilde{u}_L} \end{array}\right]}{-\beta_L(1-\beta_L)\frac{\rho_L \tilde{u}_L}{\tilde{u}}\frac{\frac{\beta_L}{\alpha^2}\frac{\partial e_1}{\partial \rho_1}\frac{\partial e_2}{\partial p} + \frac{1-\beta_L}{(1-\alpha)^2}\frac{\partial e_2}{\partial \rho_2}\frac{\partial e_1}{\partial p}}{\beta_L\frac{\partial e_1}{\partial p} + (1-\beta_L)\frac{\partial e_2}{\partial p}} + \tilde{u}(\tilde{u}_L - \tilde{u}) + \frac{p_L \tilde{u}}{\rho_L \tilde{u}_L}}. \tag{4.16}$$

Integrating equation (4.16) numerically results in the volume fraction distribution. Equation (4.12a) gives the bulk density distribution. With the volume fraction and bulk density distribution, equation (4.12c) and the equations of state, the pressure distribution can be calculated. The mass fraction directly results from equation (4.12d). The right state is found with

$$\left.\begin{aligned}\tau &= \rho_L \tilde{u}_L(\tilde{u} - \tilde{u}_L) + p - p_L \\ \tau &= 0\end{aligned}\right\} \quad \Rightarrow \quad \mathbf{q} = \mathbf{q}_R. \tag{4.17}$$

Now that the state at the right side of the shock is found, the jump in state variables over the shock is known.

The method that is presented here results in a set of equations that is independent of x, independent of the heat conductions and also independent of viscosities. The latter, because only the velocity derivative, $\frac{\partial \tilde{u}}{\partial x}$, is of interest in the viscous stress, τ.

Important to notice is that for the distributions of the state variables through the shock, only one point (excluding the left state) is correct for sure, namely the right state $\mathbf{q}_R$. The state distributions between the left and right state are most likely incorrect. Fortunately, for the Rankine-Hugoniot conditions we are only interested in the left and right state of the shock.

4.4 Remark

The development of jump conditions for the two-fluid model was beyond the scope of this research. Therefore the jump conditions are not used in the numerical solver. Moreover, due to limited time, we were not able to test the jump conditions. This is therefore added to the list of recommendations given in section 11.2.

Wackers [28] obtained the same jump conditions. He did perform some tests on several shock tube problems, as in chapter 9, using an exact Riemann solver. For a shock, the Riemann solver used the jump conditions described in section 4.3. The results were similar to those in chapter 9, indicating that the method does work.

Part II

Flow Solver

Chapter 5

Finite-Volume Discretisation

The exact solution of the two-fluid Euler model is not known in nearly all cases. As an approximation the system will be discretized, replacing the continuous equations by a system of equations with a finite number of unknowns. A popular method in computational fluid dynamics is the finite-volume method, mainly because of two advantages. First, finite-volume methods ensure that the discretization is conservative. Second, the finite-volume method can be applied on unstructured meshes (Lomax [15]).
Finite-volume methods use the integral form of the governing equations. This integral formulation will be approximated by dividing the computational domain Ω into several subdomains $\Omega_{i,j}$. For the time-derivative the family of Runge-Kutta schemes will be introduced and for the space-descretization the MUSCL method with two types of limiters will be used.

5.1 Integral formulation

Integrate equation (2.18) over an element Ω of arbitrary shape and size:

$$\int_\Omega \frac{\partial \mathbf{q}}{\partial t} \mathrm{d}\Omega + \int_\Omega \nabla \cdot \mathbf{F} \mathrm{d}\Omega = \int_\Omega \mathbf{S} \mathrm{d}\Omega. \tag{5.1}$$

In general the solution of the Euler equations contains several kinds of continuous and discontinuous waves. Over these discontinuous waves the Euler equations in the form of (5.1) are not valid. We therefore apply Gauss's divergence theorem to the second integral, so that $\mathbf{F}$ no longer has to be spatial-differentiable. Looking at the first integral, the domain Ω does not change its shape during a time integration, so the space integration and the time derivative are interchangeable. This results in:

$$\frac{\partial}{\partial t} \int_\Omega \mathbf{q} \mathrm{d}\Omega + \oint_\Gamma \mathbf{F} \cdot \mathbf{n} \mathrm{d}\Gamma = \int_\Omega \mathbf{S} \mathrm{d}\Omega. \tag{5.2}$$

$\mathbf{n} = (n_x, n_y)^T$ is the unit normal vector to the boundary of the domain.

5.2 Finite-volume approximation

In a finite-volume approximation the domain Ω is divided into a finite number of non-overlapping domains $\Omega_{i,j}$, called cells. Although unstructured meshes can be used, in

this report only rectangular cells are used. Each cell center has an average state $\mathbf{q}_{i,j}$. Here the problem is reduced to a finite number of unknowns.

$$\int_{\Omega_{i,j}} \mathbf{q} \mathrm{d}\Omega = \Delta x \Delta y \mathbf{q}_{i,j}, \tag{5.3}$$

Instead of a flux distribution over a cell face, it will be approximated by a single flux per cell face. Van der Maarel [24] has shown that this limits the accuracy to second-order, by:

$$\begin{aligned} \frac{1}{\Delta y} \int_{\Gamma_{i\pm\frac{1}{2},j}} \mathbf{f}(\mathbf{q}) \mathrm{d}y &= \mathbf{f}\left(\frac{1}{\Delta y} \int_{\Gamma_{i\pm\frac{1}{2},j}} \mathbf{q} \mathrm{d}y \right) + \mathcal{O}\left(\Delta x^2, \Delta y^2\right) \\ &= \mathbf{f}_{i\pm\frac{1}{2},j} + \mathcal{O}\left(\Delta x^2, \Delta y^2\right). \end{aligned} \tag{5.4}$$

This results into the discretized form of equation (2.18), as a result of the finite volume approximation:

$$\frac{\partial \mathbf{q}_{i,j}}{\partial t} + \frac{1}{\Delta x}\left[\mathbf{f}_{i+\frac{1}{2},j} - \mathbf{f}_{i-\frac{1}{2},j}\right] + \frac{1}{\Delta y}\left[\mathbf{g}_{i,j+\frac{1}{2}} - \mathbf{g}_{i,j-\frac{1}{2}}\right] = \frac{1}{\Delta x \Delta y} \int_{\Omega_{i,j}} S \mathrm{d}\Omega. \tag{5.5}$$

The source integral will be treated separately in chapter 7.

5.3 Space discretization

The order of accuracy of the spatial discretization is determined by the way the states at the left and the right side of the cell face are calculated. Above it was stated that the value at the cell center is equal to the average state over the cell. While this value is quite accurate for the cell center, it is less accurate near the cell faces. Using the states in the cell center for determining the fluxes results in a first-order accurate solution. First-order accuracy is insufficient for practical applications and therefore a higher-order method is necessary. Van Leer [25] introduced the idea of modifying the piecewise constant data in the first-order method, to achieve higher-order of accuracy. This approach is known as the MUSCL (Monotone Upstream-centred Scheme for Conservation Laws). At first it implies a data reconstruction to obtain higher-order accuracy. Secondly the reconstruction is constrained to avoid spurious oscillations. These two steps are done separately for every direction. In this paragraph it is explained for the x-direction. For any other direction it can be done in a similar way.

5.3.1 Data reconstruction

The simplest way of modifying the piecewise constant data is to replace the constant states by piecewise linear functions. The only locations that we are really interested in are the values at the cell faces. They are called *boundary extrapolated values* and are given by:

$$\mathbf{w}^L_{i+\frac{1}{2},j} = \mathbf{w}_{i,j} + \frac{1}{2}\delta\mathbf{w}_{i,j}, \tag{5.6a}$$

$$\mathbf{w}^R_{i-\frac{1}{2},j} = \mathbf{w}_{i,j} - \frac{1}{2}\delta\mathbf{w}_{i,j}, \tag{5.6b}$$

where $\mathbf{w} = (\rho, u, v, p, \alpha, \beta)$ and $\delta\mathbf{w}$ is the slope of the interpolation. Data reconstruction is performed on the primitive variables instead of the conservative, because this gives a more accurate result, see [29].
A consequence of having modified the data is that at each cell face one may now consider a so-called *Generalised Riemann Problem* (GRP) to compute the flux. This results in wave paths that are curved in the x, t-plane. Naturally, for non-linear systems the exact solution of the GRP is exceedingly complicated, but for the purpose of flux evaluation, approximate information may be obtained. Most approaches do in fact give up the solution of the GRP and rely instead on use of the boundary extrapolated values. In this way, one may instead consider the piece-wise constant data Riemann problem.
A well-known scheme for the slope $\delta\mathbf{w}$ is the family of κ-schemes of Van Leer [26],

$$\delta\mathbf{w}_{i,j} = \frac{1+\kappa}{2}(\mathbf{w}_{i+1,j} - \mathbf{w}_{i,j}) + \frac{1-\kappa}{2}(\mathbf{w}_{i,j} - \mathbf{w}_{i-1,j}). \tag{5.7}$$

For $\kappa = \frac{1}{3}$ the scheme of (5.6) becomes third-order accurate. The κ-schemes work fine in the smooth parts of the flow, but will lead to spurious oscillations around discontinuities. Godunov [6] has shown that wiggles always occur when using higher than first-order schemes. As a remedy against these spurious non-monotonicities, *limited* schemes are proposed.

5.3.2 Limiters

In general limiter schemes are given by:

$$\mathbf{w}^R_{i-\frac{1}{2},j} = \mathbf{w}_{i,j} + \frac{1}{2}\phi\left(r^R_{i,j}\right)(\mathbf{w}_{i,j} - \mathbf{w}_{i+1,j}), \qquad \text{with} \quad r^R_{i,j} = \frac{\mathbf{w}_{i-1,j} - \mathbf{w}_{i,j}}{\mathbf{w}_{i,j} - \mathbf{w}_{i+1,j}}, \tag{5.8a}$$

$$\mathbf{w}^L_{i+\frac{1}{2},j} = \mathbf{w}_{i,j} + \frac{1}{2}\phi(r^L_{i,j})(\mathbf{w}_{i,j} - \mathbf{w}_{i-1,j}), \qquad \text{with} \quad r^L_{i,j} = \frac{\mathbf{w}_{i+1,j} - \mathbf{w}_{i,j}}{\mathbf{w}_{i,j} - \mathbf{w}_{i-1,j}}, \tag{5.8b}$$

in which $\phi(r)$ is some limiter. To have a second-order accurate discretization, the limiter function must satisfy $\phi(1) = 1$. Futhermore Sweby [23] introduced a monotonicity domain in which the limiter function should lie. This domain was later extended by Spekreijse [22]. The monotonicity domain is highlighted in figure 5.1.
A well-known and rather simple limiter is the *minmod* limiter, which is given by:

$$\phi(r) = \max\left(0, \min\left(1, r\right)\right). \tag{5.9}$$

If $\phi(r) = 1$, then the scheme is equal to the upwind scheme (equal to the $\kappa = -1$ scheme of equation (5.7)), if $\phi(r) = r$, then the scheme is equal to the central scheme (equal to the $\kappa = 1$ scheme) and if $\phi(r) = 0$, the scheme is first-order accurate.
For this report the *Koren* limiter is used [14]. It is based on the $\kappa = \frac{1}{3}$ scheme, for which it tries to follow for a as large as possible range of r. The limiter is given by:

$$\phi(r) = \max\left(0, \min\left(2r, \min\left(\frac{1}{3} + \frac{2}{3}r, 2\right)\right)\right). \tag{5.10}$$

For $\phi(r) = \frac{1}{3} + \frac{2}{3}r$ the scheme is equal to the $\kappa = \frac{1}{3}$ scheme which is third-order accurate. Both limiters are displayed in a Sweby diagram in figure 5.1.

The cells at the boundaries need special attention, because equation (5.8) is not applicable here. For the most left cell the limiters are given by:

$$\phi\left(r^R_{\frac{1}{2},j}\right) = 0, \qquad \Rightarrow \qquad \mathbf{w}^R_{\frac{1}{2},j} = \mathbf{w}_{1,j}, \tag{5.11a}$$

$$\phi(r^L_{1\frac{1}{2},j}) = r^L_{1\frac{1}{2},j}, \qquad \Rightarrow \qquad \mathbf{w}^L_{1\frac{1}{2},j} = \frac{1}{2}\left(\mathbf{w}_{2,j} + \mathbf{w}_{1,j}\right), \tag{5.11b}$$

and for the most right cell the limiter is given by:

$$\phi\left(r^R_{n-\frac{1}{2},j}\right) = r^R_{n-\frac{1}{2},j}, \qquad \Rightarrow \qquad \mathbf{w}^R_{n-\frac{1}{2},j} = \frac{1}{2}\left(\mathbf{w}_{n,j} + \mathbf{w}_{n-1,j}\right), \tag{5.12a}$$

$$\phi(r^L_{n+\frac{1}{2},j}) = 0, \qquad \Rightarrow \qquad \mathbf{w}^L_{n+\frac{1}{2},j} = \mathbf{w}_{n,j}. \tag{5.12b}$$

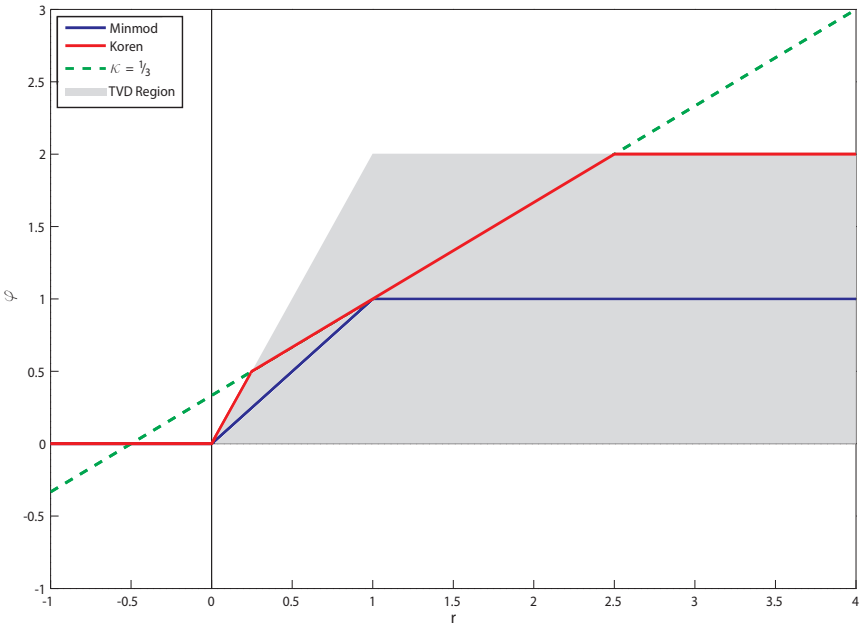

Figure 5.1: Sweby's TVD diagram with Minmod and Koren limiter

5.4 Time discretization

The system of equations is unsteady, so the state variables also have to be discretized in time. Because space- and time-discretization can be treated separately, the system to be solved can be written as:

$$\frac{\mathrm{d}}{\mathrm{d}t}\mathbf{q} = \mathbf{L}\left(\mathbf{q}\right), \tag{5.13}$$

where $\mathbf{L}(\mathbf{q})$ represents the terms which do not contain a time-derivative. This includes the source term of equation (3.34), because, as will be shown in chapter 7, the $\frac{\partial \alpha}{\partial t}$ term will be replaced by terms containing only spatial derivatives.
The average states $\mathbf{q}_{i,j}$ are calculated only at discrete time levels n lying Δt apart. Over the past many time-discretization methods have been developed, starting from the well-known forward Euler, which is first-order, to higher-order schemes. While the first is

very easy to implement, its accuracy is much lower than the latter and also an order lower than the space discretization. Therefore a higher-order method is preferred. In general two approaches are possible to reach higher-order time accuracy, by multi-stage or multi-step schemes. The first calculate intermediate stages to find the solution at the next time-level, for example the family of Runge-Kutta schemes, while the second use the solutions at multiple time-levels to calculate the solution at the new time-level, e.g. the leapfrog method and the family of Backward Difference Formulas.
Here the multi-stage method is chosen, in the form of the Explicit Runge-Kutta methods ERK1 (equal to forward Euler), ERK2b and ERK3b. These are rather easy to implement and have already proven to be useful for the Euler equations [13].
The family of Explicit Runge-Kutta schemes is given by:

$$\begin{aligned} \mathbf{q}^{(0)} &= \mathbf{q}^n, \\ \mathbf{q}^{(k)} &= \mathbf{q}^{(0)} + \sum_{m=0}^{k-1} \eta_{km} \Delta t \mathbf{L}\left(\mathbf{q}^{(m)}\right), \quad k = 1, \ldots, p, \\ \mathbf{q}^{n+1} &= \mathbf{q}^{(p)}, \end{aligned} \tag{5.14}$$

where p is the order of the scheme and η_{km} is a coefficient tabulated in table 5.1.

Name	Order p	Coeff. η_{km}		
ERK1	1	1		
ERK2b	2	1 1/2	- 1/2	
ERK3b	3	1 1/4 1/6	- 1/4 1/6	- - 2/3

Table 5.1: Coefficients for the Runge-Kutta scheme

5.5 Stability requirement

Numerical stability is an important property of the numerical scheme. It determines if numerical errors grow or reduce in time. The stability requirement limits the possible size of the timestep Δt. Numerical stability is expressed by the Courant number, which for our 2D model can be written as:

$$C = \max\left(\max_{\forall i,j,k}\left|(\lambda_k)_{i+\frac{1}{2},j}\right|\frac{\Delta t}{\Delta x}\,,\ \max_{\forall i,j,k}\left|(\lambda_k)_{i,j+\frac{1}{2}}\right|\frac{\Delta t}{\Delta y}\right), \tag{5.15}$$

where λ_k is a wave speed of the model, which is dealt with in more detail in the next chapter.
In Hundsdorfer et al. [13] it is shown that for a discretization using both limiters and explicit Runge-Kutta schemes, the solution is stable if

$$C \leq \frac{1}{1+\delta/2},$$

where δ equals the upper limit of the limiter function $\phi(r)$. For Sweby's TVD domain it holds $\delta = 2$, resulting in a stability requirement according to [13] of

$$C \leq \frac{1}{2}. \tag{5.16}$$

Chapter 6

Osher's Approximate Riemann Solver

To find the numerical fluxes over the cell faces, so called Riemann problems have to be solved. A Riemann problem is an initial value problem containing two initial states which are separated by a discontinuity. The solution of a Riemann problem is a combination of shocks, expansion waves and a contact discontinuity. In the begin of this thesis work we assumed that it is not possible to define Rankine-Hugoniot relations over a shock for the proposed system of equations[1]. Therefore an approximate Riemann solver had to be used. Osher's approximate Riemann solver is used, because it only makes an approximation for handling shocks. Osher's solver uses isentropic relations to calculate both expansions and shocks. For expansions the solver is still exact, since these are isentropic. Shocks are approximated by isentropic compression waves. For weak shocks this approximation is still pretty accurate, because the production of entropy in a shockwave is of $\mathcal{O}\left(\Delta u^3\right)$.
Although Osher's solver is not new and already presented in several master thesis reports, e.g. [27], it useful to present the elements on which the solver is based. The system of equations presented in this report require some modifications to the implementation compared to the standard Euler equations. Futhermore for the integration of the source term in chapter 7, knowledge of Oshers solver is needed. The derivation of Osher's solver is based on the derivation that is given in Osher and Solomon [18] and Spekreijse [22].

6.1 Derivation of Osher's solver

The flux derivative of equation (2.18) can be written in the quasi-linear form

$$\frac{\partial \mathbf{f}}{\partial x} = \mathbf{A}\frac{\partial \mathbf{q}}{\partial x}, \tag{6.1}$$

with $\mathbf{A} = \frac{\partial \mathbf{f}(\mathbf{q})}{\partial \mathbf{q}}$, the Jacobian matrix. Diagonalizing the the Jacobian matrix results in

$$\mathbf{A} = \mathbf{R}\mathbf{\Lambda}\mathbf{R}^{-1}, \tag{6.2}$$

with $\mathbf{R} = [\mathbf{r}_1 \dots \mathbf{r}_k]$ a matrix containing all right eigenvectors and $\mathbf{\Lambda}$ a diagonal matrix containing the corresponding eigenvalues. We can split the diagonal matrix into matrices $\mathbf{\Lambda}^+$ and $\mathbf{\Lambda}^-$ containing respectively only the positive eigenvalues ($\lambda_k^+ = \max(0, \lambda_\mathrm{k})$) or

[1] Chapter 4 was added in the last period of this thesis work.

negative eigenvalues ($\lambda_k^- = \min(0, \lambda_k)$). We also introduce some matrix operations, which are useful during the derivation.

$$\mathbf{A}^+ = \mathbf{R}\mathbf{\Lambda}^+\mathbf{R}^{-1}, \tag{6.3a}$$

$$\mathbf{A}^- = \mathbf{R}\mathbf{\Lambda}^-\mathbf{R}^{-1}, \tag{6.3b}$$

$$|\mathbf{A}| = \mathbf{R}|\mathbf{\Lambda}|\mathbf{R}^{-1} = \mathbf{A}^+ - \mathbf{A}^-, \tag{6.3c}$$

$$\mathbf{A} = \mathbf{A}^+ + \mathbf{A}^-. \tag{6.3d}$$

Osher's approach assumes that there exist functions $\mathbf{f}^+(\mathbf{q})$ and $\mathbf{f}^-(\mathbf{q})$ such that

$$\mathbf{f}(\mathbf{q}) = \mathbf{f}^+(\mathbf{q}) + \mathbf{f}^-(\mathbf{q}), \tag{6.4}$$

and

$$\frac{\partial \mathbf{f}^+}{\partial \mathbf{q}} = \mathbf{A}^+, \quad \frac{\partial \mathbf{f}^-}{\partial \mathbf{q}} = \mathbf{A}^-. \tag{6.5}$$

With the initial data $\mathbf{q}_L$ and $\mathbf{q}_R$ of the Riemann problem, the numerical flux can be written as:

$$\mathbf{F}_{i+\frac{1}{2}}(\mathbf{q}_L, \mathbf{q}_R) = \mathbf{f}^+(\mathbf{q}_L) + \mathbf{f}^-(\mathbf{q}_R). \tag{6.6}$$

Using relations (6.3a) to (6.5), the numerical flux can also be written in three other forms, namely

$$\mathbf{F}_{i+\frac{1}{2}} = \mathbf{f}(\mathbf{q}_L) + \int_{\mathbf{q}_L}^{\mathbf{q}_R} \mathbf{A}^-(\mathbf{q})\mathrm{d}\mathbf{q}, \tag{6.7a}$$

$$\mathbf{F}_{i+\frac{1}{2}} = \mathbf{f}(\mathbf{q}_R) - \int_{\mathbf{q}_L}^{\mathbf{q}_R} \mathbf{A}^+(\mathbf{q})\mathrm{d}\mathbf{q}, \tag{6.7b}$$

$$\mathbf{F}_{i+\frac{1}{2}} = \frac{1}{2}\left[\mathbf{f}(\mathbf{q}_L) + \mathbf{f}(\mathbf{q}_R)\right] - \frac{1}{2}\int_{\mathbf{q}_L}^{\mathbf{q}_R} |\mathbf{A}(\mathbf{q})|\mathrm{d}\mathbf{q}. \tag{6.7c}$$

The first two representations reveal the upwind character of the Osher flux. Spekreijse [22] states that in general no functions $\mathbf{f}^+$ and $\mathbf{f}^-$ exist such that (6.4) is valid. This means that the integrals of equations (6.7a) to (6.7c) depend on their integration path. We continue with the numerical flux of equation (6.7a). Suppose that states $\mathbf{q}_L$ and $\mathbf{q}_R$ can be connected with each other by an integral path Γ, which is composed of subcurves Γ_k,

$$\Gamma = \bigcup_{k=1}^{n} \Gamma_k, \tag{6.8}$$

where Γ_k is tangential to the eigenvector $\mathbf{r}_k$. Γ_k can be parameterized by $\mathbf{q}(\xi)$ as

$$\frac{\mathrm{d}\mathbf{q}(\xi)}{\mathrm{d}\xi} = \mathbf{r}_k(\mathbf{q}(\xi)), \quad \text{for} \quad \xi_\mathrm{k} \le \xi \le \xi_{\mathrm{k}+1}, \quad \mathrm{k} = 1, \ldots, \mathrm{n}, \tag{6.9}$$

where ξ is an integration parameter which can be interpreted as $\xi = \frac{x}{t}$. There are two types of integral paths defined for the Osher solver, the O(sher)-variant and the P(hysical)-variant. The O-variant passes the subcurves in order of decreasing corresponding eigenvalues. This variant was originally proposed by Osher and Solomon [18] and is especially interesting when proving certain properties of the scheme. Later Hemker and Spekreijse [11] introduced the P-variant, which passes the subcurves in order of increasing corresponding eigenvalues to improve the efficiency. We therefore chose the

P-variant.
Each subcurve can be treated separately. Each subcurve represents a single wave. By performing a change of variables, using (6.9), we can rewrite the integral of equation (6.7a) to

$$\int_{\Gamma_k} \mathbf{A}^- \mathrm{d}\mathbf{q} = \int_{\xi_k}^{\xi_{k+1}} \mathbf{R}\mathbf{\Lambda}^-\mathbf{R}^{-1}\mathbf{r}_k \mathrm{d}\xi = \int_{\xi_k}^{\xi_{k+1}} \lambda_k^- \mathbf{r}_k \mathrm{d}\xi. \tag{6.10}$$

We need to know on which part of the subcurves Γ_k the corresponding eigenvalues $\lambda_k(\mathbf{q}(\xi))$ are negative. Some assumptions can be made about the eigenvalues $\lambda_k(\mathbf{q}(\xi))$, which are valid for most physical systems of equations, including ours. The eigenvalue $\lambda_k\left(\mathbf{q}(\xi)\right)$ is supposed to be either linearly degenerate, which means that along a subcurve Γ_k

$$\frac{\mathrm{d}}{\mathrm{d}\xi}\lambda_k\left(\mathbf{q}(\xi)\right) = \nabla\lambda_k \cdot \mathbf{r}_k = 0, \tag{6.11}$$

or genuinely non-linear, which means that along subcurve Γ_k

$$\frac{\mathrm{d}}{\mathrm{d}\xi}\lambda_k\left(\mathbf{q}(\xi)\right) = \nabla\lambda_k \cdot \mathbf{r}_k \neq 0. \tag{6.12}$$

The first indicate that $\lambda_k\left(\mathbf{q}(\xi)\right)$ is constant along Γ_k, representing a contact discontinuity. In the second case the eigenvalue $\lambda_k\left(\mathbf{q}(\xi)\right)$ is strictly monotone on Γ_k, representing a simple wave, in which $\lambda_k\left(\mathbf{q}(\xi)\right)$ changes sign at most once on Γ_k. Rewriting expression (6.10) results in

$$\int_{\xi_k}^{\xi_{k+1}} \lambda_k^- \mathbf{r}_k \mathrm{d}\xi = \int_{\xi_k^-}^{\xi_{k+1}^-} \lambda_k^- \mathbf{r}_k \mathrm{d}\xi = \int_{\xi_k^-}^{\xi_{k+1}^-} \lambda_k \mathbf{r}_k \mathrm{d}\xi = \int_{\xi_k^-}^{\xi_{k+1}^-} \mathbf{A}\mathbf{r}_k \mathrm{d}\xi = \int_{\mathbf{q}_k^-}^{\mathbf{q}_{k+1}^-} \frac{\mathrm{d}\mathbf{f}}{\mathrm{d}\mathbf{q}} \mathrm{d}\mathbf{q},$$

where $\xi_k^- = \min(0, \xi_\mathrm{k})$ and $\mathbf{q}_k^- = \mathbf{q}(\xi_k^-)$. So

$$\int_{\Gamma_k} \mathbf{A}^- \mathrm{d}\mathbf{q} = \mathbf{f}(\mathbf{q}_{k+1}^-) - \mathbf{f}(\mathbf{q}_k^-). \tag{6.13}$$

In the next sections we need to determine the number of integral paths Γ_k and how to calculate the state $\mathbf{q}_k$ on each intersection point of the integral paths Γ_k.

6.2 Characteristic equations & Riemann invariants

The Euler equations are *hyperbolic* PDEs. Hyperbolic PDEs describe physical phenomena in which one or more quantities propagate in preferred directions, while remaining of the same strength. These quantities are called *Riemann invariants* $\mathrm{d}\psi_k$ and the *characteristic equations* describe the transport of the Riemann invariants along a certain path. The Riemann invariants are transported with a velocity λ_k:

$$\frac{\partial\psi_k}{\partial t} + \lambda_k \frac{\partial\psi_k}{\partial x} = 0. \tag{6.14}$$

Because the characteristic equations are valid in the continuous domains only, we can use for the derivation of the characteristic equations the primitive equations, which were found in the chapter 3.

The Riemann invariants will be used for the determination of the fluxes. Here we derive the Riemann and characteristic equations for the flux in x-direction, so $\frac{\partial}{\partial y} = 0$. The set of primitive equations that were found in the previous chapter becomes:

$$\begin{aligned}
\frac{\partial \rho}{\partial t} + u\frac{\partial \rho}{\partial x} + \rho\frac{\partial u}{\partial x} &= 0,\\
\frac{\partial u}{\partial t} + u\frac{\partial u}{\partial x} + \frac{1}{\rho}\frac{\partial p}{\partial x} &= 0,\\
\frac{\partial v}{\partial t} + u\frac{\partial v}{\partial x} &= 0,\\
\frac{\partial p}{\partial t} + u\frac{\partial p}{\partial x} + \rho c^2\frac{\partial u}{\partial x} &= 0,\\
\frac{\partial \alpha}{\partial t} + u\frac{\partial \alpha}{\partial x} + \varphi\frac{\partial u}{\partial x} &= 0,\\
\frac{\partial \beta}{\partial t} + u\frac{\partial \beta}{\partial x} &= 0.
\end{aligned}$$

These equations can be written in the form:

$$\frac{\partial \mathbf{w}}{\partial t} + \mathbf{A}\frac{\partial \mathbf{w}}{\partial x} = 0, \tag{6.15}$$

with $\mathbf{w}$ the primitive vector:

$$\mathbf{w} = \begin{pmatrix} \rho \\ u \\ v \\ p \\ \alpha \\ \beta \end{pmatrix} \quad \text{and} \quad \mathbf{A} = \begin{bmatrix} u & \rho & 0 & 0 & 0 & 0 \\ 0 & u & 0 & \frac{1}{\rho} & 0 & 0 \\ 0 & 0 & u & 0 & 0 & 0 \\ 0 & \rho c^2 & 0 & u & 0 & 0 \\ 0 & \varphi & 0 & 0 & u & 0 \\ 0 & 0 & 0 & 0 & 0 & u \end{bmatrix}.$$

The eigenvalues can be determined by applying $\det(\mathbf{A} - \lambda_k \mathbf{I}) = 0$. The eigenvalues of the system of equations are:

$$\begin{aligned}
\lambda_1 &= u - c,\\
\lambda_{2,3,4,5} &= u,\\
\lambda_6 &= u + c.
\end{aligned} \tag{6.16}$$

This result shows that a flow element containing both fluids, has only one speed of sound. This is different from the two-phase flow model [3], which has two different speeds of sound for that single flow element.
Define the matrix $\mathbf{L}$ by choosing its rows to be the left eigenvectors $\mathbf{L}_k$, corresponding to the eigenvalues λ_k, $k = 1 \ldots 6$. The left eigenvectors are found using $\mathbf{L}_k\mathbf{A} = \lambda_k\mathbf{L}_k$. This results in:

$$\mathbf{L} = \begin{bmatrix} 0 & -\rho c & 0 & 1 & 0 & 0 \\ -c^2 & 0 & 0 & 1 & 0 & 0 \\ 0 & 0 & 1 & 0 & 0 & 0 \\ 0 & 0 & 0 & 0 & 1 & 0 \\ \varphi & 0 & 0 & 0 & 0 & -\rho \\ 0 & \rho c & 0 & 1 & 0 & 0 \end{bmatrix}.$$

Replace $\mathbf{A}$ by $\mathbf{L}^{-1}\mathbf{\Lambda}\mathbf{L}$, where $\mathbf{\Lambda} = \mathrm{diag}\,(\lambda_k)\,,\ k = 1\ldots 6$. Equation (6.15) can then be rewritten as

$$\mathbf{L}\frac{\partial \mathbf{w}}{\partial t} + \mathbf{\Lambda}\mathbf{L}\frac{\partial \mathbf{w}}{\partial x} = \mathbf{0}, \tag{6.17}$$

resulting in the characteristic equations:

$$\Big(\frac{\partial u}{\partial t} - \frac{1}{\rho c}\frac{\partial p}{\partial t}\Big) + (u-c)\Big(\frac{\partial u}{\partial x} - \frac{1}{\rho c}\frac{\partial p}{\partial x}\Big) = 0, \tag{6.18a}$$

$$\Big(\frac{\partial p}{\partial t} - c^2\frac{\partial \rho}{\partial t}\Big) + u\Big(\frac{\partial p}{\partial x} - c^2\frac{\partial \rho}{\partial x}\Big) = 0, \tag{6.18b}$$

$$\frac{\partial v}{\partial t} + u\frac{\partial v}{\partial x} = 0, \tag{6.18c}$$

$$\frac{\partial \beta}{\partial t} + u\frac{\partial \beta}{\partial x} = 0, \tag{6.18d}$$

$$\Big(\rho\frac{\partial \alpha}{\partial t} - \varphi\frac{\partial \rho}{\partial t}\Big) + u\Big(\rho\frac{\partial \alpha}{\partial x} - \varphi\frac{\partial \rho}{\partial x}\Big) = 0, \tag{6.18e}$$

$$\Big(\frac{\partial u}{\partial t} + \frac{1}{\rho c}\frac{\partial p}{\partial t}\Big) + (u+c)\Big(\frac{\partial u}{\partial x} + \frac{1}{\rho c}\frac{\partial p}{\partial x}\Big) = 0. \tag{6.18f}$$

So the Riemann invariants $\mathrm{d}\psi_k$ of the system of equations are:

$$\mathrm{d}\psi_1 = \mathrm{d}u - \frac{\mathrm{d}p}{\rho c} \qquad \text{along} \quad \lambda_1 = u - c, \tag{6.19a}$$

$$\mathrm{d}\psi_2 = \mathrm{d}p - c^2\mathrm{d}\rho \qquad \text{along} \quad \lambda_2 = u, \tag{6.19b}$$

$$\mathrm{d}\psi_3 = \mathrm{d}v \qquad \text{along} \quad \lambda_3 = u, \tag{6.19c}$$

$$\mathrm{d}\psi_4 = \mathrm{d}\beta \qquad \text{along} \quad \lambda_4 = u, \tag{6.19d}$$

$$\mathrm{d}\psi_5 = \rho\mathrm{d}\alpha - \varphi\mathrm{d}\rho \qquad \text{along} \quad \lambda_5 = u, \tag{6.19e}$$

$$\mathrm{d}\psi_6 = \mathrm{d}u + \frac{\mathrm{d}p}{\rho c} \qquad \text{along} \quad \lambda_6 = u + c. \tag{6.19f}$$

Four of the six Riemann invariants are equal to the single-fluid case. The other two Riemann invariants, equations (6.19d) and (6.19e), contain the fraction variables which are typical for this two-fluid model. It shows that the mass fraction is convected with the flow, while the volume fraction is not for a mixed fluid.

6.3 Implementation of Riemann invariants in Osher's solver

In the previous section we saw that the system of equations contains six eigenvalues of which three different kind of eigenvalues. This means that the integral path of equations (6.8) and (6.9) consists of six parts, in which Γ_2 to Γ_5 coincides with each other. This results into three different sub-curves, Γ_1, $\Gamma_{2\ldots5}$, Γ_6, which corresponds to the eigenvalues λ_1, $\lambda_{2\ldots5}$ and λ_6. A schematic representation of the complete integral path is given in figure 6.1.

Along integral paths Γ_1 and Γ_6, where $\lambda_1 = u - c$ and $\lambda_6 = u + c$, are v and β constant. On the other hand ρ, u, p and α are in general not constant, but a function of the location along the integral path, i.e. a function of the integration parameter ξ. The same holds for λ_1 and λ_6, which indicates that each of both integral paths represent a simple wave, as defined in equation (6.12).

Unlike the single-fluid Euler equations, see any textbook about gasdynamics, e.g. [4],

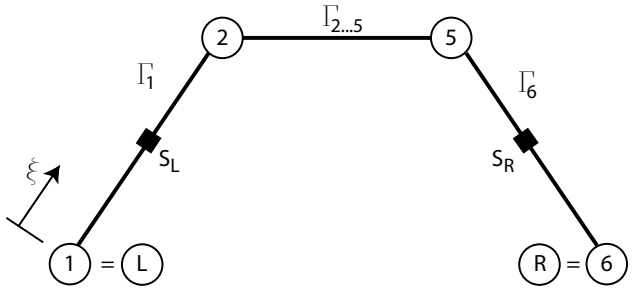

Figure 6.1: Integral path for Osher's flux, with the two initial states, $1 = L$ and $6 = R$, the two final states, 2 and 5, and the two sonic states, S_L and S_R.

it is not possible to express the state behind a simple wave in an analytic way as a function of the state in front of the simple wave. Instead, we get a set of differential equations which have to be solved. Along the integral paths Γ_1 and Γ_6 the Riemann invariants of equations (6.19b) to (6.19e) are equal to zero. For Γ_1 equation (6.19f) and for Γ_6 equation (6.19a) are also equal to zero. As independent variable for the set of differential equation the velocity component u is chosen. This results in:

$$\frac{\mathrm{d}p}{\mathrm{d}u} = \pm\rho c, \tag{6.20a}$$

$$\frac{\mathrm{d}\rho}{\mathrm{d}u} = \pm\frac{\rho}{c}, \tag{6.20b}$$

$$\frac{\mathrm{d}\alpha}{\mathrm{d}u} = \pm\frac{\varphi}{c}, \tag{6.20c}$$

$$v = \text{const}, \tag{6.20d}$$

$$\beta = \text{const}. \tag{6.20e}$$

where the '+' sign stands for a right running wave and the '−' sign for a left running wave. It is also possible to integrate along the particle path with the pressure p as independent variable. This gives the following set of differential equations:

$$\frac{\mathrm{d}u}{\mathrm{d}p} = \pm\frac{1}{\rho c}, \tag{6.21a}$$

$$\frac{\mathrm{d}\rho}{\mathrm{d}p} = \frac{1}{c^2}, \tag{6.21b}$$

$$\frac{\mathrm{d}\alpha}{\mathrm{d}p} = \frac{\varphi}{\rho c^2}, \tag{6.21c}$$

$$v = \text{const}, \tag{6.21d}$$

$$\beta = \text{const}. \tag{6.21e}$$

Unfortunately the final velocity and pressure are not known. Along integral path $\Gamma_{2\ldots5}$ the Riemann invariants of equations (6.19a) and (6.19f) are equal to zero. This is only possible if the velocity u and pressure p are constant along the integral path. A constant velocity u also means that $\lambda_{2\ldots5}$ are constant, implying that integral path $\Gamma_{2\ldots5}$ represents a contact discontinuity, as defined in equation (6.11). So integrating through the left wave and integrating through the right wave must end up with the same velocity and pressure.

We now have all the ingredients to find the two final states, $\mathbf{q}(\xi_2)$ and $\mathbf{q}(\xi_5)$, which are the states at the intersection points of the integral paths, and, if they exist, to find the states at the two sonic points of the simple waves, where $\lambda_1(\mathbf{q}(\xi)) = 0$ and $\lambda_6(\mathbf{q}(\xi)) = 0$. With these states, equation (6.13) and equation (6.7a) we can calculate the flux vector. Table 6.3 presents for each configuration how to calculate $\mathbf{F}_{i+\frac{1}{2}}$.
The numerical flux in y-direction can be determined in a similar fashion as is presented in this chapter for the x-direction.

	$\xi_1 \geq 0$, $\xi_6 \geq 0$	$\xi_1 \geq 0$, $\xi_6 \leq 0$	$\xi_1 \leq 0$, $\xi_6 \geq 0$	$\xi_1 \leq 0$, $\xi_6 \leq 0$
$\lambda_{2\ldots5} \geq 0$, $\xi_2 \geq 0$	$\mathbf{F}_1$	$\mathbf{F}_1 + \mathbf{F}_6 - \mathbf{F}_{S_R}$	$\mathbf{F}_{S_L}$	$\mathbf{F}_{S_L} - \mathbf{F}_{S_R} + \mathbf{F}_6$
$\lambda_{2\ldots5} \geq 0$, $\xi_2 \leq 0$	$\mathbf{F}_1 - \mathbf{F}_{S_L} + \mathbf{F}_2$	$\mathbf{F}_1 - \mathbf{F}_{S_L} + \mathbf{F}_2 - \mathbf{F}_{S_R} + \mathbf{F}_6$	$\mathbf{F}_2$	$\mathbf{F}_6 + \mathbf{F}_2 - \mathbf{F}_{S_R}$
$\lambda_{2\ldots5} \leq 0$, $\xi_5 \geq 0$	$\mathbf{F}_1 - \mathbf{F}_{S_L} + \mathbf{F}_5$	$\mathbf{F}_1 - \mathbf{F}_{S_L} + \mathbf{F}_5 - \mathbf{F}_{S_R} + \mathbf{F}_6$	$\mathbf{F}_5$	$\mathbf{F}_5 - \mathbf{F}_{S_R} + \mathbf{F}_6$
$\lambda_{2\ldots5} \leq 0$, $\xi_5 \leq 0$	$\mathbf{F}_1 - \mathbf{F}_{S_L} + \mathbf{F}_{S_R}$	$\mathbf{F}_1 - \mathbf{F}_{S_L} + \mathbf{F}_6$	$\mathbf{F}_{S_R}$	$\mathbf{F}_6$

Table 6.1: Osher's flux formulae

6.4 Boundary conditions

On the boundary of the computational domain boundary conditions must be applied. This is done by prescribing a number of state variables at the cell face to determine the flux over the boundary. The number of prescribed state variables depend on the direction of the wave speeds λ_k:

- *Supersonic outflow*: Since all characteristics run out of the computational domain, no state variable should be prescribed. The flux vector is completely prescribed by the state in the neighbouring cell.
- *Supersonic inflow*: Since all characteristics run into the computational domain, a complete state vector should be given at the boundary. Flow near the boundary has no influence on the flux at the boundary.
- *Subsonic outflow*: Only the λ_1 or λ_6, depending on the location of the boundary, runs into the computational domain. Therefore only one flow parameter has to be prescribed on the boundary. Most practical and most common is to prescribe either the velocity in normal direction to the boundary or the pressure at the outlet.
- *subsonic inflow*: In this case all except one of the outer characteristics runs into the computational domain. Therefore only one of the state variables should not be prescribed at the boundary.
- *Solid wall / symmetry plane*: This is a special case of the subsonic cases. In this case the velocity normal to the wall is zero. Since only one characteristic runs into the flow domain, only one state variable should be prescribed at the boundary, which then is the normal velocity equal to zero.

Chapter 7

Integration of the source term

In chapter 5 the finite-volume discretisation was given by equation (5.5). For the time derivative of the state vector a multi-stage scheme was introduced, the spatial discretization was done using a limited second-order scheme and the fluxes at the cell faces were found using Osher's approximate Riemann solver. In this section the integral of the source term will be treated.

Consider the integral over the source term of equation (5.5). We can substitute equation (3.34) for the source term S:

$$\int_{\Omega_{i,j}} S \mathrm{d}\Omega = \int_{\Omega_{i,j}} \left[-p\frac{\partial \alpha}{\partial t} + (\alpha - \beta)\, \mathbf{V} \cdot \nabla p \right] \mathrm{d}\Omega. \tag{7.1}$$

With $\frac{\partial \alpha}{\partial t}$ there is a second time-derivative introduced in equation (5.5). Fortunately this time-derivative can be replaced using the primitive equation of the volume fraction (3.29). This gives an integral containing only terms with spatial derivatives:

$$= \int_{\Omega_{i,j}} \left[p\mathbf{V} \cdot \nabla \alpha + p\varphi \nabla \cdot \mathbf{V} + (\alpha - \beta)\, \mathbf{V} \cdot \nabla p \right] \mathrm{d}\Omega. \tag{7.2}$$

7.1 Splitting the source term integral

Equation (7.2) contains only spatial derivatives. So for the disretization of the source term, we only have to focus on the spatial distibutions of the discretized state variables. We know these already from chapter 5, as illustrated in figure 7.1 for the 1D case. Therefore the single volume integral of equation (7.2) has, in discretized form, two different contributors to the source term integral:

- The distribution of the state variables over a cell is in general not constant, when applying data reconstruction to obtain higher order space discretization. This kind of state distribution contributes to the integral of the source term.
- The waves in the flux solver at each cell face that run into the cell also contribute to the integral of the source term.

Both are illustrated in figure 7.1 for the 1D case. For clarity reasons the derivation will be done one-dimensional, but it is easily extendible to more dimensions. In 1D, the volume integral reduces to a line integral. For a cell i, see figure 7.1a, it means that we

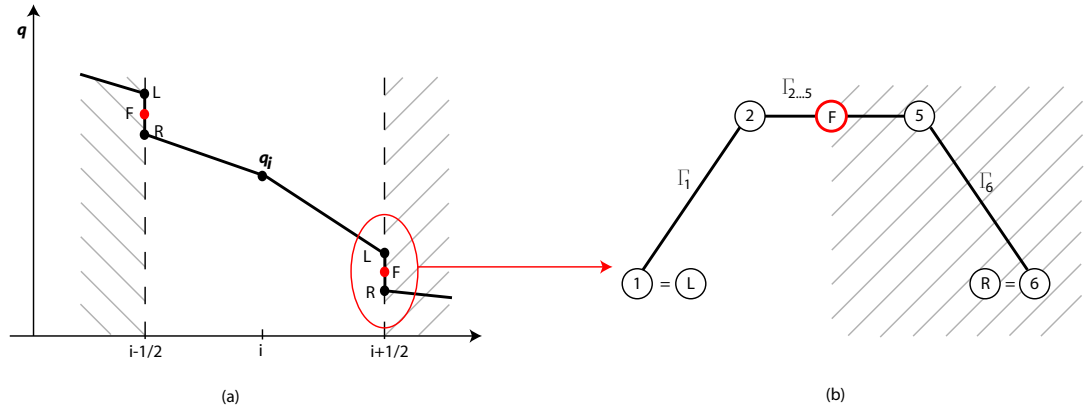

Figure 7.1: Source term in a cell: from distribution in the cell (a) and from cell faces (b)

need to integrate from the flux state $\mathbf{q}^F_{i-\frac{1}{2}}$ to flux state $\mathbf{q}^F_{i+\frac{1}{2}}$. To actually calculate this integral, we need to split it into three parts:

$$\int_{\Omega_i} S \, \mathrm{d}x = \int_{x^F_{i-\frac{1}{2}}}^{x^F_{i+\frac{1}{2}}} S \, \mathrm{d}x = \int_{x^F_{i-\frac{1}{2}}}^{x^R_{i-\frac{1}{2}}} S \, \mathrm{d}x + \int_{x^R_{i-\frac{1}{2}}}^{x^L_{i+\frac{1}{2}}} S \, \mathrm{d}x + \int_{x^L_{i+\frac{1}{2}}}^{x^F_{i+\frac{1}{2}}} S \, \mathrm{d}x, \tag{7.3}$$

in which the first integral is the integral through the left half of the flux solver for cell face $i - \frac{1}{2}$, the middle integral is the integral over the cell domain and last integral the integral through the right half of the flux solver for cell face $i + \frac{1}{2}$.
The 2D equivalent of equation (7.3) reads

$$\begin{aligned}\int_{\Omega_{i,j}} S \, \mathrm{d}\Omega = \int_{y^A_{i,j-\frac{1}{2}}}^{y^B_{i,j+\frac{1}{2}}} \int_{x^R_{i-\frac{1}{2},j}}^{x^L_{i+\frac{1}{2},j}} S \, \mathrm{d}x\mathrm{d}y + \Delta y \int_{x^F_{i-\frac{1}{2},j}}^{x^R_{i-\frac{1}{2},j}} S \, \mathrm{d}x + \Delta y \int_{x^L_{i+\frac{1}{2},j}}^{x^F_{i+\frac{1}{2},j}} S \, \mathrm{d}x + \\ \Delta x \int_{y^F_{i,j-\frac{1}{2}}}^{y^A_{i,j-\frac{1}{2}}} S \, \mathrm{d}y + \Delta x \int_{y^B_{i,j+\frac{1}{2}}}^{y^F_{i,j+\frac{1}{2}}} S \, \mathrm{d}y.\end{aligned} \tag{7.4}$$

7.2 Source in the cell domain

First let us concentrate on the middle integral of equation (7.3). When using a first-order finite-volume approximation the state values are constant in each cell. This means that all three spatial derivatives are zero, so the middle integral of equation (7.3) is equal to zero. However a higher-order spatial discretization is used, in which the state variables are no longer constant in a cell. The state variables in the cell are interpolated linearly from the cell center to the cell faces by the limited second-order approximation of section 5.3. This results in a piecewise linear distribution (see figure 7.1(a)), causing the spatial derivatives to be nonzero.

7.2.1 Derivation in 1D

The part of the integral of equation (7.2) that corresponds to a single piecewise linear distribution can be written in the following form:

$$\int_{x_i}^{x_j} \left[pu\frac{\partial \alpha}{\partial x} + p\varphi\frac{\partial u}{\partial x} + (\alpha-\beta)u\frac{\partial p}{\partial x}\right] \mathrm{d}x. \tag{7.5}$$

where x_i and x_j indicate the begin and endpoint of the single distribution. The integral of equation (7.5) can be split into three integrals with the same configuration:

$$\int_{x_i}^{x_j} ab\frac{\partial c}{\partial x}\,\mathrm{d}x,$$

in which a, b and c are linear functions given by:

$$a(x) = a_i + (a_j - a_i)\frac{x-x_i}{x_j-x_i},$$

and b and c having identical shapes. This integral can be obtained analytically and results in:

$$\int_{x_i}^{x_j} ab\frac{\partial c}{\partial x}\,\mathrm{d}x = \frac{1}{6}\big[2a_ib_i + a_ib_j + a_jb_i + 2a_jb_j\big](c_j - c_i). \tag{7.6}$$

The cell state in each cell consists of two piecewise linear distributions. Integrating the source term over the cell domain results in six integrals. The source integral over the cell domain becomes:

$$\begin{aligned}
&\int_{x^R_{i-\frac{1}{2}}}^{x^L_{i+\frac{1}{2}}} S\mathrm{d}x = \int_{x^R_{i-\frac{1}{2}}}^{x_i} S\mathrm{d}x + \int_{x_i}^{x^L_{i+\frac{1}{2}}} S\mathrm{d}x \\
&= \frac{1}{6}\left[2p^Ru^R + p^Ru_i + p_iu^R + 2p_iu_i\right](\alpha_i - \alpha^R) \\
&+ \frac{1}{6}\left[2p^R\varphi^R + p^R\varphi_i + p_i\varphi^R + 2p_i\varphi_i\right](u_i - u^R) \\
+\frac{1}{6}&\left[2\left(\alpha^R-\beta^R\right)u^R + \left(\alpha^R-\beta^R\right)u_i + (\alpha_i-\beta_i)\,u^R + 2\,(\alpha_i-\beta_i)\,u_i\right](p_i - p^R) \\
&+ \frac{1}{6}\left[2p_iu_i + p_iu^L + p^Lu_i + 2p^Lu^L\right](\alpha^L - \alpha_i) \\
&+ \frac{1}{6}\left[2p_i\varphi_i + p_i\varphi^L + p^L\varphi_i + 2p^L\varphi^L\right](u^L - u_i) \\
+\frac{1}{6}&\left[2\,(\alpha_i-\beta_i)\,u_i + (\alpha_i-\beta_i)\,u^L + \left(\alpha^L-\beta^L\right)u_i + 2\left(\alpha^L-\beta^L\right)u^L\right](p^L - p_i).
\end{aligned} \tag{7.7}$$

7.2.2 Derivation in 2D

In 2D, the data reconstruction of section 5.3 works in four directions. This results in four piecewise linear distributed planes, see figure 7.2. Like in the previous section we first calculate the contribution of a single plane. In 2D the integral over the source term is given by:

$$\begin{aligned}
&\int_{y_i}^{y_k}\int_{x_i}^{x_j} S\,\mathrm{d}x\mathrm{d}y = \int_{y_i}^{y_k}\int_{x_i}^{x_j} \big[p\mathbf{V}\cdot\nabla\alpha + p\varphi\nabla\cdot\mathbf{V} + (\alpha-\beta)\,\mathbf{V}\cdot p\big]\mathrm{d}x\mathrm{d}y \\
&= \int_{y_i}^{y_k}\int_{x_i}^{x_j} \big[pu\frac{\partial\alpha}{\partial x} + pv\frac{\partial\alpha}{\partial y} + p\varphi\frac{\partial u}{\partial x} + p\varphi\frac{\partial v}{\partial y} + (\alpha-\beta)\,u\frac{\partial p}{\partial x} + (\alpha-\beta)\,v\frac{\partial p}{\partial y}\big]\mathrm{d}x\mathrm{d}y.
\end{aligned} \tag{7.8}$$

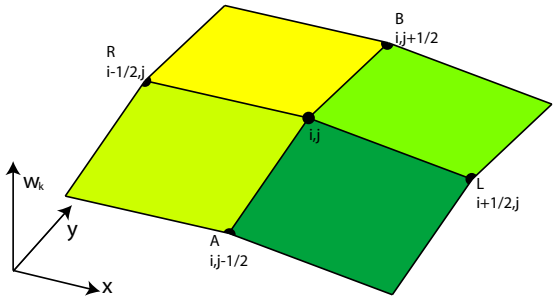

Figure 7.2: Schematic representation of a state distribution for a single cell $\Omega_{i,j}$, when applying second-order spatial discretization

The source in the cell domain for 1D calculations is given in subsection 7.2.1. For 2D calculations the same approach is used. Equation (7.8) is again integrated over the domain $\Omega_{i,j}$. The integral can be split into six integrals of the following configurations:

$$\int_{y_i}^{y_k}\int_{x_i}^{x_j} ab\frac{\partial c}{\partial x}\,\mathrm{d}x\mathrm{d}y, \qquad \int_{y_i}^{y_k}\int_{x_i}^{x_j} ab\frac{\partial c}{\partial y}\,\mathrm{d}x\mathrm{d}y,$$

in which a, b and c are linear functions given by:

$$a(x,y) = a_i + (a_j - a_i)\frac{x - x_i}{x_j - x_i} + (a_k - a_i)\frac{y - y_i}{y_k - y_i},$$

b and c have identical shapes. This results in

$$\int_{y_i}^{y_k}\int_{x_i}^{x_j} ab\frac{\partial c}{\partial x}\,\mathrm{d}x\mathrm{d}y = \tag{7.9}$$

$$= \frac{1}{12}\big[2a_ib_i - a_ib_j - a_ib_k - a_jb_i + 4a_jb_j + 3a_jb_k - a_kb_i + 3a_kb_j + 4a_kb_k\big](c_j - c_i)(y_k - y_i),$$

$$\int_{y_i}^{y_k}\int_{x_i}^{x_j} ab\frac{\partial c}{\partial y}\,\mathrm{d}x\mathrm{d}y = \tag{7.10}$$

$$= \frac{1}{12}\big[2a_ib_i - a_ib_j - a_ib_k - a_jb_i + 4a_jb_j + 3a_jb_k - a_kb_i + 3a_kb_j + 4a_kb_k\big](c_k - c_i)(x_j - x_i).$$

With equations (7.8), (7.9) and (7.10) an analytic expression of the source integral can be found for the each piecewise linear distribution. Adding up the four piecewise linear distributions results in the source integral over the domain for a single cell.

7.3 Source in the waves at the cell faces

To calculate the fluxes at the cell faces Riemann problems are solved. When taking an infinitely small time step, the waves of the Riemann problem travel into the cells. These waves also create a source. The Riemann problem acts in two cells, resulting in two source contributions for neighbouring cells, one from the left state $\mathbf{q}^L_{i+\frac{1}{2}}$ to the flux state $\mathbf{q}^F_{i+\frac{1}{2}}$ and for the neighbouring cell on from the flux state $\mathbf{q}^F_{i+\frac{1}{2}}$ to the right state $\mathbf{q}^R_{i+\frac{1}{2}}$. Futhermore the Riemann problem consists of three waves, a left and a right running isentropic wave and a contact discontinuity, each requiring special treatment, because

the isentropic waves are continuous phenomena and the contact discontinuity is not. The isentropic waves can run in both cells, even at the same time, so every isentropic wave, or part of it running into the same cell, must be treated separately. Fortunately the structure of the waves is already known from the calculation of the Osher fluxes, see chapter 6. Tables 7.1 and 7.2 show for all 16 wave combinations which integrals have to be taken for each cell[1].

	$\xi_1 \geq 0$, $\xi_6 \geq 0$	$\xi_1 \geq 0$, $\xi_6 \leq 0$	$\xi_1 \leq 0$, $\xi_6 \geq 0$	$\xi_1 \leq 0$, $\xi_6 \leq 0$
$\lambda_{2...5} \geq 0$, $\xi_2 \geq 0$	0	$\int_{S_R}^{6}$	$\int_{1}^{S_L}$	$\int_{1}^{S_L} + \int_{S_R}^{6}$
$\lambda_{2...5} \geq 0$, $\xi_2 \leq 0$	$\int_{S_L}^{2}$	$\int_{S_L}^{2} + \int_{S_R}^{6}$	$\int_{1}^{2}$	$\int_{1}^{2} + \int_{S_R}^{6}$
$\lambda_{2...5} \leq 0$, $\xi_5 \geq 0$	$\int_{S_L}^{2} + \int_{cd}$	$\int_{S_L}^{2} + \int_{cd} + \int_{S_R}^{6}$	$\int_{1}^{2} + \int_{cd}$	$\int_{1}^{2} + \int_{cd} + \int_{S_R}^{6}$
$\lambda_{2...5} \leq 0$, $\xi_5 \leq 0$	$\int_{S_L}^{2} + \int_{cd} + \int_{5}^{S_R}$	$\int_{S_L}^{2} + \int_{cd} + \int_{5}^{6}$	$\int_{1}^{2} + \int_{cd} + \int_{5}^{S_R}$	$\int_{1}^{2} + \int_{cd} + \int_{5}^{6}$

Table 7.1: Integration path for source in left half of the flux solver

	$\xi_1 \geq 0$, $\xi_6 \geq 0$	$\xi_1 \geq 0$, $\xi_6 \leq 0$	$\xi_1 \leq 0$, $\xi_6 \geq 0$	$\xi_1 \leq 0$, $\xi_6 \leq 0$
$\lambda_{2...5} \geq 0$, $\xi_2 \geq 0$	$\int_{1}^{2} + \int_{cd} + \int_{5}^{6}$	$\int_{1}^{2} + \int_{cd} + \int_{5}^{S_R}$	$\int_{S_L}^{2} + \int_{cd} + \int_{5}^{6}$	$\int_{S_L}^{2} + \int_{cd} + \int_{5}^{S_R}$
$\lambda_{2...5} \geq 0$, $\xi_2 \leq 0$	$\int_{1}^{S_L} + \int_{cd} + \int_{5}^{6}$	$\int_{1}^{S_L} + \int_{cd} + \int_{5}^{S_R}$	$\int_{cd} + \int_{5}^{6}$	$\int_{cd} + \int_{5}^{S_R}$
$\lambda_{2...5} \leq 0$, $\xi_5 \geq 0$	$\int_{1}^{S_L} + \int_{5}^{6}$	$\int_{1}^{S_L} + \int_{5}^{S_R}$	$\int_{5}^{6}$	$\int_{5}^{S_R}$
$\lambda_{2...5} \leq 0$, $\xi_5 \leq 0$	$\int_{1}^{S_L} + \int_{S_R}^{6}$	$\int_{1}^{S_L}$	$\int_{S_R}^{6}$	0

Table 7.2: Integration path for source in right half of the flux solver

7.3.1 Sources in the isentropic waves

We start with deriving the integrals over the isentropic waves. Equation (7.2) is integrated with respect to x. This is actually not possible because the flux solver does not have a finite length in x-direction. The waves 'travel' in the phase space of Osher's solver. We therefore change the integration parameter to ξ, the parameter for Osher's path. Unfortunately none of the state variables are known as function of ξ. Therefore another change in integration parameter is proposed. Instead of integration with respect to ξ, it is also possible to integrate with respect to the velocity, u. Since isentropic waves are continuous phenomena, the change in integration parameters can be done using the following relations:

$$\int_{x_i}^{x_j} S \mathrm{d}x = \int_{\xi_i}^{\xi_j} S \frac{\partial x}{\partial \xi} \mathrm{d}\xi = \int_{u_i}^{u_j} S \frac{\partial x}{\partial \xi} \frac{\partial \xi}{\partial u} \mathrm{d}u = \int_{u_i}^{u_j} S \frac{\partial x}{\partial u} \mathrm{d}u. \tag{7.11}$$

[1] $\int_{cd}$ Is the integral over the contact discontinuity. This is better than to write $\int_{2}^{3}$, since ξ_2 and ξ_3 can lie in different halfs of the plane.

Substitute into equation (7.11) the expression for S which was derived in equation (7.2),

$$\int_{x_i}^{x_j} S \mathrm{d}x = \int_{u_i}^{u_j} \left[pu \frac{\partial \alpha}{\partial u} + p\varphi + (\alpha - \beta)\, u \frac{\partial p}{\partial u} \right] \mathrm{d}u. \tag{7.12}$$

For the derivatives with respect to u, the differential equations that follow from the Riemann invariants (see equations (6.20)) can be substituted. This results in

$$= \int_{u_i}^{u_j} \left[p\varphi \left(1 \pm \frac{u}{c} \right) \pm (\alpha - \beta)\, \rho c u \right] \mathrm{d}u. \tag{7.13}$$

Note that integrating with respect to the velocity is an arbitrary choice, another possibility is to integrate the source term with respect to the pressure, p. This leads to

$$\int_{x_i}^{x_j} S \mathrm{d}x = \int_{p_i}^{p_j} \left[\frac{p\varphi}{\rho c} \left(\frac{u}{c} \pm 1 \right) + (\alpha - \beta)\, u \right] \mathrm{d}p.$$

7.3.2 Source due to contact discontinuity

The method used for the isentropic waves is not applicable for the contact discontinuity. The derivative $\frac{\partial \xi}{\partial u}$ in equation (7.11), used to change the integration parameter, does not exist everywhere along the integral path for the contact discontinuity, $\Gamma_{2\ldots5}$. Therefore another approach is used. We do have to transform the integration parameter to a parameter used in Osher's solver. This will again be the integral path parameter ξ, so

$$\int_{x_i}^{x_j} S \mathrm{d}x = \int_{\xi_i}^{\xi_j} S \frac{\partial x}{\partial \xi} \mathrm{d}\xi = \int_{\xi_i}^{\xi_j} \left[pu \frac{\partial \alpha}{\partial \xi} + p\varphi \frac{\partial u}{\partial \xi} + (\alpha - \beta)\, u \frac{\partial p}{\partial \xi} \right] \mathrm{d}\xi. \tag{7.14}$$

We know that the velocity and the pressure are constant over a contact discontinuity, so

$$\frac{\partial u}{\partial \xi} = 0, \tag{7.15a}$$

$$\frac{\partial p}{\partial \xi} = 0, \tag{7.15b}$$

both for $\xi \in \Gamma_{2\ldots5}$. This reduces equation (7.14) to

$$\int_{x_i}^{x_j} S \mathrm{d}x = \int_{\xi_i}^{\xi_j} pu \frac{\partial \alpha}{\partial \xi}\, \mathrm{d}\xi = up \int_{\xi_i}^{\xi_j} \frac{\partial \alpha}{\partial \xi}\, \mathrm{d}\xi. \tag{7.16}$$

It is not possible to apply the same trick to the integral as we did for equation (7.11), because $\frac{\partial \alpha}{\partial \xi}$ does not exist everywhere in the domain. To calculate the integral we first have to express α as a function of ξ. Between ξ_2 and ξ_5, the volume fraction has the shape of a heaviside function. The contact discontinuity can be integrated in the same way as was done in section 4.2. Then the contribution of the contact discontinuity at a cell face to the source in a cell is given by:

$$\int_{cd} S \mathrm{d}x = pu\, (\alpha_5 - \alpha_2)\,. \tag{7.17}$$

7.4 Applicability to shallow water flow over a non-flat bottom

The source term of the two-fluid model, discretized in this chapter, consists of terms in the form of $ab\frac{\partial c}{\partial x}$. The same form of source term is found in the momentum equation for shallow water flow over a non-flat bottom. The shallow water over a non-flat bottom model is given by

$$\frac{\partial h}{\partial t} + \nabla \cdot h\mathbf{V} = 0, \tag{7.18a}$$

$$\frac{\partial h\mathbf{V}}{\partial t} + \nabla \cdot h\mathbf{V}\otimes\mathbf{V} = -gh\nabla \cdot b. \tag{7.18b}$$

This model is discussed in Platzek [19]. The finite volume discretization used is comparable with the one presented in this report. The important difference is the treatment of the source term. To show that our method is also applicable to other models with the same kind of source term, it is applied to a "transcritical flow with a stationary shock" problem. Due to the bottom topography, given by

$$b(x) = \begin{cases} 0.2\left(\cos(10\pi(x-0.5)) + 1.0\right) & \text{if } |x-0.5| < 0.1 \\ 0 & \text{otherwise} \end{cases},$$

the flow becomes locally supercritical $\left(Fr = \frac{|\mathbf{V}|}{\sqrt{gh}} > 1\right)$. The initial conditions and numerical results are shown in figure 7.3. The numerical result shows good resemblance

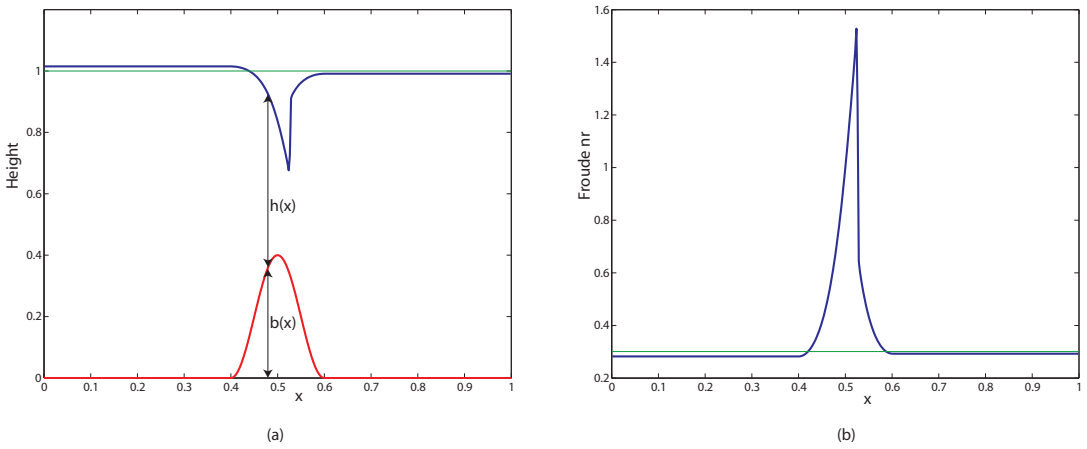

Figure 7.3: Bottom profile (red) and surface level (blue) (a) and Froude number (blue) (b) for a transcritical flow with a stationary shock together with the initial conditions (green).

with [19].

Chapter 8

Implementation of the flow solver

To perform numerical simulations for the two-fluid model, a `FORTRAN 90` code has been written by the author. The discretization of the two-fluid model that was presented in the previous three chapters has been coded into a computer program. Only the things that are not trivial and typical for the two-fluid model are discussed here. Section 8.1 explains how to switch between conservative state, primitive state and flux state. Section 8.2 briefly discusses the flux subroutine. The last section gives an overview of the set-up of the program.

8.1 Implementation issues

The discretization of the two-fluid model, presented in chapters 5 to 7, uses the state variables both in conservative form, $\mathbf{q}$, and in primitive form, $\mathbf{w}$. The relation between the conservative and primitive state variables are needed to be able to switch from the one to the other. For these relations the equations of state of both fluids must be specified. In this report two combinations of equations of state are used.
First, most test cases, both fluids are an *ideal gas*. A different ratio of specific heat γ_i makes the fluids different. The switch from primitive to conservative state variables is given by

$$q = \begin{pmatrix} \rho \\ \rho u \\ \rho v \\ \rho E \\ \alpha\rho_1 \\ \alpha\rho_1 E_1 \end{pmatrix} = \begin{pmatrix} w_1 \\ w_1 w_2 \\ w_1 w_3 \\ \left[\frac{w_6}{\gamma_1 - 1} + \frac{1-w_6}{\gamma_2 - 1}\right] w_4 + \frac{1}{2} w_1 \left(w_2^2 + w_3^2\right) \\ w_1 w_5 \\ \frac{w_4 w_6}{\gamma_1 - 1} + \frac{1}{2} w_1 w_5 \left(w_2^2 + w_3^2\right) \end{pmatrix}. \tag{8.1}$$

The switch from conservative to primitive state variables is given by

$$\mathbf{w} = \begin{pmatrix} \rho \\ u \\ v \\ p \\ \alpha \\ \beta \end{pmatrix} = \begin{pmatrix} q_1 \\ \frac{q_2}{q_1} \\ \frac{q_3}{q_1} \\ (\gamma_1-\gamma_2)\left[q_6 - \frac{q_5\left(q_2^2+q_3^2\right)}{2q_1^2}\right] + (\gamma_2-1)\left[q_4 - \frac{q_2^2+q_3^2}{2q_1}\right] \\ \frac{(\gamma_1-1)\left[q_6 - \frac{q_5\left(q_2^2+q_3^2\right)}{2q_1^2}\right]}{(\gamma_1-\gamma_2)\left[q_6 - \frac{q_5\left(q_2^2+q_3^2\right)}{2q_1^2}\right] + (\gamma_2-1)\left[q_4 - \frac{q_2^2+q_3^2}{2q_1}\right]} \\ \frac{q_5}{q_1} \end{pmatrix}. \tag{8.2}$$

The first three lines of equations (8.1) and (8.2) are equal to that of the single-fluid two-dimensional Euler equations. The pressure p and total energy ρE depend on the type of fluids and are different from that in the single-fluid case. The last two lines of equations (8.1) and (8.2) are specific for the two-fluid model.
Also the flux vector $\mathbf{F}$ can be written as a function of the primitive and conservative state variables. This is given by

$$\begin{aligned} F = \begin{pmatrix} \rho u \\ \rho u^2 + p \\ \rho u v \\ \rho u \left(E + \frac{p}{\rho}\right) \\ \alpha\rho_1 u \\ \alpha\rho_1 u \left(E_1 + \frac{p}{\rho_1}\right) \end{pmatrix} &= \begin{pmatrix} w_1 w_2 \\ w_1 w_2^2 + w_4 \\ w_1 w_2 w_3 \\ \left[\frac{w_6}{\gamma_1-1} + \frac{1-w_6}{\gamma_2-1} + 1\right] w_2 w_4 + \frac{1}{2} w_1 w_2 \left(w_2^2 + w_3^2\right) \\ w_1 w_2 w_5 \\ \frac{\gamma_1}{\gamma_1-1} w_2 w_4 w_6 + \frac{1}{2} w_1 w_2 w_5 \left(w_2^2 + w_3^2\right) \end{pmatrix} \\ &= \begin{pmatrix} q_2 \\ (\gamma_1-\gamma_2)\left[q_6 - \frac{q_5\left(q_2^2+q_3^2\right)}{2q_1^2}\right] + (\gamma_2-1)\left[q_4 - \frac{q_2^2+q_3^2}{2q_1}\right] + \frac{q_2^2}{q_1} \\ \frac{q_2 q_3}{q_1} \\ \frac{q_2}{q_1}\left\{q_4 + (\gamma_1-\gamma_2)\left[q_6 - \frac{q_5\left(q_2^2+q_3^2\right)}{2q_1^2}\right] + (\gamma_2-1)\left[q_4 - \frac{q_2^2+q_3^2}{2q_1}\right]\right\} \\ \frac{q_2 q_5}{q_1} \\ \frac{q_2}{q_1}\left\{q_6 + \left[q_6 - (\gamma_1-1)\frac{q_5\left(q_2^2+q_3^2\right)}{2q_1^2}\right]\right\} \end{pmatrix}. \end{aligned} \tag{8.3}$$

The fourth and sixth line of equation (8.1) and the fourth and fifth line of equation (8.2) change when changing the equations of state. The second combination of equations of state is a combination of *Van der Waals gas* and *stiffened gas*. The equations of state are given by

$$p(\rho, e) = (\gamma-1)\frac{\rho e + a\rho^2}{1-b\rho} - a\rho^2, \quad \text{with} \quad a \geq 0,\ 0 \leq b \leq \frac{1}{\rho}, \tag{8.4a}$$

$$p(\rho, e) = \rho e(\gamma-1) - \gamma\pi, \quad \text{with} \quad \pi \geq 0, \tag{8.4b}$$

in which a and b are parameters of the van der Waals equation of state and π a parameter of the stiffened equation of state. The switch from primitive state variables to

conservative state variables $(q_4, q_6)^T$ is given by

$$\begin{pmatrix} q_4 \\ q_6 \end{pmatrix} = \begin{pmatrix} \frac{w_6}{\gamma_1 - 1}\left[w_4 - bw_1 w_4 \frac{w_5}{w_6} + (2-\gamma_1) a w_1^2 \frac{w_5^2}{w_6^2} - abw_1^3 \frac{w_5^3}{w_6^3}\right] \\ \quad + \frac{1-w_6}{\gamma_2 - 1}\left[w_4 + \gamma_2 \pi\right] + \frac{1}{2} w_1 (w_2^2 + w_3^2) \\ \frac{w_6}{\gamma_1 - 1}\left[w_4 - bw_1 w_4 \frac{w_5}{w_6} + (2-\gamma_1) a w_1^2 \frac{w_5^2}{w_6^2} - abw_1^3 \frac{w_5^3}{w_6^3}\right] \\ \quad + \frac{1}{2} w_1 (w_2^2 + w_3^2) \end{pmatrix}. \tag{8.5}$$

The switch from conservative state variables to primitive state variables $(w_4, w_6)^T$ is more difficult. w_4 and w_6 can not be written as explicit functions of $\mathbf{q}$. Instead w_4 is a function of $\mathbf{q}$ and w_6 and w_6 is implicitly given as a fourth-order polynomial.

$$w_4 = \frac{Q_2}{1 - w_6} - \gamma_2 \pi, \tag{8.6a}$$

$$\begin{aligned} 0 = {} & \gamma_2 \pi w_6^4 + \left[Q_1 + Q_2 - \gamma_2 \pi (1 - b q_5)\right] w_6^3 \\ & + \left[-Q_1 - b q_5 (Q_2 - \gamma_2 \pi) - (2 - \gamma_1) a q_5^2\right] w_6^2 \\ & + \left[(2 - \gamma_1) a q_5^2 + abq_5^3\right] w_6 - abq_5^3, \end{aligned} \tag{8.6b}$$

with

$$\begin{aligned} Q_1 = {} & (\gamma_1 - 1)\left[q_6 - \frac{q_5 (q_2^2 + q_3^2)}{2 q_1^2}\right], \\ Q_2 = {} & -(\gamma_2 - 1)\left\{\left[q_6 - \frac{q_5 (q_2^2 + q_3^2)}{2 q_1^2}\right] - \left[q_4 - \frac{q_2^2 + q_3^2}{2 q_1}\right]\right\}. \end{aligned}$$

Again the flux vector $\mathbf{F}$ can be written as a function of the primitive state variables. This is given by

$$\mathbf{F} = \begin{pmatrix} \rho u \\ \rho u^2 + p \\ \rho u v \\ \rho u \left(E + \frac{p}{\rho}\right) \\ \\ \alpha \rho_1 u \\ \alpha \rho_1 u \left(E_1 + \frac{p}{\rho_1}\right) \\ \\ \end{pmatrix} = \begin{pmatrix} w_1 w_2 \\ w_1 w_2^2 + w_4 \\ w_1 w_2 w_3 \\ \frac{w_2 w_6}{\gamma_1 - 1}\left(w_4 + a w_1^2 \frac{w_5^2}{w_6^2}\right)\left(1 - b w_1 \frac{w_5}{w_6}\right) - a w_1^2 w_2 \frac{w_5^2}{w_6} \\ + \frac{w_2 (1 - w_6)}{\gamma_2 - 1}(w_4 + \gamma_2 \pi) + \frac{1}{2} w_1 w_2 (w_2^2 + w_3^2) + w_2 w_4 \\ w_1 w_2 w_5 \\ \frac{w_2 w_6}{\gamma_1 - 1}\left(w_4 + a w_1^2 \frac{w_5^2}{w_6^2}\right)\left(1 - b w_1 \frac{w_5}{w_6}\right) - a w_1^2 w_2 \frac{w_5^2}{w_6} \\ + \frac{1}{2} w_1 w_2 w_5 (w_2^2 + w_3^2) + w_2 w_4 w_6 \end{pmatrix}. \tag{8.7}$$

8.2 Flux subroutine

Flux calculation is time consuming. Especially for our two-fluid model. Several steps can be taken in advance to reduce computation time. A first step is to check if the left and right state are equal. In this case the flux can be determined immediately using equation (8.3) or (8.7). The second step is to check if we deal with an interface at rest. Then the flux vector becomes $\mathbf{F} = (0, p, 0, 0, 0, 0)^T$. A third check is if we locally deal with a single or two-fluid situation. This is the case when for the left and right state both the volume and mass fraction are zero or one. The single-fluid solver is easier and faster than the two-fluid solver, because for the single-fluid solver the initial and final

states are related by algebraic relations, while for the two-fluid solver the states have to be integrated through the isentropic waves to determine the final state.
Due to numerical diffusion and wave propagation states will change so that these three steps become less useful rather quickly. These steps are mainly useful for the beginning of two flow simulations.
The one-dimensional tests, treated in the next chapter, only use the two-fluid flow solver. The isentropic waves in Osher's solver are integrated using a fourth-order Runge-Kutta method and to find the final states the Secant method is used.

8.3 Algorithm

This section shows an overview of the numerical algorithm for the unsteady compressible two-flow model.

- Set initial condition $\mathbf{q}^0$ and $\mathbf{w}^0$.

`do while` $t < t_{final}$

- Determine Δt using the stability requirement.
- Start multistep time integration method. For every intermediate time step, $k = 1, \ldots, p$, the following steps are taken:
  - data reconstruction with slope limiter is applied to get boundary extrapolated values,
  - calculate fluxes at the boundary of the computational domain,
  - start subroutine which calculates the fluxes inside the computational domain. The flux algorithm is as follows:
    - `if` $\mathbf{w}^L = \mathbf{w}^R$, then the flux is $\mathbf{F}(\mathbf{w}^R)$,
    - `elseif` $p^L = p^R$ and $u^L = u^R = 0$, representing an interface at rest, the flux can be calculated directly,
    - `elseif` $\alpha^L = \alpha^R = \beta^L = \beta^R$ is either 0 or 1, then the flux is determined by the single-fluid Osher solver,
    - `else` the two-fluid Osher solver is used to calculate the fluxes.
    - The maximum wavespeed is stored to use later in the stability requirement.
  - Calculate the source term as follows:
    - the wave pattern from the flux subroutine is known and is again used to determine the source term in the flux solver,
    - calculate the source term integral inside the cell.
  - Calculate the right-hand-side of equation (5.14), $\mathbf{L}(\mathbf{q}^{(m)})$,
  - and march to new intermediate ERK stage.
- Update the conservative state vector to $\mathbf{q}^{n+1}$ and transform it to the primitive state vector $\mathbf{w}^{n+1}$,
- write vector $\mathbf{w}^{n+1}$ to file.

`end do`

Part III

Flow Problems & Numerical Results

Chapter 9

One-Dimensional Problems

In this chapter one-dimensional flow problems, applied to the two-fluid model, are discussed. In real life however flows are never one-dimensional and, as seen in chapter 3, the model is at most quasi one-dimensional. Nevertheless, in gas dynamics one-dimensional problems are ideal as a mathematical tool for testing and validating the flow model and numerical scheme, because for certain one-dimensional problems the exact solution is known. Common used one-dimensional problems are the so called *shock tube problems*. In these problems the shock tube is divided into two parts, separated by a membrane, see figure 9.1. Both parts have constant flow properties. At $t = 0$ the membrane is removed and the fluids start moving. The interface, which for one-dimensional problems acts as a contact discontinuity, moves with a velocity u. Two more waves appear in the solution, each running into one of the fluids with velocities $u \pm c$. They can be either a shock wave or an expansion fan. A set of test problems will be treated, each containing its own

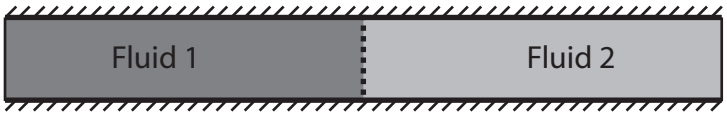

Figure 9.1: A shock tube with two fluids separated by an interface for $t = 0$

difficulties. Every test problem will be discussed both qualitatively and quantitatively. The latter is done with a grid refinement study. On several grids, ranging from 50 to 1600 cells, the errors in the state variable distributions are calculated. For this purpose the L_1-error norm is used, such that the average error per state variable distribution can be written as

$$\epsilon_{L_1} = \frac{1}{N} \sum_{i=1}^{N} \left| q^k(x_i) - q_i^k \right|. \tag{9.1}$$

The order of accuracy n, i.e. $\mathcal{O}(\Delta x^n)$, is obtained from these errors and their corresponding grid size using a least-squares method. All simulations are performed with the third-order explicit Runge-Kutta scheme to march in time and the Koren limiter is used for the boundary extrapolated states. To ensure stability the Courant number is equal to 0.25 for all problems, unless otherwise stated. A fixed grid and fixed Courant number results in a variable time step. Furthermore, unless otherwise stated, the equations of state used for the simulations are those for ideal gases. A different ratio of specific heats γ_i ensures that we deal with a two-fluid problem.
In this chapter the following tests are performed: first a translating interface problem, secondly a high pressure high density Sod problem, then a no reflection problem. These

three test cases were also considered by Naber [16] and Wackers [29]. Naber [17] only did the first and third tests. The last test is a Van der Waals gas - stiffened gas problem of Shyue [21].

9.1 Translating interface

This first test focus on the behavior of a moving two-fluid interface. The two fluids have a density ratio like water and air. A big density ratio will clearly show the performance of this test. The ratios of specific heats differ, making the problem two-fluid. The velocity and pressure of both fluids are the same, resulting only in a translating interface. The initial conditions are given in table 9.1. The interface moves to the right with velocity u.

	ρ	u	p	α	β	γ
fluid 1	1000.0	1.0	1.0	1.0	1.0	1.4
fluid 2	1.0	1.0	1.0	0.0	0.0	1.6

Table 9.1: Initial values for the translating interface problem.

From the exact solution we expect at the location of the interface only a sharp change in density and the volume and mass fractions. We expect the velocity and pressure to be constant along the shock tube.
The solution is shown in figure 9.2. The density plot 9.2(a) shows that the interface is at the correct location. The numerical interface is smeared over about 8 cells. More important is that the velocity and pressure remain constant over the interface. No pressure oscillations are present. This means that our model does not need any fixes, in contrast to other methods, like the level-set method of Naber [17] and the incomplete model of Quirk and Karni [20]. In the mass fraction plot 9.2(d), it looks like the interface is not at the correct location. This is due to the high density ratio, then for most cells containing both fluids, $\beta \approx 1$. So while the interface is smeared over about 8 cells, only a couple of them are visible.
Table 9.2 shows the errors and order of convergence for all variables. The velocity and pressure are exact for all grid sizes. Although a third-order time and a second-order space discretization is used, the contact discontinuity with a high density ratio reduces the order of the other variables to about 0.75.

N	e_ρ	e_u	e_p	e_α	e_β
50	11.421	0.0000	0.0000	0.0114	0.0460
100	6.7420	0.0000	0.0000	0.0067	0.0276
200	3.9723	0.0000	0.0000	0.0040	0.0165
400	2.3408	0.0000	0.0000	0.0023	0.0098
800	1.3918	0.0000	0.0000	0.0014	0.0059
Order	0.7586	-	-	0.7586	0.7398

Table 9.2: Errors and order of convergence for the interface translation problem for the five state variables.

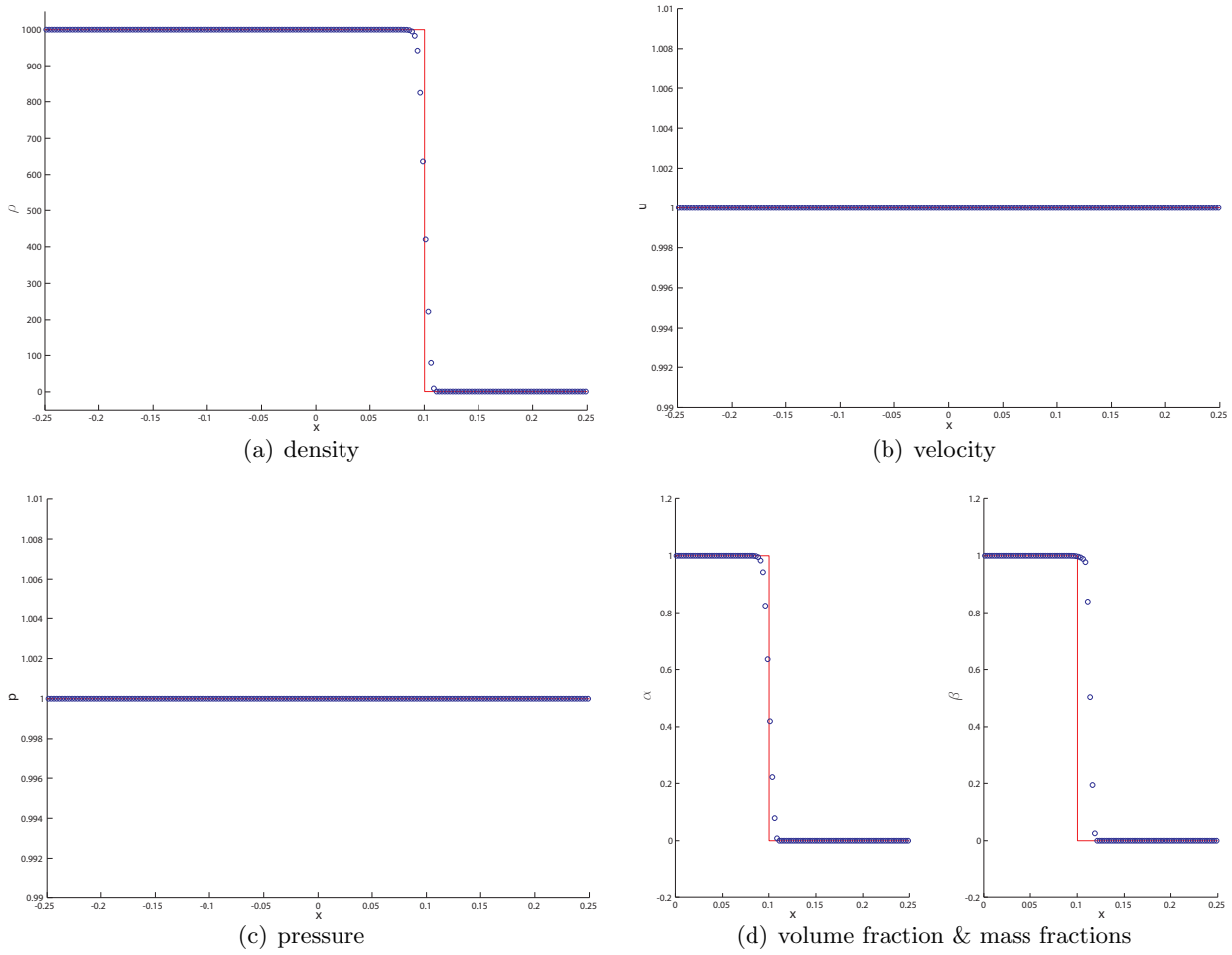

(a) density (b) velocity

(c) pressure (d) volume fraction & mass fractions

Figure 9.2: Numerical "○" and exact "—" state distribution of the translating interface problem at $t = 0.10$, for 200 cells and $C = 0.25$.

9.2 High pressure high density Sod problem

The second test case is a variant of the well-known Sod problem. The test presented here consists of two fluids and a high pressure and high density jump over the interface. This test is often used because it contains all three kinds of waves. The initial conditions are given in table 9.3. Initially both fluids are at rest, but due to the pressure difference,

	ρ	u	p	α	β	γ
fluid 1	10.0	0.0	10.0	1.0	1.0	1.4
fluid 2	0.125	0.0	0.1	0.0	0.0	1.6

Table 9.3: Initial values for the high pressure high density Sod problem.

the contact discontinuity (representing the interface) starts moving to the right, an expansion wave travels into the left fluid and a shock wave runs into the right fluid.
In figures 9.3 we see that all waves are captured at the correct location. Figures 9.3(a) and 9.3(c) show that the expansion wave is captured almost exactly. The shock, best visible in figure 9.3(b), is captured in 3 cells. From the density plot and the two fraction plots we see that the interface is captured in about 8 cells. The difference between capturing a shock and a contact discontinuity is that for a shock the information travels towards the shock, while for a contact discontinuity the information travels parallel with the wave. Again there are no pressure oscillations visible. Finally, a small overshoot is visible at the tail of the expansion fan. This overshoot is probably caused by the finite volume method and not by the two-fluid model, because it was also noticed for single-fluid flows. Moreover it reduces in size on grid refinement.
Table 9.4 shows the errors and order of convergence for this test case. The velocity and pressure converge with order 1.0, due to the presence of the shock. This was expected, because near discontinuities the limiter locally turns the scheme to first-order accurate. The contact discontinuity reduces the order of convergence of the density and the fractions to less than 1.0. The values in table 9.4 are comparable to those in [29].

N	e_ρ	e_u	e_p	e_α	e_β
50	0.0681	0.0294	0.0581	0.0160	0.0207
100	0.0348	0.0113	0.0285	0.0080	0.0113
200	0.0189	0.0057	0.0143	0.0055	0.0083
400	0.0098	0.0028	0.0072	0.0029	0.0049
800	0.0051	0.0014	0.0036	0.0016	0.0030
Order	0.9368	1.0416	1.0074	0.8507	0.6946

Table 9.4: Errors and order of convergence for the high pressure high density Sod problem for the five state variables.

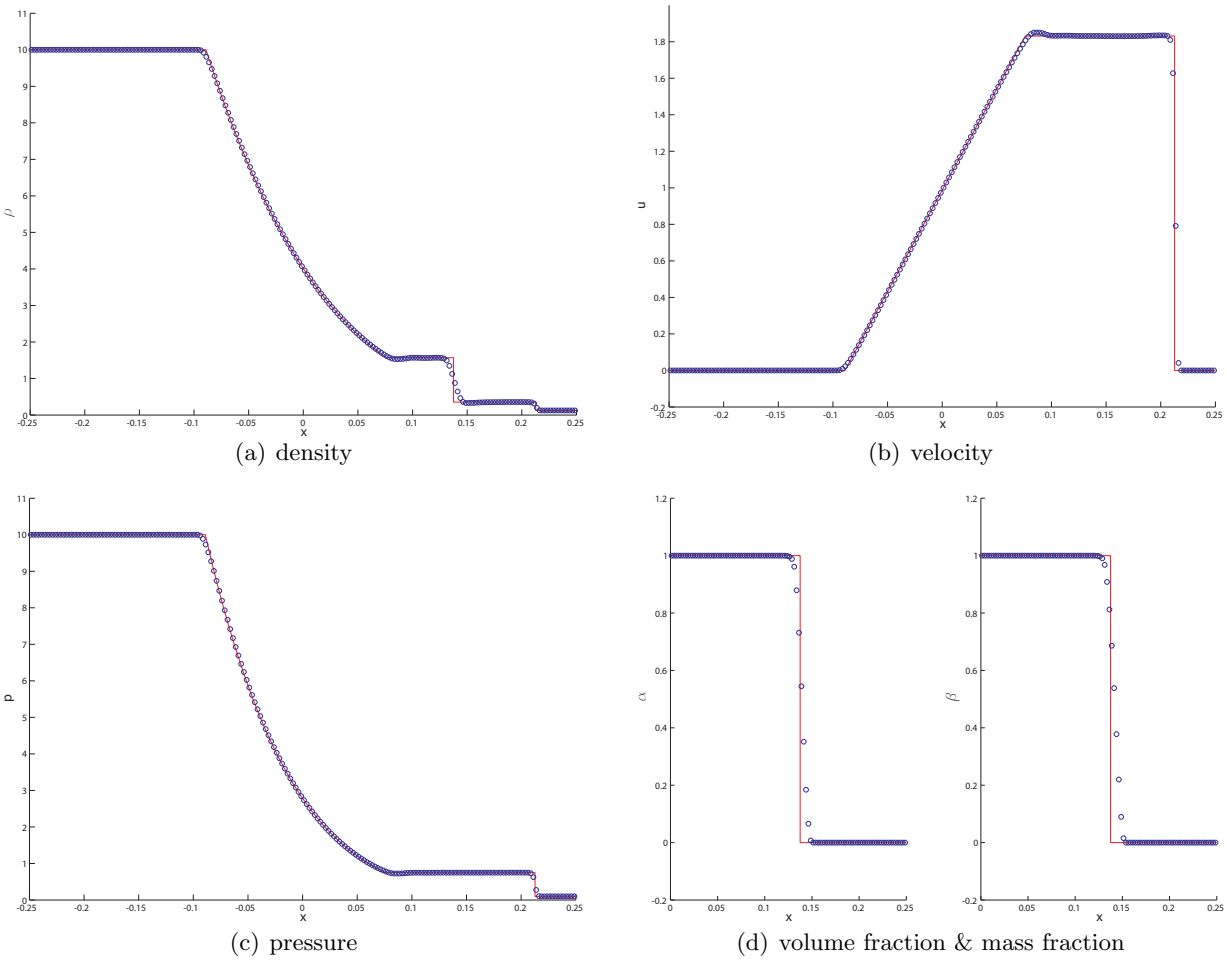

(a) density (b) velocity

(c) pressure (d) volume fraction & mass fraction

Figure 9.3: Numerical "○" and exact "—" state distribution of the high pressure high density Sod problem at $t = 0.075$, for 200 cells and $C = 0.25$.

9.3 No-reflection problem

The third problem is the no-reflection problem. This test case treats an initial two-fluid interface at rest that is hit by a strong shock coming from the left. The pressure ratio over the shock is set at 1 to 100, making it the hardest test treated in this chapter. From the moment they collide, this is where the simulation starts, the shock continues travelling to the right, followed by the interface, which now also moves to the right. The initial density and velocity jumps are chosen such that no reflection wave is created, which means that the left running wave is of zero strength. The initial conditions are given in the table below.

	ρ	u	p	α	β	γ
fluid 1	3.1748	9.4350	100.0	1.0	1.0	1.667
fluid 2	1.0	0.0	1.0	0.0	0.0	1.2

Table 9.5: Initial values for the no-reflection problem.

In figure 9.5 the results are plotted in the case of 400 cells and for $t = 0.02$. Although this problem is called the no-reflection problem the numerical results show a bump at the location of the left-running wave (which moves to the right because the flow is supersonic). This bump is an error introduced by the solver and will reduce in size on grid refinement. The same bump is visible in the numerical results in [16, 17, 29]. Note that this bump has no effect on the volume and mass fraction.
Table 9.6 shows the errors and orders of convergence for the no-reflection problem. Again the order of convergence is limited by the discontinuities. As mentioned earlier we see the effect of the contact discontinuity in the orders of convergence. Comparing the errors and orders with the finite-volume level-set method of [16] and the capturing method of [29] we see that the errors are of the same magnitude, but the orders presented in table 9.6 are higher than those in [16] and [29]. As expected the errors are higher than those for the discontinuous Galerkin level-set method of [17]. However the orders of convergence are about the same.

N	e_ρ	e_u	e_p	e_α	e_β
100	0.2400	0.1469	1.4134	0.0187	0.0064
200	0.1348	0.0934	0.9206	0.0083	0.0039
400	0.0676	0.0454	0.4501	0.0043	0.0021
800	0.0359	0.0210	0.2070	0.0026	0.0011
1600	0.0192	0.0102	0.1033	0.0012	0.0006
Order	0.8964	0.9911	0.9871	0.9799	0.8429

Table 9.6: Errors and order of convergence for the no-reflection problem for the five state variables

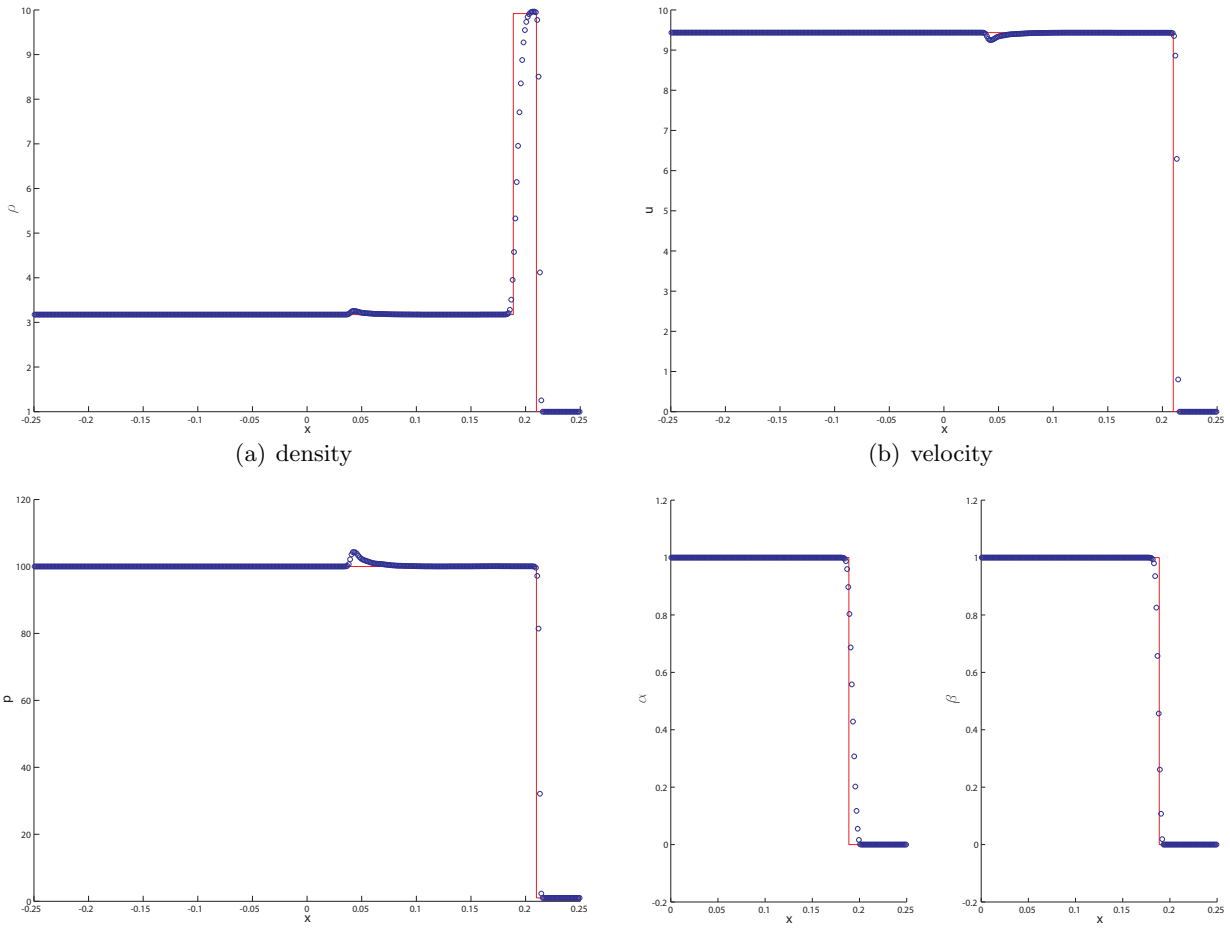

(a) density (b) velocity

(c) pressure (d) volume fraction & mass fraction

Figure 9.4: Numerical "○" and exact "—" state distribution of the no reflection problem at $t = 0.02$, for 400 cells and $C = 0.25$.

9.4 Real gases

Equations (2.12) give the equations of state in their most general form. The previous three sections used only ideal gases, but also other equations of state can be used. In this section Van der Waals equation of state, equation (8.4a), and the equation of state for stiffened gas, equation (8.4b), is used. This makes the test more difficult. For ideal gases the numerical mixture again results in an ideal gas, while for the real gases problem the numerical mixture consists of a new type of gas.
The gases are applied to a translating interface problem. The initial conditions are given in table 9.7. The gas parameters a, b and π are kept small, because for higher values of the parameters the flux solver had problems to converge. Therefore also the Minmod limiter was used.
Nevertheless the current problems show that is indeed possible to insert different types

	ρ	u	p	α	β	γ	a	b	π
fluid 1	1.0	1.0	1.0	1.0	1.0	1.4	0.01	0.01	0.0
fluid 2	0.5	1.0	1.0	0.0	0.0	1.6	0.0	0.0	0.2

Table 9.7: Initial values for the real gases problem.

of equations of state in the flow model. The numerical results are shown in figure 9.5. Also for the real gases problem the numerical results of the velocity and pressure are oscillation free. Due to a different limiter, more cells are needed to capture the interface.

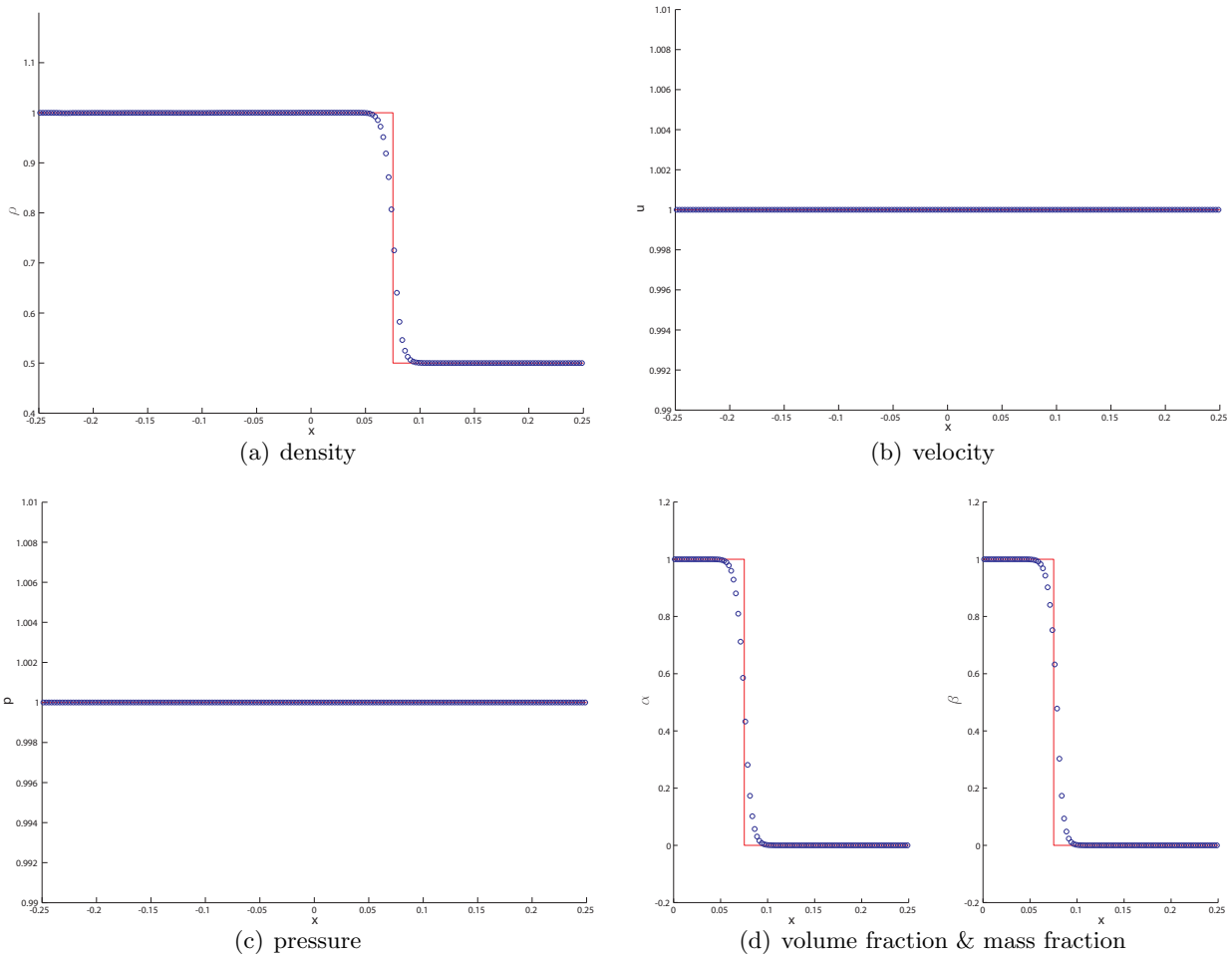

(a) density (b) velocity

(c) pressure (d) volume fraction & mass fraction

Figure 9.5: Numerical "○" and exact "—" state distribution of the real gases problem at $t = 0.075$, for 200 cells and $C = 0.25$.

Chapter 10

Shock-bubble interaction

Shock-bubble interaction is a well-known test which was first reported by Haas and Sturtevant [9]. They performed several experiments on the interaction between a shock moving in air and a bubble containing a different gas. One of the motivations for studying shock-bubble interactions is to investigate mechanisms in which air and fuel can be mixed efficiently in the short transit times available with supersonic combustion systems. By now this problem has become a benchmark, which was treated numerically among others by Quirk and Karni [20], by Wackers and Koren [29] and by Naber [16, 17]. Haas and Sturtevant did experiments with spherical and cylindrical bubbles. The latter are of interest here since we do two-dimensional simulations. These cylindrical bubbles will be filled with either a gas which is lighter or heavier than air. The problem starts with a bubble at rest, which is separated from the surrounding air by a micro-film. From the right a shock travels toward the interface. The initial situation is given in figure 10.1. When the shock hits the bubble, the micro-film will tear apart and interacts with

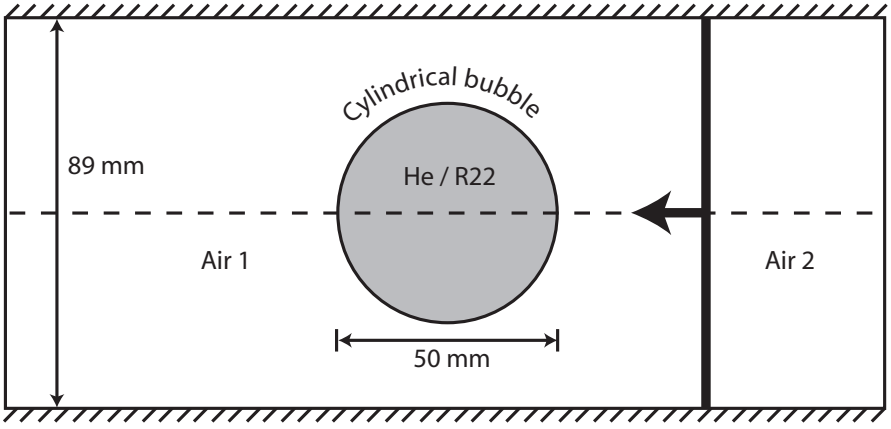

Figure 10.1: Initial situation of the shock-bubble interaction problem, located inside a wind tunnel

the bubble. Due to the high velocity of the shock wave (it passes the bubble in about 10^{-4} seconds for a speed of sound of 343 m/s) the two fluids do not mix during this experiment. Therefore our model is well-suited to perform this benchmark case.
The deformation of the interface and the wave pattern strongly depend on the kind of gas used for the bubble. Haas and Sturtevant [9] used helium and R22 for their experiments. The former has a higher speed of sound than air and the latter has a lower speed of sound than air. Although both result in very different wave patterns, they have some

types of waves in common. The shock traveling toward and later passing the bubble is called the *incoming shock*. This shock initially travels with a Mach number of 1.22. After hitting the interface, part of the incoming shock continues inside the bubble as a *refraction wave*. The other part travels back into the air as a *reflection wave*. Interaction between the incoming shock and the bubble interface causes the interface to move to the left. This process will occur again when the refracted wave reaches the interface on the other side of the bubble. Then part of the wave continues into the air as a *transmitted wave* and part of it is reflected as a second reflection wave. More details of the wave patterns are given in the next two sections.
For computational efficiency the numerical domain is halved by making use of the symmetric shape of the flow domain. The dimensions of the computational domain are $0.16 \times 0.0445\ m$ and are divided in 800×200 equally sized cells. The cell size is equal to that in [17, 29], to make a proper comparison with their numerical simulations.
The initial conditions of the different states and gases are given in table 10.1. All values are normalized for a speed of sound of 343 m/s. Notice that for helium the ratio of specific heats is lower and that the density is higher than is expected, 1.648 instead of 1.667 and 0.25463 instead of 0.19317. This is due to some contamination of the helium cylinder by air, that had leaked through the micro-film. Haas and Sturtevant [9] estimated the contamination at 28% by air mass.

	γ	ρ	u	v	p	α	β
air 1	1.400	1.40000	0.00000	0.00000	1.00000	1.0	1.0
air 2	1.400	1.92691	0.33361	0.00000	1.56980	1.0	1.0
helium	1.648	0.25463	0.00000	0.00000	1.00000	0.0	0.0
R22	1.249	4.41540	0.00000	0.00000	1.00000	0.0	0.0

Table 10.1: Initial conditions and gas properties for the shock-bubble interaction problems.

10.1 R22 bubble

In the first test case the bubble is filled with refrigerant R22. This gas is a HCFC which is used in air conditioners and heat pumps. HCFCs, like R22, became popular as a replacement of the ozone-depleting CFC's. However they found out that HCFC's are also ozone-depleting and thus are scheduled for phaseout. R22 has a higher density and lower ratio of specific heats than air, resulting in a normalized speed of sound of 0.532. A lower speed of sound causes the refraction shock to lag behind of the incoming shock. Together with the circular shape of the bubble, the refraction shock becomes curved. Also the reflected wave has a curved shape and is travelling away from the bubble through the air. A schematic drawing of the waves and interface deformation is given in figure 10.2.
The same can be seen in the experimental and numerical results of figure 10.4(a). An important remark has to be made about the color bar. This color bar is made such that most of the waves and physics is visible. This clarifies why there is a big difference in density between green and yellow. Figure 10.4(b) shows that the incoming shock and its refracted shock inside the bubble remain connected. Therefore also the incoming shock becomes curved. Figures 10.4(c) and 10.4(d) show that the reflected shock is bounced back from the wall and hits the interface at the top. This shock however is too weak to

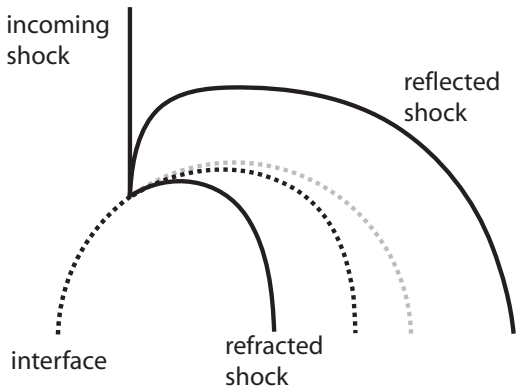

Figure 10.2: Wave pattern as a result of the interaction between the shock and the R22 bubble.

have significant effect on the interface movement and its refracted and reflected waves are too weak to be visible.
The refracted shock becomes so curved that pressure waves appear at the locations of the sharp bends, as can be seen in figure 10.4(c) (circled). At these locations the density and pressure rapidly increase, see the black spots in figure 10.4(d). The pressure waves finally meet, resulting in a density peak of more than three times the initial density and a pressure peak of four and a half times the initial pressure of the bubble. Behind the bubble the two parts of the incoming shock, that were split in front of the bubble, cross each other. They remain attached to the air-bubble interface. The refracted shock to which they are connected become weak and are hardly visible. The refracted shock focuses near the downstream interface. It then expands radially as a transmitted shock, as can be seen in figure 10.5(e), indicated by the arrow. A high velocity created by the transmitted shock at its focus causes a central wedge to form on the interface. As the transmitted shock travels along the interface, two inward curling vortices are generated. This starts already in figure 10.5(f), but is better visible in figure 10.5(g). However, in the experimental results this pair of vortices is not yet visible. Only figure 10.5(i), at $t = 1020\mu s$, shows the vortices.
Figure 10.6 shows the pressure plots for four different time-levels. The location of the interface is not visible in these plots, as it should be, because the pressure is continuous over the interface. A guess of the interface location may still be made though, because the pressure gradients away from the interface for both fluids are different.
Figure 10.7 shows the volume fraction. The white line shows the initial location of the bubble. The interface, where the volume fraction is between 0.0 and 1.0, is initially a single cell thick. When the incoming shock has passed the interface, it is smeared over a few cells. At the time of figure 10.7(b), the shock almost completely passed the bubble. Still the interface is at the correct location, and has not been torn apart, as in the numerical results in [29]. A comparison is made in figure 10.3, which shows the difference in volume fraction between the current numerical results and that in [29]. For this purpose the same plot style is used. The S_E part of the source term, which was not taken into account in the results in [29] caused the interface to break up in two pieces. Figure 10.7(c) shows a locally thicker interface at the top and bottom of the bubble. This is caused by a roll-up of the interface. This is the start of a vortex. In

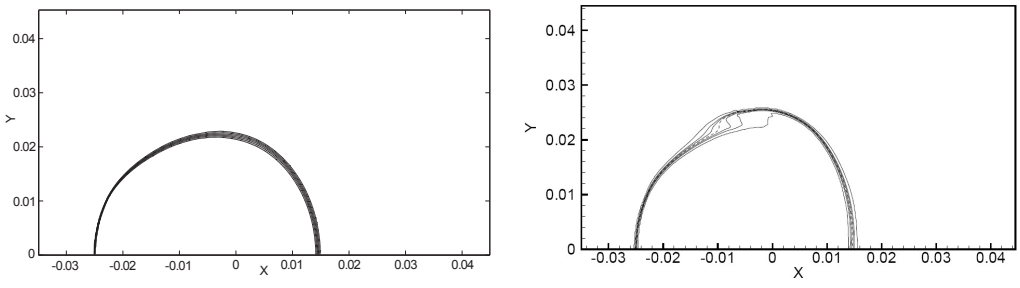

Figure 10.3: Comparison of the volume fraction, left: current numerical results, right: numerical results of Wackers [29].

figure 10.7(d) the two vortices are clearly visible. The locally thicker interface right of the vortices are likely caused by Kelvin-Helmholtz instability. These swellings are also found and described in [20]. In [17] the roll-up of the interface due to Kelvin-Helmholtz instability for inviscid fluids is described in more detail.
In the numerical results of figures 10.5(f) to 10.5(h) a 'nose' is visible on the downstream interface. Although to a less extent, the 'nose' can also be seen in the experimental results. The larger 'nose' in the numerical results may be caused by the numerical boundary conditions. Equations (5.11a) and (5.12b) are given such that the spacial discretization locally reduces to first-order accurate.
Besides a qualitative survey, some quantative comparison of the waves can be made. We discuss the velocity of the incoming shock, c_s, the velocity of the refraction shock, c_r, and the velocity of the interface, c_i. The velocities are compared with the experiments in [9] and the numerical computations in [17, 20, 29]. All velocities are given in table 10.2. The dimensionless velocities that result from the computations are multiplied by the initial speed of sound of air, i.e. 343 m/s. The velocities are obtained by interpolation of several locations and the corresponding times. Table 10.2 shows that the present method

	c_s $[m/s]$	c_r $[m/s]$	c_i $[m/s]$
Present method	419	241	75
Haas & Sturtevant [9]	415	240	73
Quirk & Karni [20]	420	254	70
Wackers & Koren [29]	419	241	75
Naber [17]	419	230	73

Table 10.2: Comparison of wave speeds between several numerical results, including ours, and the experimental results, for the R22 bubble test.

performs almost simular to the experiments and the other numerical simulations. The current wave speeds are even equal to those in [29].

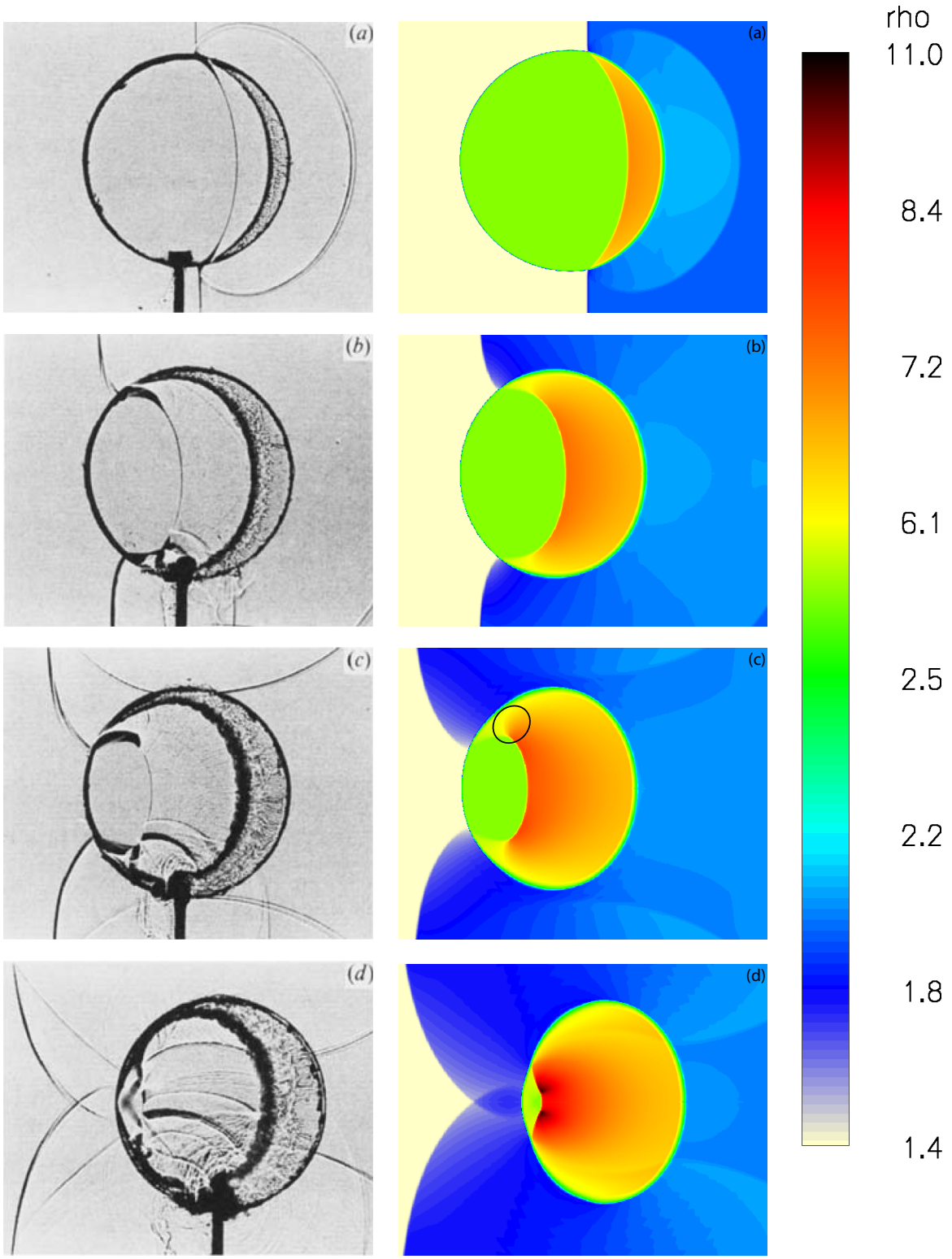

Figure 10.4: Evolution of density distribution for R22 test, left: experimental results of Haas & Sturtevant [9], right: current numerical results, at $t = 55\mu s$, $115\mu s$, $135\mu s$ and $187\mu s$.

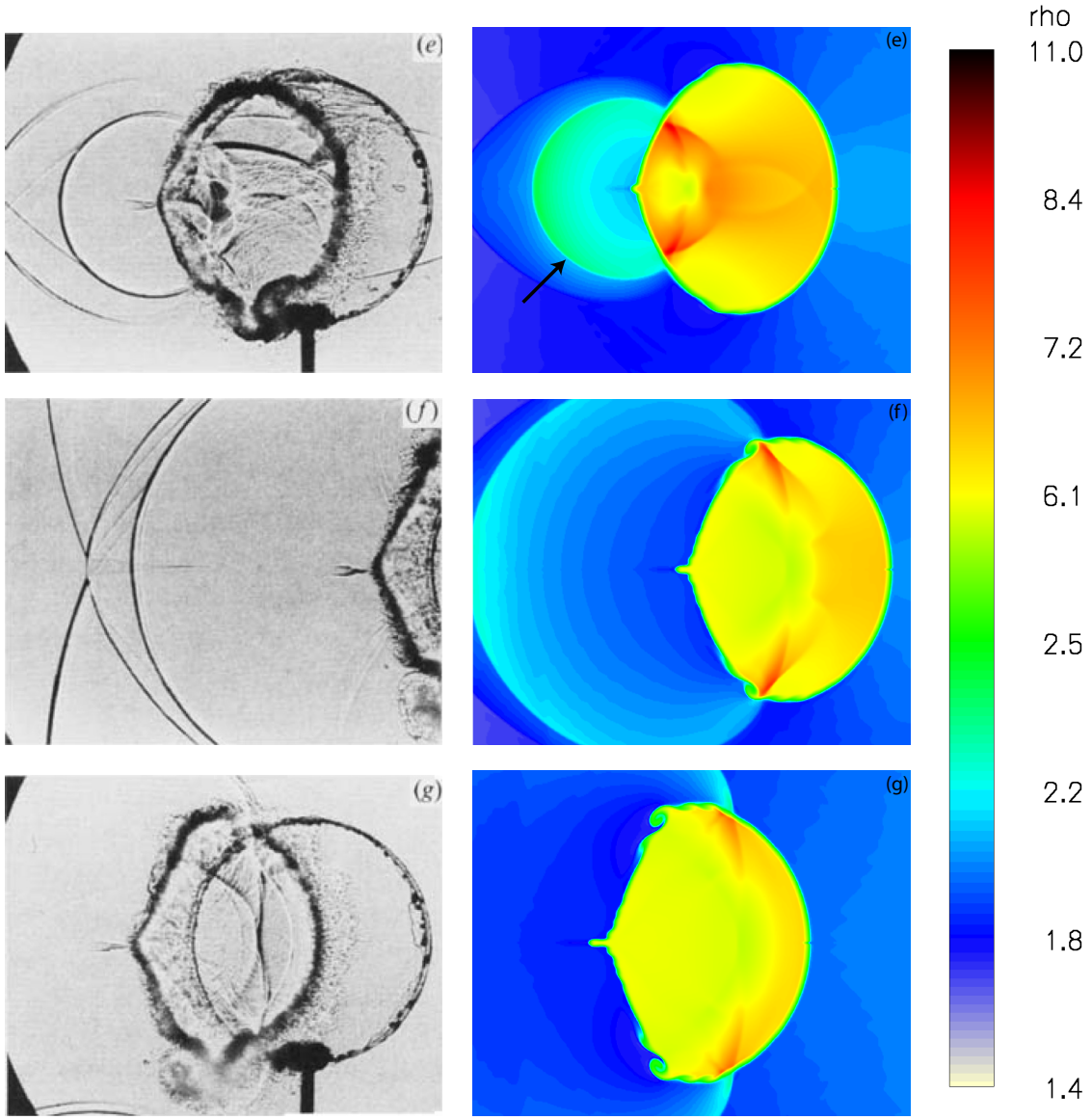

Figure 10.5: Continuation evolution of density distribution for R22 test, left: experimental results of Haas & Sturtevant [9], right: current numerical results, at $t = 247\mu s$, $318\mu s$, $342\mu s$ and $417\mu s$.

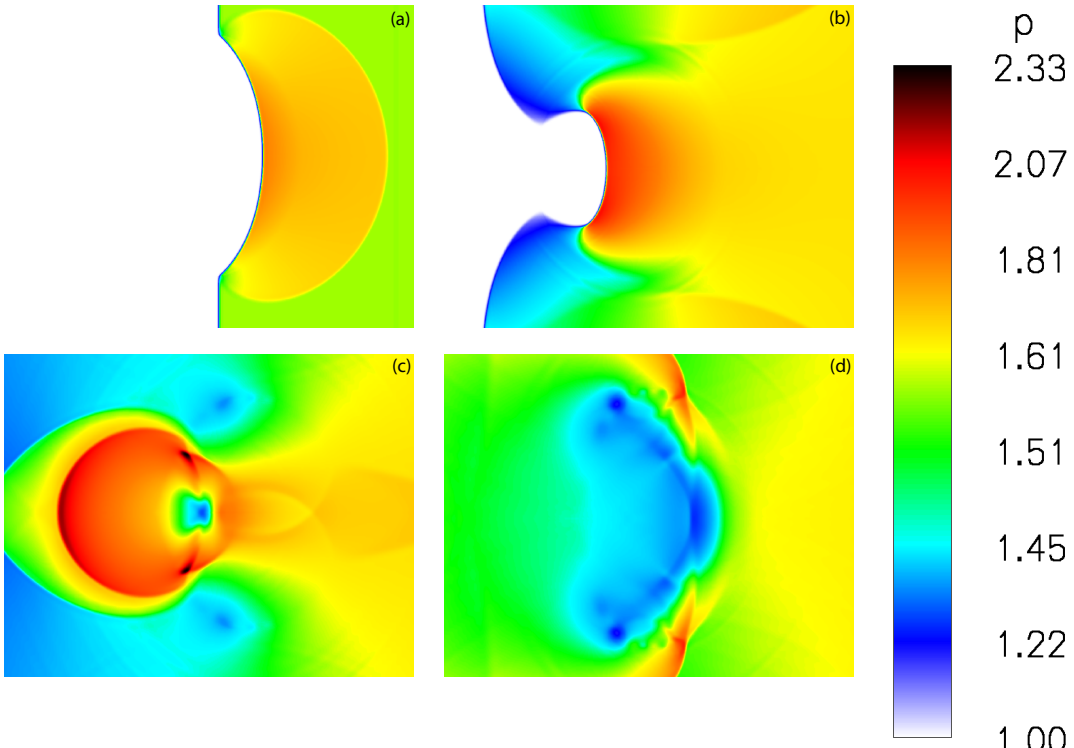

Figure 10.6: Numerical results of pressure distribution for R22 test, at $t = 55\mu s$, $135\mu s$, $247\mu s$, and $342\mu s$.

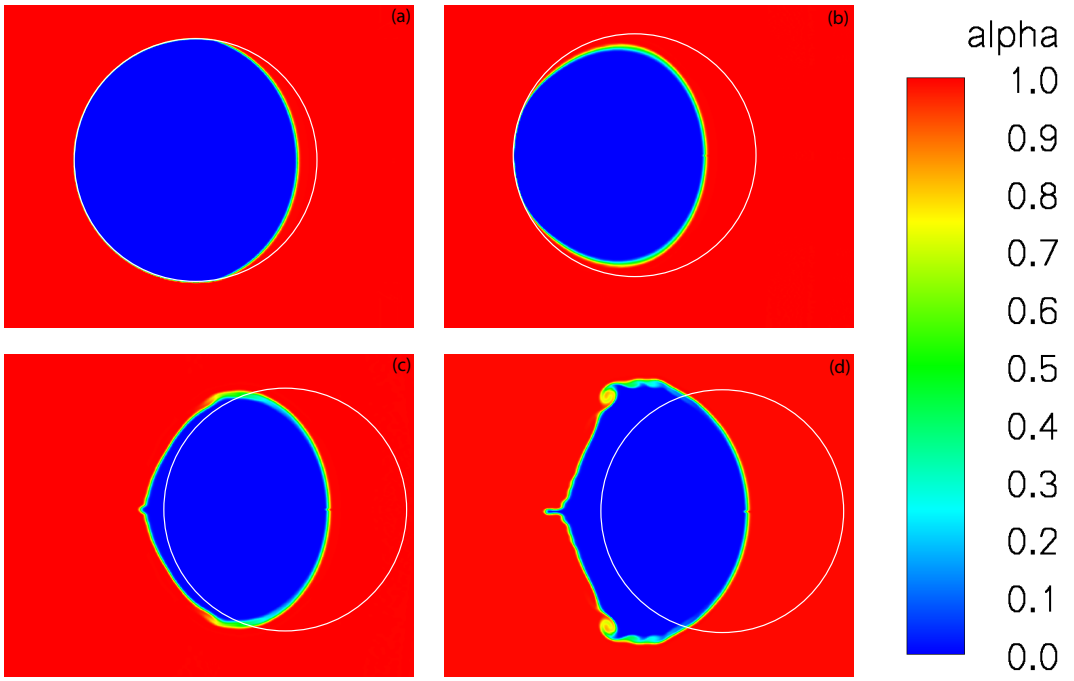

Figure 10.7: Numerical results of volume fraction distribution for R22 test, at $t = 55\mu s$, $135\mu s$, $247\mu s$, and $342\mu s$. The white line represents the initial location of the bubble.

10.2 Helium bubble

The second case contains a bubble filled with helium. Helium has a much lower density and a higher ratio of specific heats than air. This results in a speed of sound higher than air. Even though the helium in the bubble is contaminated with air, the speed of sound is still 2.544 times that of air. As a result, the refraction shock runs ahead of the incoming shock, as can be seen in figure 10.10(a). The reflection wave is a small expansion wave. Again the color bar is modified so that almost all waves and physics are visible.

Depending on the angle of incidence of the shock wave onto the interface and on the strength of the shock, the refraction can be regular or irregular. Regular means the refracted wave, incoming wave and reflected wave meet at the same point on the interface. In case the refraction is irregular, the refracted wave intersects the interface ahead of the other waves. The refraction for the R22 bubble case was completely regular. As explained in [9] for the helium bubble case, the refraction becomes irregular at an angle of incidence of 19°. Where the refracted shock hits, in the irregular case, the interface a new refraction wave appears which is called the transmitted wave. A schematic drawing of these waves is given in figure 10.8. They are also visible in the experiments and numerical results of figure 10.10(b). Due to the transmitted wave, the part of the incoming shock between the transmitted wave and the interface is deflected. Behind the incoming shock the transmitted wave interacts with the reflected expansion wave, causing the transmitted wave to bend inwards. In the triangle between the incoming wave, the transmitted wave and the expansion wave (see figure 10.8), the density becomes much higher. This is visualized in figure 10.10(b) by the dark regions. When the refracted shock continues through the bubble, an internally reflected wave appears inside the bubble. These internally reflected shocks become visible in figure 10.10(b) (also illustrated in figure 10.8). A schematic drawing of the waves inside the bubble is given in figure 10.9 to support the explination of the dynamics of the internally reflected wave, as occurs in figures 10.10(b) to 10.10(d). In figure 10.10(c) (circled) the internal reflection waves are visible as two curved shocks inside the bubble. At this time-level, the internal reflection waves become irregular. They split, resulting in a set of waves curving towards the symmetry axis and a set of waves curving away from the symmetry axis. The former

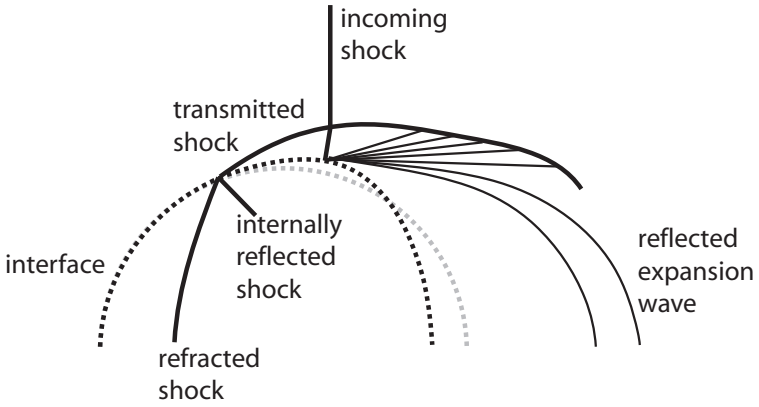

Figure 10.8: Wave pattern as a result of the interaction between the shock and the helium bubble.

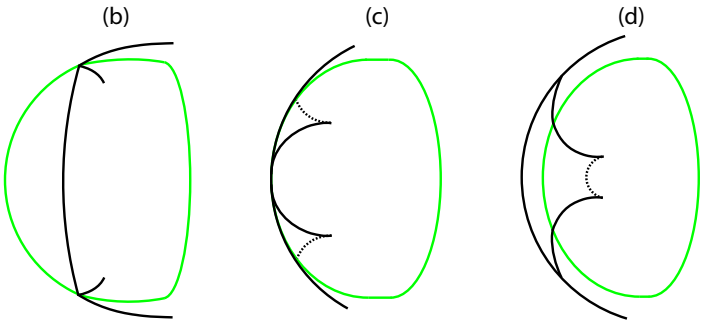

Figure 10.9: Schematic drawing of the waves inside the bubble, to clarify figures 10.10(b) to 10.10(d). The lines in the plot represent the interface "—", pressure waves "—" and weak pressure waves ".....".

are visible as half a circle in figures 10.10(c) and 10.10(d). The latter starts very weak and is therefore not visible in 10.10(c). They are indicated in figure 10.9 as two dotted lines. In figure 10.10(d) they are visible as the lighter region inside the bubble. Also the secondary transmitted waves that are created by the outward curving waves are weakly visible (and illustrated in figure 10.9). The secondary transmitted waves are located between the first transmitted wave and the interface. They are visible first in 10.10(c) and are more clear in figure 10.10(d). When the first refracted shock meets the interface on the other side of the bubble, it continues through the air as the transmitted wave.
The deformation of the bubble is clearly visible when comparing the different figures. From figure 10.10(a) to 10.10(d) the volume of the bubble becomes smaller, resulting in a higher overall density.
The internally reflected waves in figure 10.11(e) have crossed each other and now appear as a loop which expands towards the bubble interface. In figure 10.11(f) the internally reflected wave has completely crossed the interface and now continues through the air as the secondary transmitted wave, which completely encloses the bubble.
Slowly the bubble starts to roll up, finally creating two separate vortices. This process is referred to as a Rayleigh-Taylor instability, initiated by a jet flow near the centerline around the interface at the right side. This roll up is visible in the figure 10.11(g).
From figure 10.10(c) on, when the refracted shock hits the interface for the second time, the bubble completely moves to the left. This movement is best visible in the last few figures. For this purpose the T-shaped support structure in the experimental results can be taken as a reference point.
The pressure plots for the helium test case are given in figure 10.12. In the triangle structure, as explained earlier, the pressure is much higher than in the surrounding air and in the helium bubble. Again the location of the interface is not visible. Furthermore, all waves that were already described are also shown in figure 10.12.
The interface is shown in figure 10.13 by means of the volume fraction. The white line indicates the initial location of the bubble.
Also for the helium test case some quantitative comparison of wave speeds can be made. Again we compare the wave velocity of the incoming shock, c_s, the velocity of the refraction wave, c_r, and the velocity of the interface, c_i. These velocities are given in table 10.3. Again the wave speeds show a good similarity with the other data, especially with the numerical simulations. The small differences in the velocities of the refracted shock and the interface can originate from the different numerical methods used, but

	c_s $[m/s]$	c_r $[m/s]$	c_i $[m/s]$
Present method	419	956	176
Haas & Sturtevant [9]	410	900	170
Quirk & Karni [20]	422	943	178
Wackers & Koren [29]	419	950	173
Naber [17]	419	955	181

Table 10.3: Comparison of wave speeds between several numerical results, including ours, and the experimental results, for the R22 bubble test.

can also differ because of a different location and domain over which a displacement is measured.

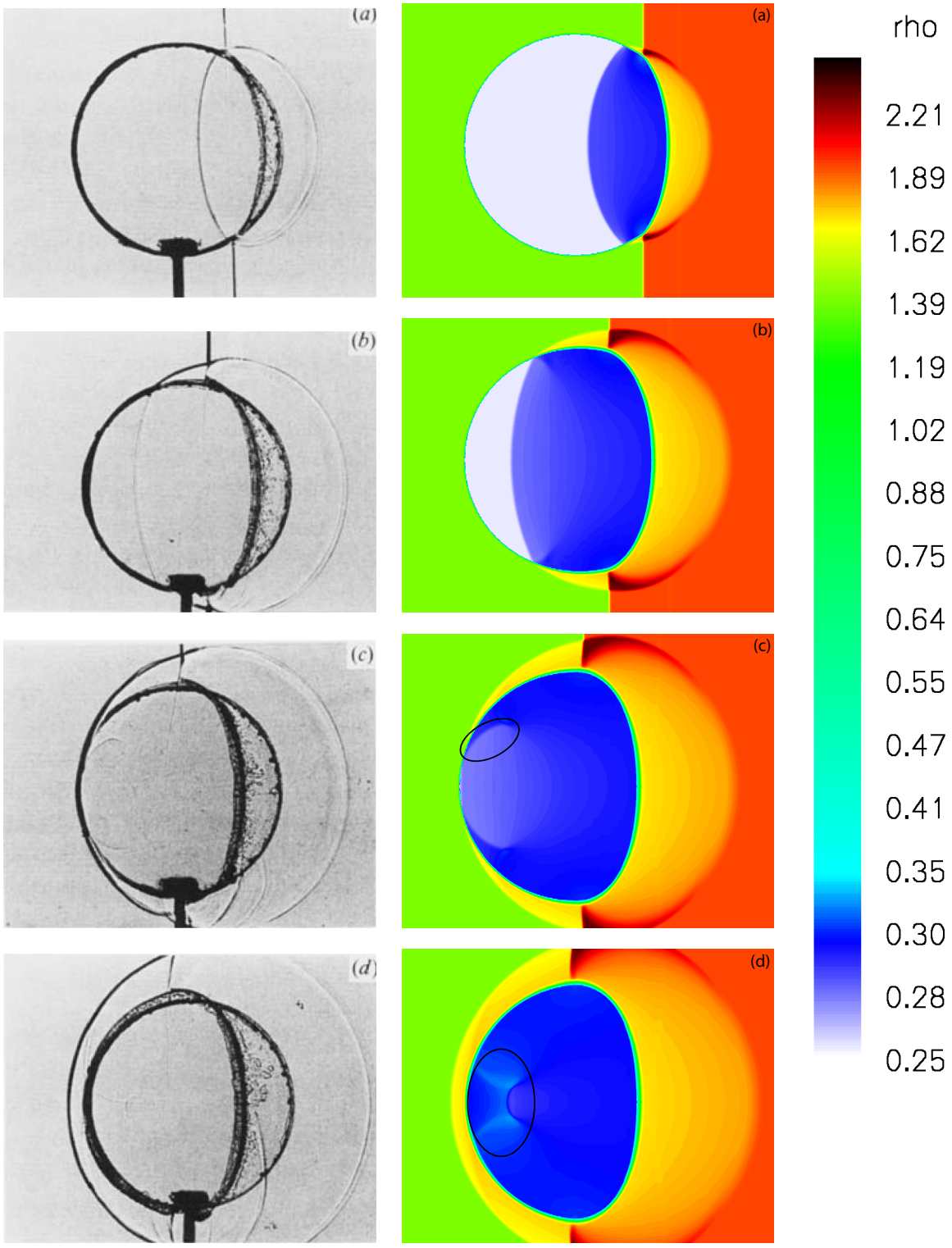

Figure 10.10: Evolution of density distribution for the helium test, left: experimental results of Haas & Sturtevant [9], right: current numerical results, at $t = 32\mu s$, $52\mu s$, $62\mu s$ and $72\mu s$.

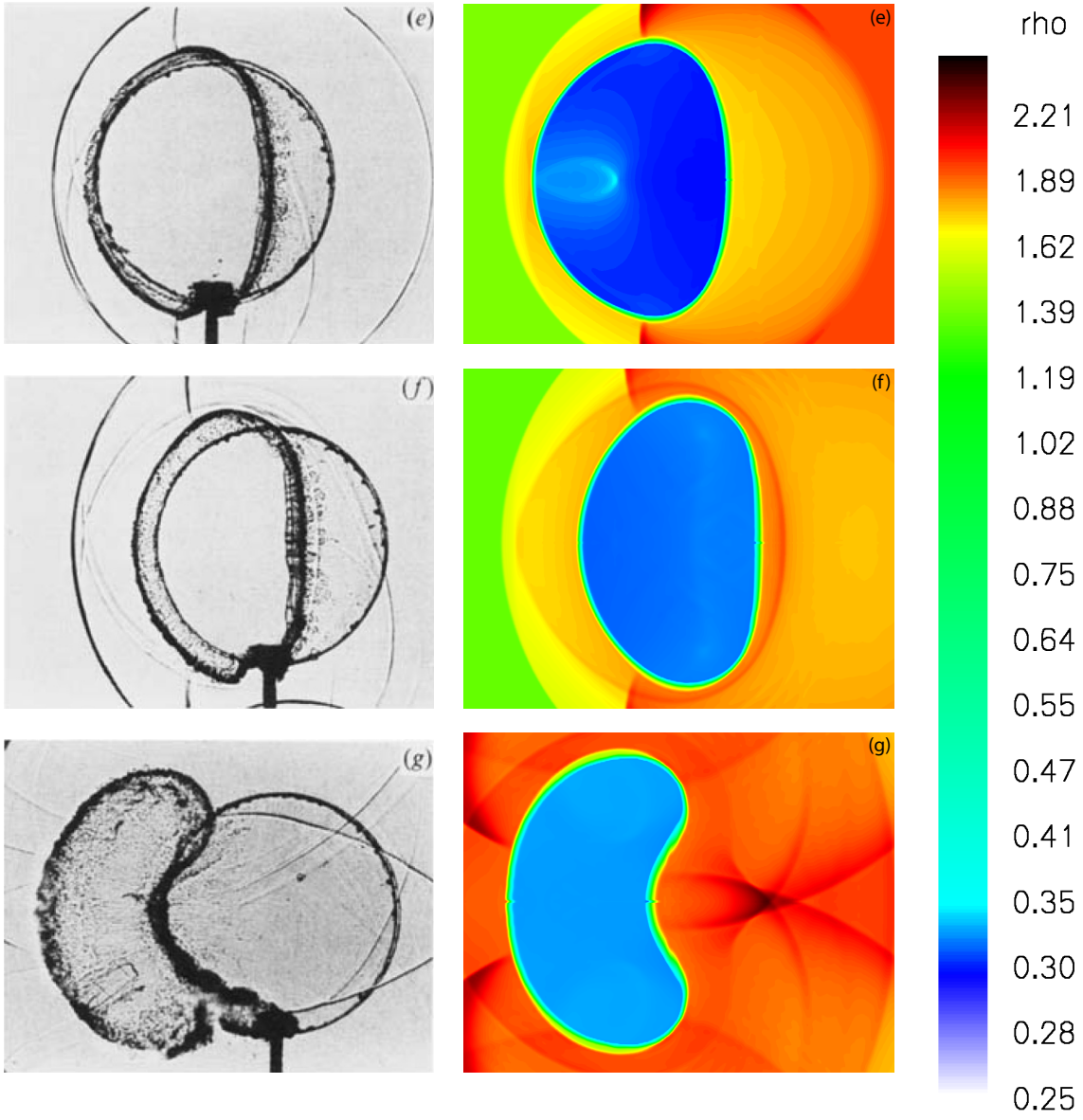

Figure 10.11: Continuation evolution of density distribution for the helium test, left: experimental results of Haas & Sturtevant [9], right: current numerical results, at $t = 82\mu s$, $102\mu s$ and 245(exp.) / 230(num.) μs.

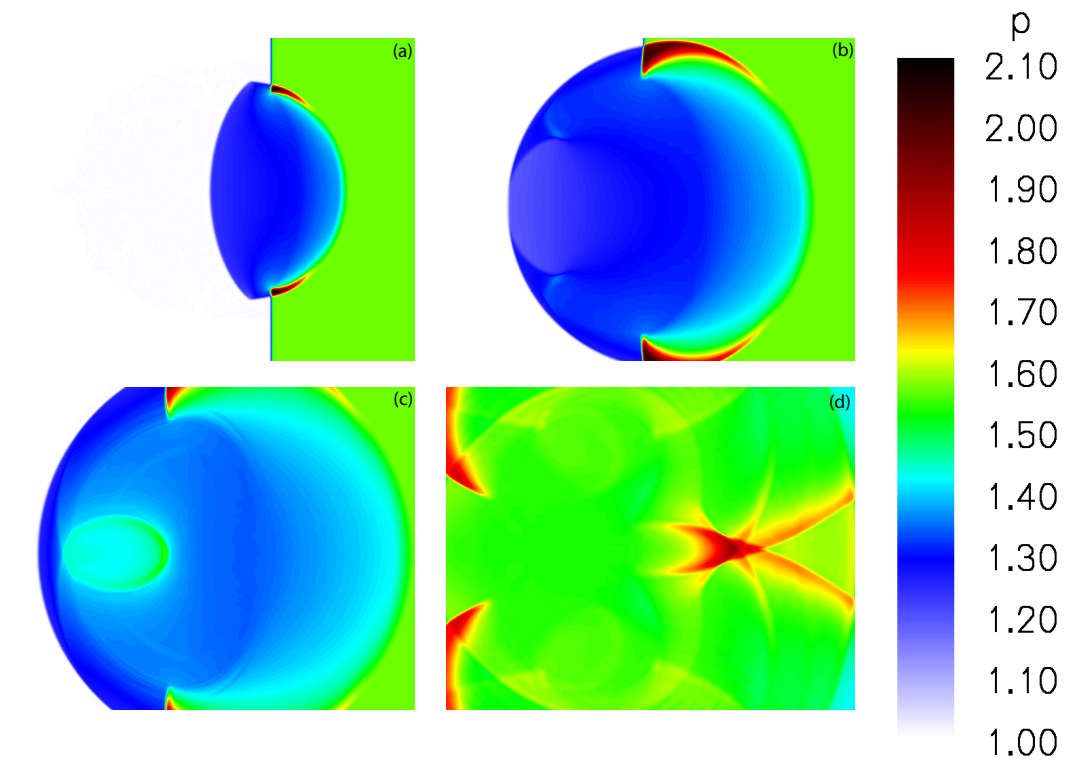

Figure 10.12: Numerical results of pressure distribution for the helium test, at $t = 32\mu s$, $62\mu s$, $82\mu s$, and $230\mu s$.

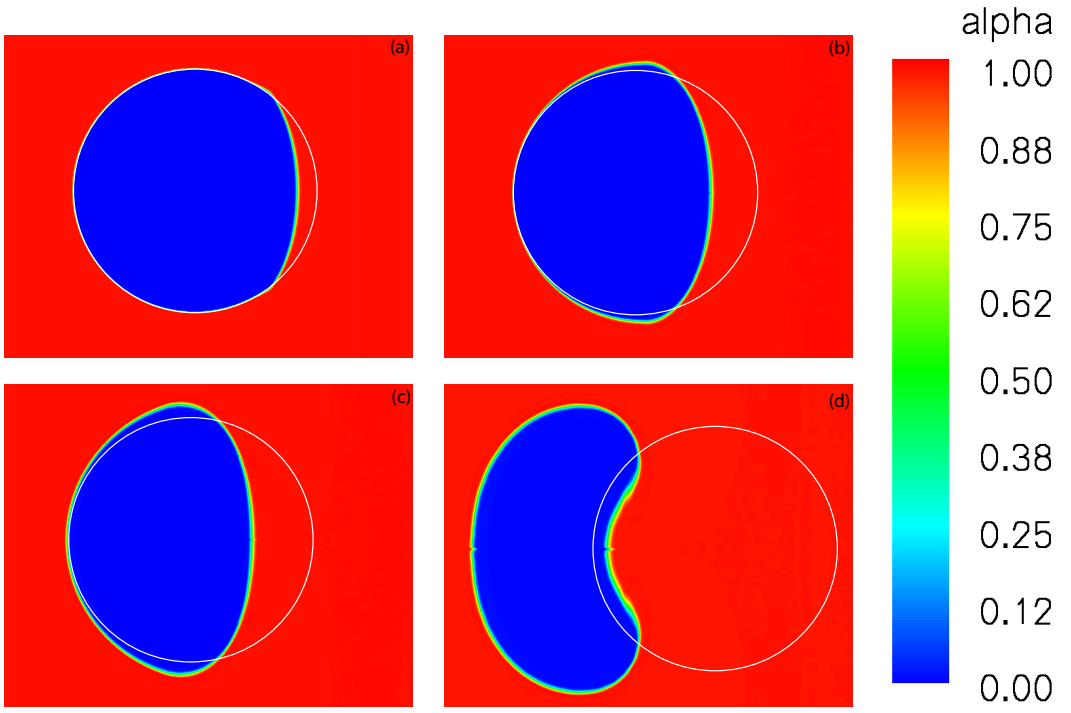

Figure 10.13: Numerical results of volume fraction distribution for the helium test, at $t = 32\mu s$, $62\mu s$, $82\mu s$, and $230\mu s$. The white line represents the initial location of the bubble.

Chapter 11

Conclusions and recommendations

This chapter concludes the thesis work presented in this report. Section 11.1 gives the conclusions that can be drawn. Section 11.2 lists a number of suggestions for future research.

11.1 Conclusions

In this report an Euler based, unsteady compressible two-fluid model for interface capturing was presented. The model consists of a set of five equations: a mass, momentum and energy equation for the bulk, and a mass and energy equation for one of the two fluids. These equations contain two new variables which distinguish the two fluids, a volume fraction and a mass fraction. While the first four equations are written in conservative form, the latter is not. The energy equation for one of the two fluids contains a source term, which represents the exchange in energy between the two fluids. This source term represents the closure of the model. It depends on how the interface is treated.
For the interface we required that the fluids are immiscible, so no mass transport over the interface, and that the pressures and velocities on both sides of the interface are equal. With these requirements a closure is formulated which consists of three terms: a pressure force which counts for the increment in volume fraction, a force that keeps the velocity of both fluids equal and a force that keeps the pressure constant over the interface.
The model is successfully discretized through a finite volume method, which is limited second-order accurate in space and third-order accurate in time. The fluxes are evaluated using Osher's Riemann solver. The Osher solver required the derivation the Riemann invariants. A sophisticated discretization of the source term is developed. The discretization method uses the state distribution that was created by the limited data reconstruction and by the flux solver.
The model and numerical solver are tested using several shock tube problems and two shock-bubble interaction problems. The results confirm that the method is pressure-oscillation free. The pressure and velocity are continuous over the interface. The numerical results of the shock tube problems show that the various waves are captured at properly. The shock-bubble interaction problems show a very good resemblance with the experimental results. More details are even visible in the numerical results. The shocks and interface are captured sharply, even after many time steps.
To complete the model, jump conditions are derived. These jump conditions relate the

states on both sides of a discontinuity in the flow, like a contact discontinuity or a shock. Note that these relations are derived to complete the theoretical part. The numerical results show that these jump conditions are not needed to do a proper simulation. The jump conditions are not yet validated and also not used. This brings us to the list of recommendations.

11.2 Recommendations

Although the model works nicely, there are always possibilities for improvement. Besides, the model method might be used in different applications. Therefore a list of recommendations in given below.

Jump conditions and exact Riemann solver
Jump conditions are derived in chapter 4, but in this research they were not validated by numerical simulations. A closer look into the jump conditions is needed. With the jump conditions it is possible to use the exact Riemann solver. This Riemann solver is based on the physical waves.

Efficient approximate Riemann solver
The Osher solver is very computating intensive, because the Riemann invariants have to be integrated numerically through the isentropic waves. Much time is gained when using another approximate Riemann solver which does not require numerical integration of the Riemann invariants.

Application to 'mixtures'
The two-fluid model does not allow mixing of the two fluids, so on microscopic level there are two fluids separated by an interface. However, on macroscopic level, when we consider a fluid element, it can only be said that the domain contains both fluids and how much of each fluid is present, but not their locations. So on macroscopic level it is a mixture. These kinds of 'mixtures' also occur in practice, for example metal alloys (see [28]). In metal alloys the different metals do not mix, but they consist of many very small elements of a single metal. Probably there are more of these 'mixtures' possible. Questionable is whether they agree with the simplifications of section 1.2.

More equations of state
The model derived in part I does not specify equations of state. So different equations of state can be included in the model. This requires some adjustments in the algorithm, as shown in chapter 8.

Discontinuous Galerkin methods
Instead of a finite-volume method, the two-fluid model can also be discretized using a discontinuous Galerkin method. The discontinuous Galerkin method will result in sharper capturing of the discontinuities, like shocks and the interface.

Adaptive mesh refinement
The interface acts as a transition layer between the two fluids. Numerically this transition layer is smeared over a number of cells. Adaptive mesh refinement can be used to reduce the thickness of the transition layer, while the interface remains smeared

over the same number of cells. Besides the interface, also other discontinuities, like shocks, are captured sharper.

Shallow Water flow over a non-flat bottom
The momentum equation for shallow water flow over a non-flat bottom has the same kind of source term as our model, so the same discretization method as in chapter 7 can be used to discretize that source term.

Extension to full Navier-Stokes
The two-fluid model in this report is based on the Euler equations, so it treats only transport phenomena. To be able to model diffusive phenomena, the extension to a two-fluid Navier-Stokes model has to be made.

Bibliography

[1] R. Abgrall and S. Karni. Computations of compressible multifluids. *Journal of Computational Physics*, 169:594–623, 2001. [2]

[2] J.D. Anderson. *Fundamentals of Aerodynamics*. McGraw-Hill, 1991. [87]

[3] M.R. Baer and J.W. Nunziato. A two-phase mixture theory for the deflagration-to-detonation transition (ddt) in reactive granular materials. *Journal of Multiphase Flow*, 12:861–889, 1986. [3, 36]

[4] P. Bakker and B. van Leer. Lecture notes on gasdynamics, AE4-140. Lecture Notes TU Delft, 2005. [37]

[5] D.J. Benson. Computational methods in Lagrangian and Eulerian hydrocodes. *Computer Methods in Applied Mechanics and Engineering*, 99:235–394, 1992. [1]

[6] S.K. Godunov. A finite difference method for the computation of discontinuous solutions of the equations of fluid dynamics. *Matematicheskii Sbornik*, 47:357–393, 1959. Translated from Russian. [29]

[7] H. Guillard and M. Labois. Numerical modeling of compressible two-phase flows. In *ECCOMAS CFD 2006*, 2006. [4]

[8] H. Guillard and A. Murrone. A five equation reduced model for compressible two phase problems. Technical Report N° 4778, INRIA, 2003. [2, 4]

[9] J.F. Haas and B. Sturtevant. Interaction of weak shock waves with cylindrical and spherical gas inhomogeneities. *Journal of Fluid Mechanics*, 181:41–76, 1987. [65, 66, 68, 69, 70, 72, 74, 75, 76]

[10] F.H. Harlow and J.E. Welch. Numerical calculation of time-dependent viscous incompressible flow of fluid with free surface. *Physics of Fluids*, 8:2182–2189, 1965. [2]

[11] P.W. Hemker and S.P. Spekreijse. Multipe grid and Osher's scheme for the efficient solution of the steady Euler equations. *Applied Numerical Mathematics*, 2:475–493, 1986. [34]

[12] C.W. Hirt and B.D. Nichols. Volume of Fluid method for the dynamics of free boundaries. *Journal of Computational Physics*, 39:201–225, 1981. [2]

[13] W. Hundsdorfer, B. Koren, M. van Loon, and J.G. Verwer. A positive finite-difference advection scheme. *Journal of Computational Physics*, 117:35–46, 1995. [31]

[14] B. Koren. *A robust upwind discretization method for advection, diffusion and source terms, Numerical methods for advection-diffusion problems*, volume 45 of *Notes on Numerical Fluid Mechanics*, pages 117–138. Vieweg, 1993. C.B. Vreugdenhil and B. Koren (eds.). [29]

[15] H. Lomax, T.H. Pulliam, and D.W. Zingg. *Fundamentals of Computational Fluid Dynamics*. Springer, 2003. [27]

[16] J. Naber. Numerical solver for compressible two-fluid flow. Technical Report MAS-E0505, CWI, 2005. `http://ftp.cwi.nl/CWIreports/MAS/MAS-E0505.pdf`. [56, 60, 65]

[17] J. Naber. A Runge-Kutta discontinuous-Galerkin level-set method for unsteady compressible two-fluid flow. Master's thesis, Delft University of Technology, 2005. Technical Report MAS-N0301, CWI `http://ftp.cwi.nl/CWIreports/MAS/MAS-N0601.pdf`. [2, 56, 60, 65, 66, 68, 74]

[18] S. Osher and F. Solomon. Upwind difference schemes for hyperbolic systems of conservation laws. *Mathematics of Computation*, 38:339–374, 1982. [33, 34]

[19] F. Platzek. Modeling of shalow water flow over a non-flat bottom. Master's thesis, Delft University of Technology, 2007. [47]

[20] J.J. Quirk and S. Karni. On the dynamics of a shock-bubble interaction. Technical Report ICASE Report No. 94-75, NASA Langley Research Center, 1994. [4, 56, 65, 68, 74]

[21] K.M. Shyue. A fluid-mixture type algorithm for compressible multicomponent flow with Van der Waals equation of state. *Journal of Computational Physics*, 156: 43–88, 1999. [56]

[22] S.P. Spekreijse. *Multigrid solution of the steady Euler equations*. PhD thesis, Delft University of Technology, 1988. [29, 33, 34]

[23] P.K. Sweby. High resolution schemes using flux limiters for hyperbolic conservation laws. *SIAM Journal on Numerical Analysis*, 21:995–1011, 1984. [29]

[24] E. van der Maarel. *A Local Grid Refinement Method for the Euler Equations*. PhD thesis, University of Amsterdam, 1993. [28]

[25] B. van Leer. Towards the ultimate conservative difference scheme. V. A second-order sequel to Godunov's method. *Journal of Computational Physics*, 32:101–136, 1979. [28]

[26] B. van Leer. *Upwind-difference methods for aerodynamic problems governed by the Euler equations, Lectures in Applied Mathematics*, volume 22, pages 327–336. American Mathematical Society, 1985. [29]

[27] J. Wackers. An adaptive-gridding solution method for the 2d unsteady Euler equations. Master's thesis, Delft University of Technology, 2003. Technical Report MAS-N0301, CWI, `http://ftp.cwi.nl/CWIreports/MAS/MAS-N0301.pdf`. [33]

[28] J. Wackers. *Surface Capturing and Multigrid for Steady Free-Surface Water Waves*. PhD thesis, Delft University of Technology, 2007. [19, 20, 24, 80]

[29] J. Wackers and B. Koren. Five-equation model for compressible two-fluid flow. Technical Report MAS-E0414, CWI, 2005. `http://ftp.cwi.nl/CWIreports/MAS/MAS-E0414.pdf`. [2, 4, 29, 56, 58, 60, 65, 66, 67, 68, 74]

Appendix A

Speed of sound for general equation of state

This appendix derives the different forms in which the speed of sound can be given. These are used in the derivations or can be used to express the speed of sound in thermodynamic variables for any given equation of state.

We start with the assumption that the flow through a soundwave is both adiabatic and reversible, thus isentropic. Without proof we start by defining the speed of sound as (for a derivation see e.g. Anderson [2]):

$$c_i^2 = \left(\frac{\mathrm{d}p}{\mathrm{d}\rho_i}\right)_{s_i}. \tag{A.1}$$

To express the speed of sound in the thermodynamic variables ρ_i, p and e_i, we start with the first law of thermodynamics:

$$\mathrm{d}e_i = \delta q_i + \delta w_i.$$

The work as shown in chapter 3 is given by:

$$\delta w_i = -p\mathrm{d}V_i = -p\mathrm{d}\left(\frac{1}{\rho_i}\right).$$

Futhermore sound propagation is isentropic, so for the second law of thermodynamics it follows that $\delta q = 0$, and thus:

$$\mathrm{d}e_i + p\mathrm{d}\left(\frac{1}{\rho_i}\right) = 0,$$

or

$$\left(\frac{\partial e_i}{\partial p}\right)_{\rho_i}\mathrm{d}p + \left(\frac{\partial e_i}{\partial \rho_i}\right)_{p}\mathrm{d}\rho_i - \frac{p}{\rho_i^2}\mathrm{d}\rho_i = 0.$$

The first way to write the speed of sound in thermodynamic variables is:

$$c_i^2 = \left(\frac{\partial p}{\partial \rho_i}\right)_{s_i} = \frac{\frac{p}{\rho_i^2} - \left(\frac{\partial e_i}{\partial \rho_i}\right)_p}{\left(\frac{\partial e_i}{\partial p}\right)_{\rho_i}}. \tag{A.2}$$

We can use multivariable calculus for ρ_i, p and e_i. Since they are constrained by $f(\rho_i, p, e_i) = 0$, we can say that:

$$\left(\frac{\partial p}{\partial e_i}\right)_{\rho_i} \cdot \left(\frac{\partial e_i}{\partial \rho_i}\right)_{p} \cdot \left(\frac{\partial \rho_i}{\partial p}\right)_{e_i} = -1.$$

Substituting this into equation (A.2), gives:

$$c_i^2 = \left(\frac{\partial p}{\partial \rho_i}\right)_{s_i} = \left(\frac{\partial p}{\partial \rho_i}\right)_{e_i} + \frac{p}{\rho_i^2}\left(\frac{\partial p}{\partial e_i}\right)_{\rho_i}. \tag{A.3}$$